LEVEL II

SCHOOL OF APPLIED AND ENGINEERING PHYSICS

CORNELL UNIVERSITY
ITHACA, NEW YORK
14853

LEVEL II

(12)

(9) Doctoral thesis,

(6) PROPERTIES OF SUPERCONDUCTOR-NORMAL METAL-
SUPERCONDUCTOR MICRIBRIDGES.

by (0)

(10) John Michael Warlaumont

(11) 21 Jul 80

(13) 178

(15) N00014-76-C-0526

(14) 8p-2

Ph.D. Thesis
January 1980

DTIC
S ELECTE D
AUG 5 1980

D

Research Group:
Prof. R. A. Buhrman
A&EP

407244

REPORT DOCUMENTATION PAGE	READ INSTRUCTIONS BEFORE COMPLETING FORM

1. REPORT NUMBER	2. GOVT ACCESSION NO.	3. RECIPIENT'S CATALOG NUMBER
80-2	AD-A087 512	

4. TITLE (and Subtitle)	5. TYPE OF REPORT & PERIOD COVERED
Properties of Superconductor-Normal Metal-Super-conductor Microbridges	Technical Report
	6. PERFORMING ORG. REPORT NUMBER
	80-2

7. AUTHOR(s)	8. CONTRACT OR GRANT NUMBER(s)
John Michael Warlaumont	NR319-096

9. PERFORMING ORGANIZATION NAME AND ADDRESS	10. PROGRAM ELEMENT, PROJECT, TASK AREA & WORK UNIT NUMBERS
R. A. Buhrman, Applied & Engineering Physics Cornell University Ithaca, New York 14853	N00014-76-C-0526

11. CONTROLLING OFFICE NAME AND ADDRESS	12. REPORT DATE
Electronic & Solid State Sciences Program Code 427 - Office of Naval Research 800 N. Quincy, Arlington, VA 22217	July 21, 1980
	13. NUMBER OF PAGES
	163

14. MONITORING AGENCY NAME & ADDRESS(if different from Controlling Office)	15. SECURITY CLASS. (of this report)
	Unclassified
	15a. DECLASSIFICATION/DOWNGRADING SCHEDULE

16. DISTRIBUTION STATEMENT (of this Report)

Approved for public release, distribution unlimited.

17. DISTRIBUTION STATEMENT (of the abstract entered in Block 20, if different from Report)

18. SUPPLEMENTARY NOTES

19. KEY WORDS (Continue on reverse side if necessary and identify by block number)

Josephson effect, Quantum superconductivity, Superconductor-Normal Metal Proximity Effect

20. ABSTRACT (Continue on reverse side if necessary and identify by block number)

This theses describes the fabrication and electrical measurement of short, high resistance (R~1 ohm) superconductor-normal metal-superconductor micro-bridges.
These small (length and width as small as 200 nm), planar structures were produced using electron-beam lithography and ion-beam etching. Lead-copper-lead structures were primarily studied; other materials ver also briefly in-vestigated. →over (OVER)

DD FORM 1473 EDITION OF 1 NOV 65 IS OBSOLETE
1 JAN 73
S/N 0102-LF-014-6601

80. 8 1 023

The small cross section of the bridges resulted in a uniform current distribution in the bridges at all temperatures, thus enabling the experimental determination of the critical current versus temperature relation for all temperatures between T_c and $0.05\ T_c$, where T_c is the transition temperature of the electrodes. This experimental $I_c(T)$ relation was found to agree with theoretical predictions based on Usadel's equations. This successful fit of theory to experiment produced a reduced length ℓ for each sample; the samples had reduced lengths ranging from 8.2 to 30.

The low-voltage current-voltage (I-V) characteristics were studied in detail. It was found that these I-V curves could be characterized by a temperature independent relaxation time τ_{eff}; this relaxation time was observed to be proportional to ℓ^2. At low temperatures the I-V curves were hysteretic, with the curves returning to the zero-voltage axis at a return current I_R. It was observed that I_R was independent of temperature at low temperatures, having the low temperature value of $I_R R \sim 5\hbar/2e\tau_{eff}$. This hysteresis could be definitely attributed to the effective relaxation time, in contrast to the heating or capacitance explanations used for all-superconductor microbridges.

At all temperatures the low-voltage I-V curves were straight lines for voltages greater than $5\hbar/2e\tau_{eff}$.

It was found that the nature of th I-V curve with applied microwave radiation was also dependent on τ_{eff}. If the microwave period was shorter than τ_{eff} or $\hbar/2eI_c R$, there was a microwave-enhanced critical current. For microwave periods longer than both these times there was no enhancement. This result indicated that the critical-current enhancement was most likely caused by a microwave-induced spatial broadening of the quasiparticle distribution in the bridge.

Constant-voltage steps were observed in the I-V curves for all frequencies of microwave radiation used. For the shortest samples steps were observed at voltages greater than 2 mV. Subharmonic steps were observed whenever the critical current was enhanced.

The high resistance of these samples permitted measurement of the I-V curves for voltages much greater than the energy gap of the electrodes. A high-voltage peak in the dV/dI curves was observed, and it was speculated that this peak was due to an extra dissipation in the electrodes. In addition, the low-voltage resistance was found to have a temperature dependence which agreed with the phenomenological theory of Pippard et al., a theory which attributes the extra resistance to energy dissipation in the electrodes.

Biographical Sketch

The author was born in Pocatello, Idaho, in 1945. He was educated there at St. Joseph's Elementary School, and he attended high school in Ogden, Utah.

The author graduated summa cum laude from the University of Utah in 1970, obtaining a Bachelor of Arts degree in Physics.

From 1970 until 1978 the author was enrolled in the Graduate School at Cornell University; during this time he was supported in the Physics Department by teaching and research assistantships.

Since 1978 the author has been a research staff member at the Watson Research Center of the International Business Machines Corporation.

In August 1978 the author married Pia Naoko Sanda.

To my parents

Acknowledgements

First and foremost, I wish to thank Professor Robert Buhrman for his guidance, counseling, friendship, and patience; his advice and encouragement were invaluable throughout my stay in Clark Hall.

Professor Watt Webb was very helpful in the initial stages of this work, and his role as chairman of the special committee is gratefully acknowledged. I also thank Professors Robert Richardson and Geoffrey Chester for serving on the special committee.

Dr. T. D. Clark and Dr. L. D. Clark gave invaluable scientific advice and technical expertise. Alan Kleinsasser and James Brown also provided valuable assistance.

Bill Bement, John Smith, Ray Coles, and the rest of the Clark Hall technical staff were very helpful throughout the course of this work.

Of course, the friendship of the residents of F, G, and H corridors was indispensable; in particular, the comradeship of Larry Jackel, Terry Clark, Jerry Dolan, Chuck Archie, and Mike Christensen will never be forgotten.

The encouragement, patience, and love of my wife Pia were essential to the completion of this work.

Table of Contents

Table of Contents

List of Tables

List of Figures

PROPERTIES OF SUPERCONDUCTOR-NORMAL METAL-
SUPERCONDUCTOR MICROBRIDGES

John Michael Warlaumont, Ph.D.
Cornell University, 1980

This thesis describes the fabrication and electrical measurement of
short, high resistance (R $\sim$ 1 ohm) superconductor-normal metal-
superconductor microbridges.

These small (length and width as small as 200 nm), planar structures
were produced using electron-beam lithography and ion-beam etching. Lead-
copper-lead structures were primarily studied; other materials were also
briefly investigated.

The small cross section of the bridges resulted in a uniform current
distribution in the bridges at all temperatures, thus enabling the
experimental determination of the critical current versus temperature
relation for all temperatures between T_c and 0.05 T_c, where T_c is the
transition temperature of the electrodes. This experimental $I_c(T)$ relation
was found to agree with theoretical predictions based on Usadel's
equations. This successful fit of theory to experiment produced a reduced
length ℓ for each sample; the samples had reduced lengths ranging from
8.2 to 30.

The low-voltage current-voltage (I-V) characteristics were studied
in detail. It was found that these I-V curves could be characterized by a
temperature independent relaxation time τ_{eff}; this relaxation time was
observed to be proportional to ℓ^2. At low temperatures the I-V curves
were hysteretic, with the curves returning to the zero-voltage axis at a
return current I_R. It was observed that I_R was independent of temperature

at low temperatures, having the low temperature value of $I_R R \simeq 5\hbar/2e\tau_{eff}$. This hysteresis could be definitely attributed to the effective relaxation time, in contrast to the heating or capacitance explanations used for all-superconductor microbridges.

At all temperatures the low-voltage I-V curves were straight lines for voltages greater than $5\hbar/2e\tau_{eff}$.

It was found that the nature of the I-V curve with applied microwave radiation was also dependent on τ_{eff}. If the microwave period was shorter than τ_{eff} or $\hbar/2eI_c R$, there was a microwave-enhanced critical current. For microwave periods longer than both these times there was no enhancement. This result indicated that the critical-current enhancement was most likely caused by a microwave-induced spatial broadening of the quasiparticle distribution in the bridge.

Constant-voltage steps were observed in the I-V curves for all frequencies of microwave radiation used. For the shortest samples steps were observed at voltages greater than 2 mV. Subharmonic steps were observed whenever the critical current was enhanced.

The high resistance of these samples permitted measurement of the I-V curves for voltages much greater than the energy gap of the electrodes. A high-voltage peak in the dV/dI curves was observed, and it was speculated that this peak was due to an extra dissipation in the electrodes. In addition, the low-voltage resistance was found to have a temperature dependence which agreed with the phenomenological theory of Pippard et al., a theory which attributes the extra resistance to energy dissipation in the electrodes.

Chapter 1

INTRODUCTION

The subject of this work is the experimental investigation of a specific kind of superconducting weak link--planar superconductor-normal metal-superconductor microbridges. But the goal of this work is not only to characterize the physical properties of SNS microbridges, but also to gain a better understanding of the other types of super-conducting junctions by noting both the similarities and differences between the samples of this work and other systems. In fact, we have also discovered phenomena which are applicable to physical systems other than superconducting junctions.

In this introduction a very brief discussion of superconducting junctions will be given, as well as an explanation of how this work relates to the previous work in the field. The remainder of this thesis will describe in detail our experimental observations and our understanding of the physical processes behind these observations.

The term "superconducting junction" applies to any conducting link between two large superconducting electrodes; the electrodes are assumed to behave essentially like bulk superconductors, and the link between them is assumed to be sufficiently weak that the electro-magnetic properties of the sample are determined mostly by the link. The basic ideas behind such structures were first developed by Josephson[1] in 1962. Since that pioneering work there have been thousands of papers published on this subject. (A recent review has been given by Likharev.[2]) But in spite of this tremendous amount of

effort, there are still a large number of unexplained experiments, particularly those which involve non-equilibrium situations or time-dependent phenomena. The major difficulty on the theoretical side has been the very complicated microscopic theory of superconductivity. On the experimental side, it has been very difficult to fabricate well-defined junctions due to the very small lengths involved and the often-undesirable mechanical and chemical properties of superconducting materials. We have attempted to simplify the theoretical analysis by making samples which have a very well-defined weak region; this has been accomplished by using a normal metal as the bridge between the super-conducting electrodes. In addition, we have taken advantage of modern lithographic technology to significantly reduce the size of the bridge. We have succeeded in producing samples which have been of sufficient quality to allow verification of some previously unproved theories; in addition, we have observed phenomena which have not been anticipated by any of the available theories.

There are several different types of superconducting junctions, and only one type, the thin-film microbridge, will be discussed here. The reader is referred to the works of Jackel[3] and Henkels[4] for descriptions of the other types.

A schematic diagram of a thin-film superconducting microbridge is given in Figure 1.1. The structure consists of two superconducting electrodes (banks) connected by a small metal link (bridge). The metal films are deposited on an insulating substrate, and they are sculptured into the desired shape by a variety of techniques. They can be scribed
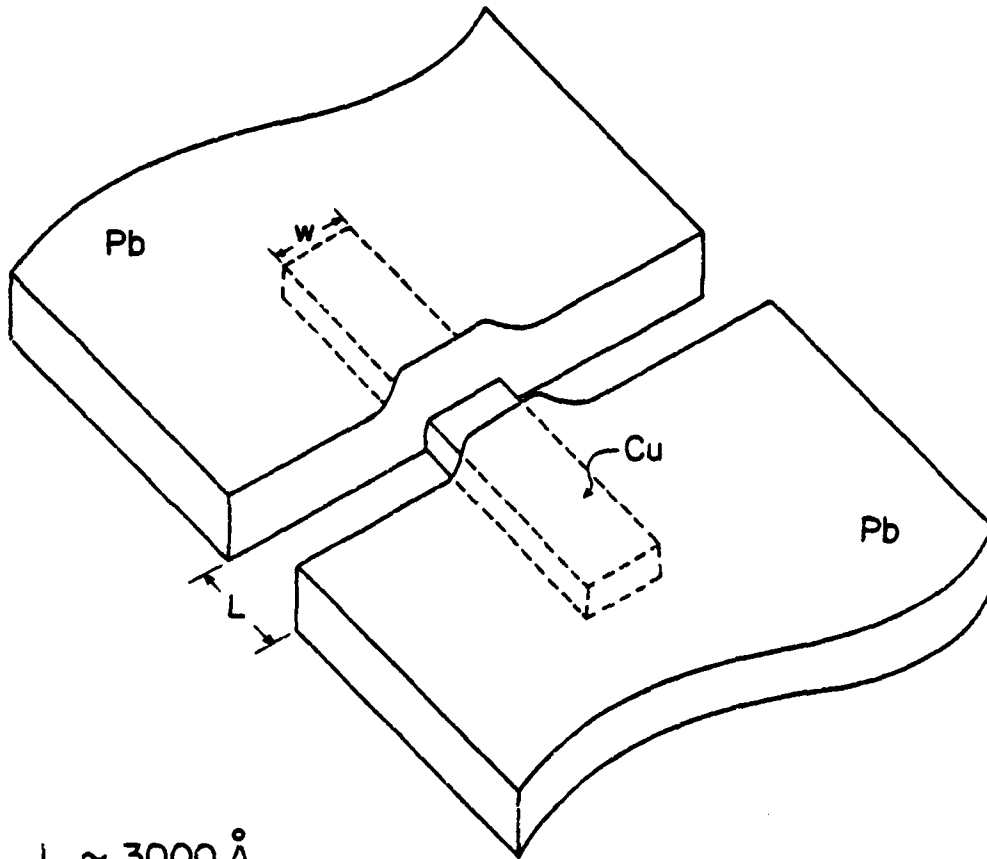
$$L \sim 3000 \ \overset{\circ}{A}$$
$$w \sim 3000 \ \overset{\circ}{A}$$
$$Pb \sim 1500 \ \overset{\circ}{A} \quad thick$$
$$Cu \sim \ 600 \ \overset{\circ}{A} \quad thick$$

Figure 1.1   Schematic diagram of an SNS microbridge.

with a metal stylus[5], patterned by depositing the films through a mechanical mask[6], or they can be tailored using lithographic techniques. The latter method was used almost exclusively in this work. The type of microbridge can be classified further: if the bridge region is composed of a normal metal, it is called a superconductor-normal-superconductor (SNS) microbridge; if the bridge is thinner than the banks, it is a variable-thickness microbridge (VTB); if both the bridge and the banks are the same thickness and the same material, it is a constriction-type (ScS) microbridge; and if the weak region is formed by underlying the weak region with a lower T_c material, it is a proximity-effect microbridge. There is one important point to be made here: SNS microbridges and proximity-effect microbridges are not the same. In the proximity-effect structure the bridge has a finite transition temperature, usually above 1K. In the SNS microbridge, the bridge does not become superconducting at any temperature.

1.1 Basic Theory of Microbridges

All of the basic phenomena of microbridges are the result of one fact: the order parameters of the opposed electrodes are coupled together in amplitude and in phase by the weak link. It is the nature of this coupling which determines the properties of any given junction.

1.1.1 Critical-current and current-phase relation

If the current through the junction is less than a critical supercurrent I_c, the coupling between the electrodes can be completely described by the current-phase relation $f(\phi)$. In this case the current is carried completely by the supercurrent I_s, where I_s is given by

$$I_s = I_c f(\phi).$$

For an ideal junction, $f(\phi) = \sin\phi$. For a non-ideal junction, $f(\phi)$ can deviate from the sinusoidal form, but it always has two properties: $f(\phi)$ is always an odd function, and $f(\phi)$ is always periodic with period $\Delta\phi = 2\pi$; $f(\phi)$ is not necessarily single-valued. Jackel[3] has made extensive measurements of $f(\phi)$ for several different types of microbridges, and his work contains an excellent discussion of the results.

The current-phase relation (CPR) of SNS microbridges has been theoretically studied in great detail. These theories are described in Chapter 4; they all have essentially the same result. Except for very short bridges at very low temperatures, the CPR should be sinusoidal. The microbridges of this work all had measured CPRs which were sinusoidal, in agreement with the theories. Thus, as far as the zero-voltage CPR is concerned, our microbridges were ideal.

The value of I_c depends, of course, on the cross-sectional area of the weak link. For sufficiently small links, I_c is inversely proportional to the normal-state resistance R of the bridge; thus, to eliminate the areal dependence of I_c, the value of $I_c R$ is usually reported. For an ideal microbridge, with banks and bridge made from the same material, the $I_c R$ product close to T_c should be given by[2]

$$I_c R = \alpha(T_c - T) \qquad \text{where } \alpha \simeq 635 \ \mu V/K.$$

At low temperatures, the $I_c R$ product should be independent of temperature, attaining, for small microbridges in the dirty limit, a maximum at $T = 0$ of $316 \ T_c$ microvolts, where T_c is in degrees K.[2]

For an SNS structure, on the other hand, close to T_c the $I_c R$ product

should be proportional[7] to $(T_c-T)^2$; at low temperatures I_cR should be nearly exponential with temperature.[17] We have compared the temperature dependence of I_cR for our samples to the predictions of the theories applicable to these samples, and we have found very good agreement. In fact, for $T < 0.6\ T_c$, our results agree both in form and in magnitude with the theory.

The above temperature dependences of I_cR are valid only for sufficiently small microbridges. For all-superconductor structures, if the bridge becomes much longer than the coherence length, the temperature dependence changes radically[2]; this is not the case for SNS structures. If the width of an all-superconductor microbridge is larger than the penetration depth, the I_cR product will be reduced due to the formation of vortices inside the bridge. This can also happen in SNS junctions; in fact, nearly all of the previous work on SNS layered junctions produced I_cR products which were limited at low temperatures due to the relatively large cross-sectional area of the bridge. This was not a problem in the SNS structures of this work, since for our samples the penetration depth is of the order of 1 mm[7], which is much larger than the width or thickness of the bridges used here.

1.1.2 Low-voltage phenomena

If a voltage V is present across the bridge, there are two additional factors which must be considered. First of all, in addition to the supercurrent there is a normal current through the junction, given by $I_n = V/R$. Second, the phase difference between the banks is now time-varying, with the variation given by $d\phi/dt = (2e/\hbar)V$. Thus, for an ideal

junction, the current through the junction is given by

$$I = I_s + I_n = I_c\sin\phi + V/R.$$

This model of an ideal junction is often called the resistively-shunted junction (RSJ) model. For this model the current versus voltage (I-V) characteristic is given by $V_{dc} = R(I_{dc}^2 - I_c^2)^{1/2}$.

The problem with the RSJ model is that no microbridge studied has ever had the I-V curve predicted by the RSJ model. The I-Vs of real microbridges often show hysteresis, bumps, curvature in the wrong direction, and other miscellaneous features. Most of these deviations from the RSJ model are caused by heating or by relaxation time effects. These effects have been described in detail by Likharev.[2]

It will be shown in Chapter 4 that our SNS junctions did not follow the predictions of the RSJ model. It will be shown that joule heating in the bridge was not important. Instead, it was found that these SNS structures had an intrinsic relaxation time which caused significant hysteresis in the I-V. We observed that the hysteresis could be characterized by the IR product at which the I-V returned to the zero-voltage axis. This characteristic IR product was independent of temperature at low temperatures, and the low-temperature value was proportional to the square of the reduced length of the bridge. Both of these phenomena are predicted by time-dependent Ginzburg-Landau calculations for SNS structures.

In addition, we found that the observed low-voltage curvature in the dc I-V could be correlated with the intrinsic relaxation time, although precise comparisons with theory could not be made.

1.1.3 <u>RF response of microbridges</u>

The fact that the supercurrent oscillates in time when there is a voltage across the bridge has led to a great number of experiments in which the microbridge is driven by an ac current as well as a dc current. Such experiments have produced two results. The first is that for small ac currents the critical current is increased above the value it had without an ac drive current. This enhancement has been studied intensively in the last few years, and our SNS results have led to a few surprises. For all superconductor microbridges it is widely believed that the ac field enhances the energy gap in the bridge, thereby increasing the critical current. However, the results of this work indicate that the enhancement in SNS structures is due to a spatial redistribution of the electrons in the bridge, rather than an increase in an energy gap. The evidence for this explanation lies in the very strong correlation between the effective relaxation time and the frequency of ac current required to increase the critical current.

The second phenomena observed when an ac current is applied is the observance of constant-voltage steps in the I-V curve. These steps occur at voltages which are multiples of the characteristic voltage $(\hbar/2e)\omega_{rf}$. (Henkels[4] has given a good review of this phenomena.) In this work, as well as in all previous works on microbridges, steps always occurred at multiples of this characteristic voltage. But for some frequencies steps also appeared at submultiples of this characteristic voltage. The minimum frequency at which these subharmonic steps occurred in this work was proportional to the effective relaxation time determined from the

reduced length of the bridge.

The major disagreement with the theory of rf-induced steps was in the magnitude of the steps. For frequencies above a frequency proportional to the effective relaxation time, there was strong disagreement.

In summary, we have discovered that the effective relaxation time determined from dc measurements was very important in predicting the ac response of our microbridges.

1.1.4 High-voltage effects

The relatively high resistance of our samples allowed us to measure the I-V characteristic at voltages above the gap voltage of the super-conducting electrodes; this regime had not been reached in previous studies of SNS structures. We found that, in contrast to the low-voltage measurements, the effect of the normal metal bridge on the electrodes was also important, in addition to the effect of the banks on the bridge. It was observed that the dV/dI curve had features which could be attributed to energy dissipation in the banks. Previous experimental workers have observed high-voltage structure in the I-V curves, but no previous experimental or theoretical work has considered the possibility of an extra high-voltage dissipation in the banks.

1.2 Sample Fabrication and Measurement

The very small length scale of superconductivity requires samples to be very small. To be more precise, the coherence length for a normal metal is given by $\xi_0(T) = (\hbar v_f \Lambda / 6\pi kT)^{1/2}$ where Λ is the electron mean free path. For the copper films used in this work, $\Lambda \simeq 15$ nm. (Λ was not measured directly; it was deduced by fitting the $I_c R$ versus T data

to the theory. A direct calculation from the resistance R and the physical dimensions of sample Pb-Cu-13 (R $\simeq$ .3 ohms, length L $\simeq$ 200 nm, width w $\simeq$ 200 nm, thickness d $\simeq$ 60 nm) gave a value of Λ = 25 nm. But this direct calculation is only approximate due to the uncertainty in the actual dimensions of the bridge.) This means that for T $\simeq$ 7K (the transition temperature of the lead banks) ξ_0(T=7K) $\simeq$ 40 nm. Now, in order to get useful samples we needed bridges whose lengths were of the order of 10 ξ_0(T=7K) or smaller. To achieve this, we could not use the traditional photo-lithography; instead, we developed our own version of electron-beam lithography. With this technique, we were able to achieve bridges of length L $\simeq$ 8 ξ_0(T=7K).

The fact that we were interested in samples composed of different materials led to difficulties in obtaining a good metallic contact between the different materials. This necessitated the introduction of a cleaning step (ion-bombardment) between the separate metal depositions.

We were also interested in various materials: tin, lead, niobium, aluminum, indium, and copper. To this end, both sputtering and thermal evaporation were used to deposit the films.

All together, several different combinations of materials were tried. The best results were obtained using lead for the superconducting electrodes, and copper for the normal-metal bridges. Only the results of these Pb-Cu-Pb structures will be presented here in detail. The results on the other structures will be briefly presented in Chapter 5.

The measurements performed were quite standard, at least in our laboratory. A discussion of the measurement techniques will therefore be

brief, with only those techniques novel to this work presented in detail.

Chapter 2

SAMPLE FABRICATION

One of the most time-consuming parts of this work was the preparation of samples. Thin film samples were required in which the planar dimensions were very small, of the order of 200 nm. Structures this small could not be reliably produced using photolithography, so an electron-beam lithography (EBL) system was developed; this system could produce structures with planar dimensions as small as 150 nm. In addition, several processing steps often occurred between film depositions, so that ion-beam etching or sputter etching had to be employed between depositions in order to achieve good metallic contact between successively deposited films.

The sequence of fabrication steps was usually the following: a gross-electrode structure was put onto a cleaned substrate using photolithography. The bridge component of the microbridge was then deposited using EBL and the lift-off method. Next, the banks component was laid down, also with EBL and the lift-off method. (In the case of niobium banks, the banks' geometry was sculptured with sputter etching.) Finally, the gross electrode structure was expanded and/or thickened, and the sample was ready for testing. This chapter is devoted to a detailed discussion of the various steps of this process.

2.1 Substrate-Selection and Cleaning

The first substrates employed were thin (.006 in) glass cover slips. These substrates did not prove to be satisfactory for two reasons: they were so thin that they broke very easily, and glass has

a very poor thermal conductivity. Good thermal conductivity is an important feature in a substrate since it aids in the cooling of the substrate during film depositions and it improves the performance of the microbridge laid upon it, although no experiments were done to meausre the importance of this latter advantage. Fused quartz was also tried (briefly) as a substrate, but although it has adequate strength it has a poor thermal conductivity. The final choice was sapphire, and it worked quite well as a substrate material. Single crystal sapphire is very strong, and its thermal conductivity is of the same order of magnitude as that of a metal at all temperatures of interest.

Single crystal sapphire substrates were obtained from Adolf Meller Co. with a standard polish on one side and an extra-fine polish on the side used for the sample. They came pre-cleaned, but an ultrasonic cleaning in isopropyl alcohol was necessary to remove any dust on the surface. Generally each substrate could be used only once, since some of the processing steps left resist residue which was impossible to remove completely using any available cleaning technique.

2.2 Photolithography and the Lift-off Technique

Most of the gross electrode structures were obtained using photo-lithography and the lift-off technique. This method has been in use for many years and a good explanation of it has been given by Henkels[4], but a brief discussion of the method is useful here. (Figure 2.1 depicts the method.)

First, a thin (200 nm to 1000 nm) film of photo resist was spun onto the substrate. (The substrate could have been clean, or it could

resist
substrate

1) coat substrate
with resist

resist
substrate

2) expose and
develop resist

metal
resist
substrate

3) evaporate metal

metal
substrate

4) strip resist

Figure 2.1   Diagram of the lift-off method for producing a patterned
thin film.

have had previously-defined thin film structures on it.) Shipley AZ1350B and Shipley AZ1350J positive resists were used. After application, the resist was baked at 80°C for ten minutes. A mask (either a film negative or a metal film on a transparent backing) was laid over the top, and the mask was held in intimate contact with the substrate in a vacuum chuck. Ultraviolet light was then shone through the mask. A high pressure mercury lamp with an incident flux of about 250 foot-candles gave exposure times of about three minutes. After the exposure, the mask was removed and the resist was developed in an aqueous developer; this developer removed the exposed areas of the resist.

After the resist stencil was completed, the lift-off method was employed: the desired metal film was evaporated over the top of the resist, then the resist was removed using a resist stripper (acetone); metal which was on top of the resist was removed along with the resist. Remaining on the substrate was the desired result--a metal film whose geometry was the same as that of the transparent area of the mask.

Although the photolithographic and lift-off techniques were relatively simple, they had significant drawbacks. The wavelength of the ultraviolet light limited the resolution to about 500 nm, a resolution which was not fine enough for the desired microbridges; electron-beam lithography was used to obtain finer resolution. In addition, the lift-off method was incompatible with the sputtering process used for the deposition of niobium films; in these cases it was necessary to use a sputter-etching technique to define the niobium films.

2.3 Electron-Beam Lithography

Electron-beam lithography (EBL)[8] is quite similar to photolithography; only the method of exposure is substantially different. In EBL, the resist is exposed by electrons in a scanning electron microscope (SEM). The resolution of EBL is determined not by the wavelength of the electrons (the electrons used have a wavelength of about .01 nm) but by the profile of the electron beam in the resist. The factors which determine this profile will be discussed later. The minimum resolution achieved in this work was about 150 nm.

2.3.1 Electron-beam resist

The resist used in this work was Dupont Elvacite 2041 (PMMA), a highly crossed-linked polymer (polymethylmethacrylate) with a mean molecular weight of about 500,000. The properties of this resist have been described in detail by Wolf et al.[9] The resist was obtained in powder form; the powder was dissolved in methyl isobutyl ketone (MIK), filtered through a Millipore filter, and spun onto a substrate at about 5000 rpm. It was found that a 4-1/2% (by weight) concentration of PMMA in MIK gave a resist thickness of about 300 nm; an 8% solution gave a thickness of about 600 nm. After application, the resist was baked at 100°C for one hour. (Baking at 160°C for one-half hour gave better adhesion and slightly better exposure characteristics, but this baking temperature proved to be damaging to metal films which may have been present under the resist.) The 8% solution proved to be markedly non-uniform, so thicker resist coatings were produced by applying more than one coat of the 4-1/2% solution; the samples were baked for one-half hour

between coats and for one hour after the final coat. Two coats of 4-1/2% solution gave a thickness of about 550 nm and three coats of 4-1/2% solution gave a thickness of about 800 nm. After baking, 10 nm of aluminum was evaporated onto the sample to prevent charging in the SEM.

After exposing the resist in the SEM, the resist was developed with the following procedure:

Soak in 0.1 Molar NaOH to remove Al coating.

Rinse in distilled water.

Develop in 3:1 isopropyl alcohol:MIK for 30 sec to 5 minutes.

Ultrasonic 3:1 isopropyl alcohol:MIK for 5 sec.

Rinse in isopropyl alcohol.

Spin dry.

Because PMMA is a positive resist, the areas of the resist exposed to the electron beam were removed by the development process. After development, the samples were ready for the deposition step.

2.3.2 Electron-beam exposure system

Resolution

The electron-beam resist coatings were exposed in an AMR Model 1000 scanning electron microscope (SEM). This microscope had a minimum probe diameter of about 20 nm, but its usual resolution was about 50 nm. This resolution was sufficient for all the samples produced, since the minimum pattern size in the resist was governed by the scattering of electrons in the resist. The electrons had an energy of 20 keV, and at this energy the scattering in the resist, neglecting substrate effects, limited the resolution of the exposed pattern to about one-fourth the

thickness of the resist. If the substrate had been coated with a moderate to high density material, this minimum feature size could be increased to about one-half the resist thickness (or larger).[10] This scattering limit could have been reduced by using an SEM with a higher accelerating voltage.[9]

Registration

PMMA has a relatively low sensitivity to electrons; as a result, the EBL system could only expose relatively small areas. (An area 1 mm by 1 mm square required a minimum of one hour to expose.) Much larger areas were required for making the electrical contacts necessary for testing. For some of the samples, the gross electrode structure was put on the substrate prior to the EBL steps. In other cases, ones in which the necessary electrodes could not survive the EBL procedure, small silver pads were put on the substrate to aid in the registration of the EBL exposure; silver was used because it was easy to evaporate, stood up to the EBL processing steps, and has a high electron cross section, thus providing a good image in the SEM. These silver pads were especially useful in the banks' exposure, since the thin bridge lines were very hard to locate without these registration pads. Figure 2.2 shows a few of the gross electrode/registration structures which were used.

These registration markers were also very useful for focusing. The usual procedure was to position the sample at low magnification, move slightly away with either the electrostatic beam shift or the mechanical stage translation, go to high magnification to focus, reposition at low magnification, and then expose at high magnification. It was not possible to focus directly at the place to be exposed, since this
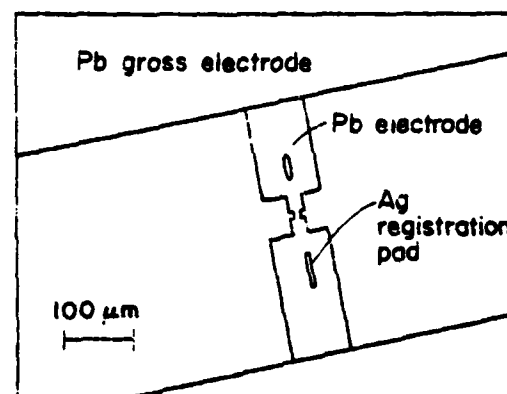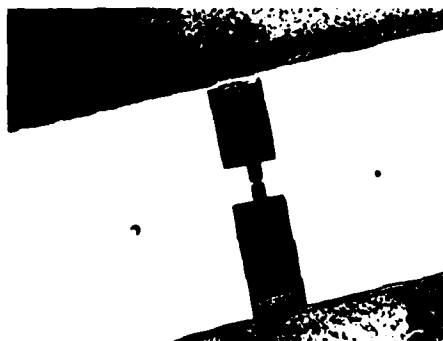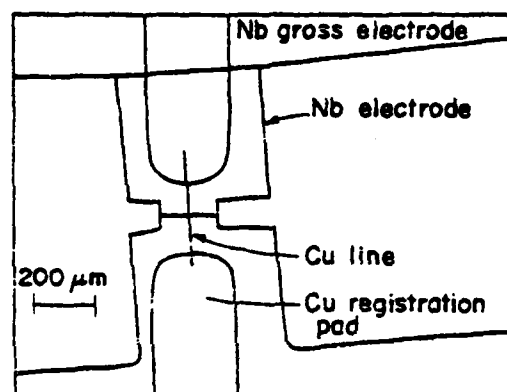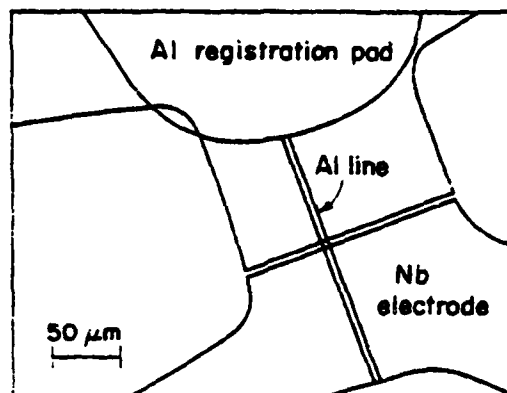
Figure 2.2 Registration pads and electrode structures for three samples.
Top - Nb-Al-4.3; middle - Nb-Cu-1/4; bottom - Pb-Cu-13.
The gross electrodes were patterned using an aluminum-foil
stencil; the electrodes and registration pads were
lithographically produced.

focusing would expose the resist in an unwanted pattern. The focusing
had to be done close to the desired exposure location since the SEM could
not keep its resolution over a large area of the sample. If there wasn't
a registration pad close enough to focus on, a minute or so of exposure
at the highest magnification (100,000 X) would blister the resist and
thus create a defect to focus on.

Line exposure

The SEM had a fair amount of noise (mostly at 60 Hz) in the scan
generator-deflection coil circuits. Because of this, the finest pattern
which could be drawn was a line in the resist, exposed in a single pass.
For many purposes (such as the bridge line exposures or the gap patterns
for sputter etching) a single line was quite satisfactory. Such lines
were drawn with the SEM in line-scan mode. The beam was blanked except for
a portion of a single line scan; it was important to blank both the begin-
ning and end of a line in order to avoid the irregularities which the
scan generator put at either end. In this mode, the necessary exposure
was about 1.3×10^{-8} coul/cm. (At a specimen current of 1.3×10^{-10} amps,
a .02 cm line could be drawn in 2 sec.)

Rectangle exposure

The microbridges which were fabricated were very small; the bridge
region which required the fine resolution occupied an area of about 100
square microns. Since the gross electrode structures had gaps of about
1 mm, it was usually necessary to expose large rectangles (~ 1 mm^2) which
required only relatively poor resolution. This was most easily done at
low magnification in the partial scan mode of the SEM. Relatively high

beam currents were used (4×10^{-10} amps) and gaps of about 5 microns could be left between rectangles. Figure 2.3 shows the use of such rectangles in the production of a Pb-Cu-Pb microbridge. The beam blank was not required during the exposure of these large rectangles.

Pattern exposure--the flying spot scanner

Patterns which required detail finer than 5 microns and which could not be constructed from a few single line scans were exposed with the SEM in its raster mode. In this mode the beam scanned the sample in a raster consisting of a number of horizontal lines. The pattern was generated by blanking the beam when it covered areas which were not to be exposed. This selective blanking of the beam was accomplished with a flying spot scanner (FSS), depicted in Figure 2.4.

A film mask was made in the same geometry as the desired pattern, but on a greatly magnified scale. (The magnification of the mask was the SEM magnification at which the exposure was to be done; i.e., if the exposure was to be done at 10,000 X, one centimeter on the mask would be one micron on the sample; the record screen had dimensions of 10 cm by 10 cm.) This mask was then placed over the record screen of the SEM, and a photomultiplier was used to detect whether or not the record screen could be seen through the mask. If the record scope trace was behind a transparent region of the mask, the SEM electron beam was left on; if the record trace was behind an opaque area of the mask, the SEM beam was blanked. Since the trace of the record scope was slaved to the same raster as the SEM beam, the SEM beam was blanked according to the mask pattern, and the resist was exposed in the mask pattern, <u>at a reduction corresponding to the magnification of the SEM used during the exposure</u>.

100 μm wide, 600 μm high

$I = 4 \times 10^{-10}$ amps, 4 min.

(Partial scan mode)

30 μm wide, 60 μm high

$I = 4 \times 10^{-11}$ amps, 40 seconds

(Partial scan mode)

10 μm wide, 4 μm high

$I = 9 \times 10^{-12}$ amps

(FSS mode)
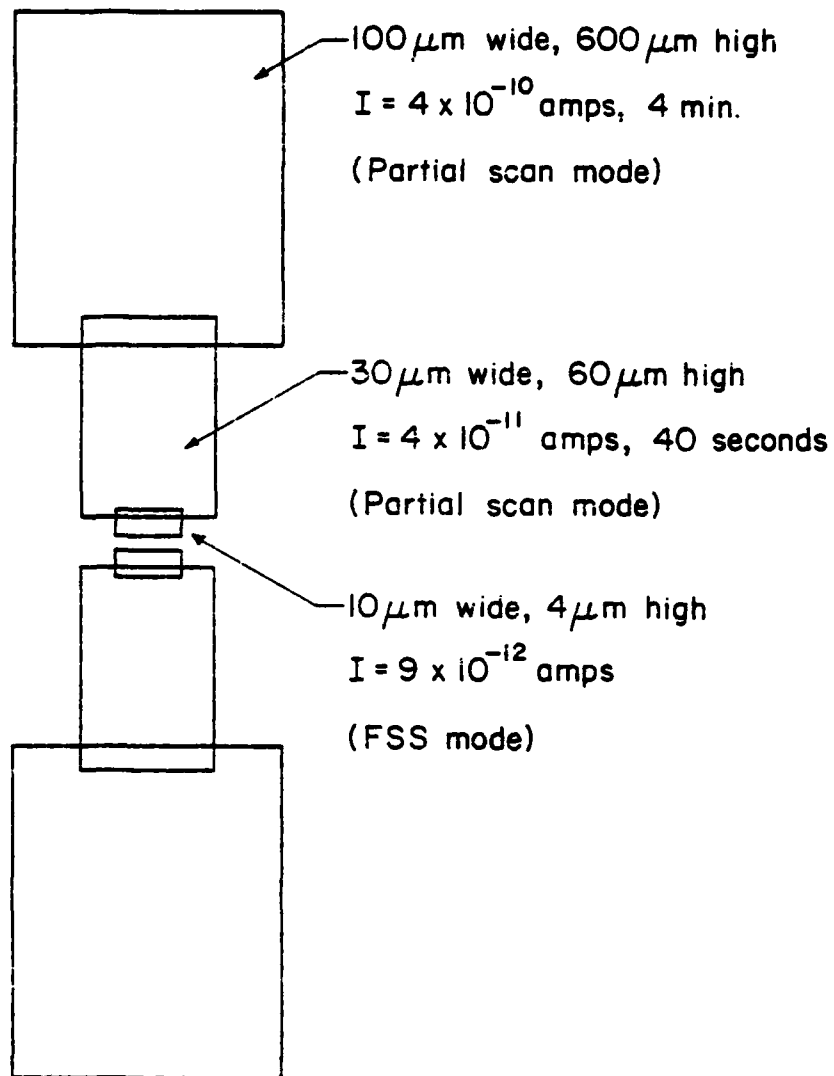
Figure 2.3 Diagram of the procedure for generating electrode structures using electron-beam lithography. Figure 2.2 (bottom) shows an example of the results of this procedure.
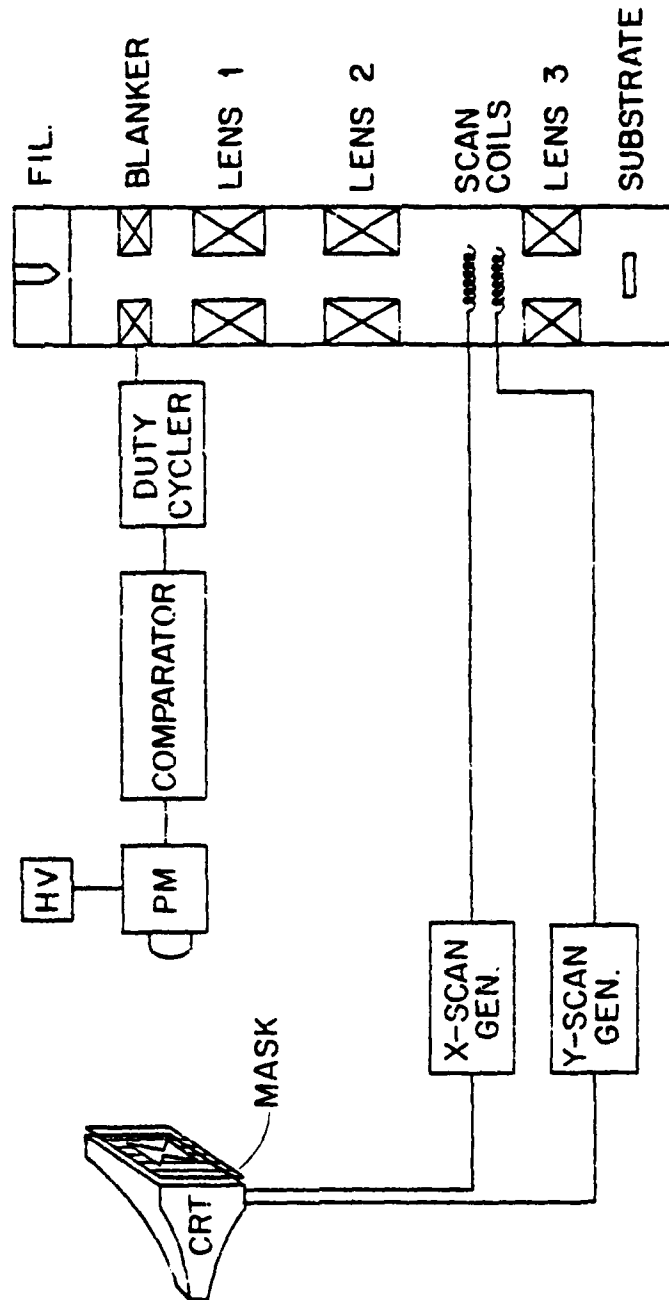
Figure 2.4 Schematic diagram of the flying-spot scanner system (FSS).

For example, if the SEM was used at a magnification of 10,000 X, the pattern was reduced by a factor of 10,000 in a single step.

The circuit used to interface the photomultiplier to the beam blank on the SEM is shown in Figures 2.5 and 2.6. The SEM required 0 volts to have the beam on, and +5 volts to blank the beam. This circuit contained a threshold detector to eliminate the zero offset and noise present in the photomultiplier output. It also contained the options of blanking the beam completely, or of leaving the beam completely unblanked. The circuit was also designed to duty cycle the beam while it was in the "beam on" state in order to reduce the current in the beam; this feature was seldom used since it had adverse effects on the resolution. The photomultiplier was run with about one kilovolt between the first dynode and the anode, and a standard resistor network was used for biasing the intermediate dynodes. The best performance of the flying spot scanner was achieved with the record scope contrast at a minimum.

The best resolution was obtained with an SEM magnification of 10,000 X. At this magnification, a sample current of about 9×10^{-12} amps was used. The horizontal lines had a scan time of .013 sec/line; the frame scan time was 24 sec. In this mode, as well as in the rectangle-exposure mode, the PMMA had a sensitivity of about 1.8×10^{-4} C/cm^2.

The most important consideration in the design of the flying spot scanner was its resolution; the resolution was characterized by the minimum mask dimension which could be resolved. This resolution was determined by both geometrical and response-time factors. There were three geometrical factors:
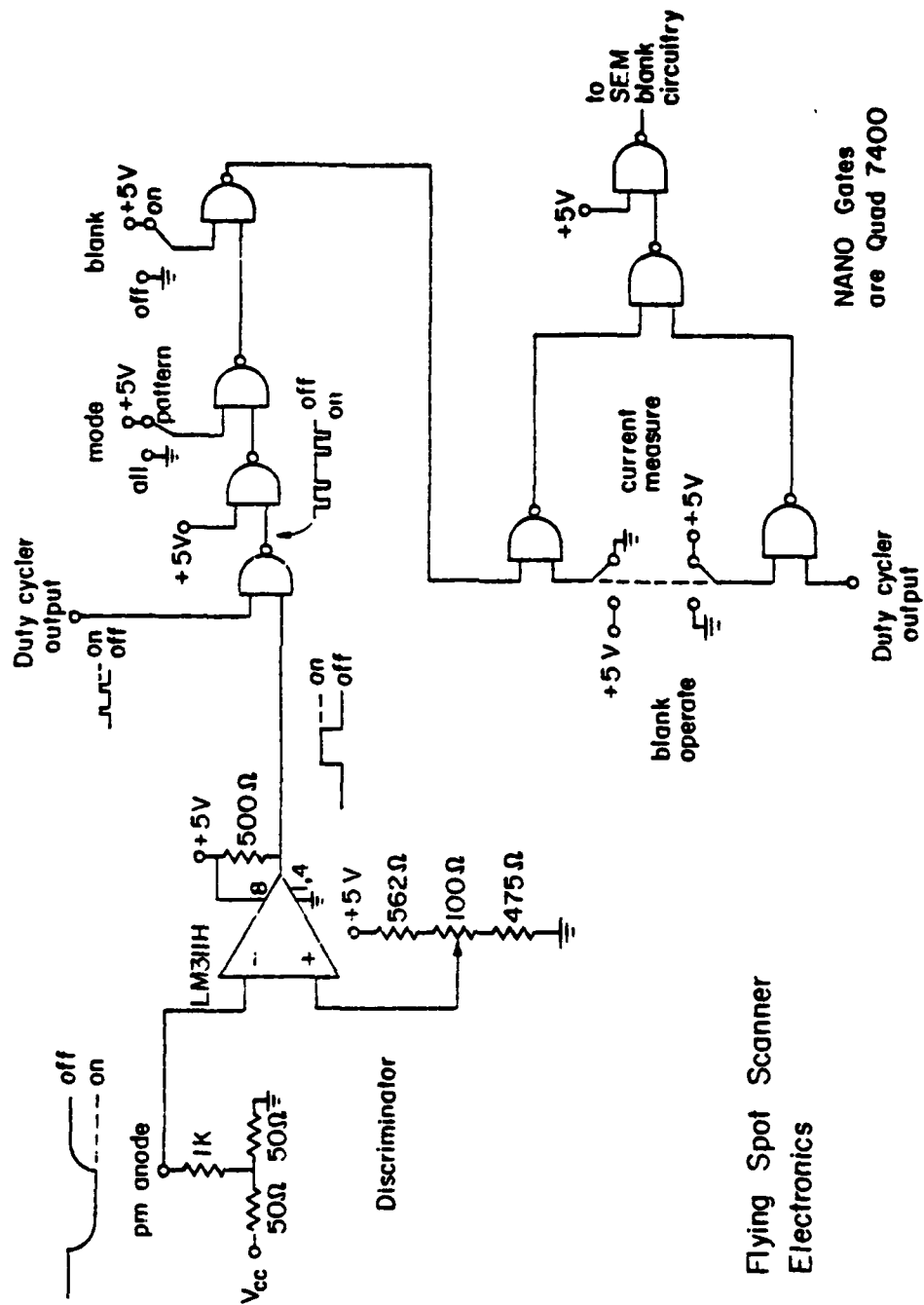
Figure 2.5 Schematic diagram of the flying-spot scanner electronics.

Duty Cycler for FSS
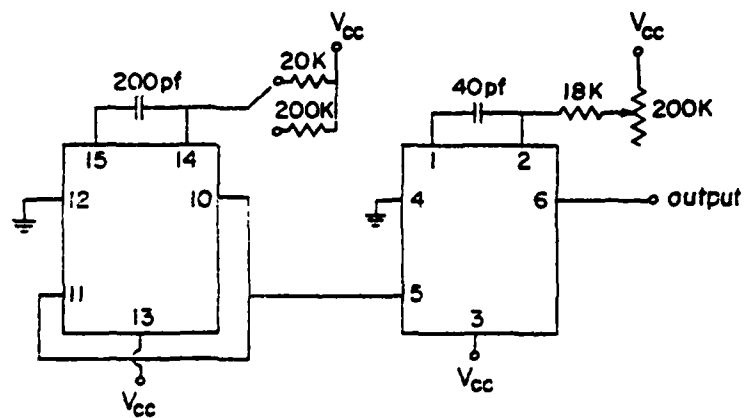
output is ⊓_⊓__⊓_ --- +5V on
0 off

pulse freq = 0.06 or 0.6 MHz

pulse width is 400 ns to 4 μs

IC is Fairchild 96L02C

Figure 2.6 Schematic diagram of the duty-cycler electronics for the FSS.

Resolution of the film mask--using Kodalith graphics film gave a resolution of about 50 microns.

Resolution of the record scope--the SEM's record scope had a resolution of 50 microns or less, as long as the intensity was not set too high.

Parallax caused by the fact that there was about 1/4 in of glass between the phosphor on the inside of the record screen and the film mask--placing the photomultiplier 24 in from the mask and using a one inch aperture at the photomultiplier reduced this error to a few microns. Parallax also caused quite a bit of distortion in the pattern, but this distortion was not important in the structures used in this work. The use of lenses between the mask and the record screen and between the photomultiplier and the mask could have significantly reduced the distortion as well as eliminated the need for such a large spacing between the photomultiplier and the mask.

These geometrical limits were quite small; the significant limitation on the FSS resolution was due to response-time considerations. A response time in the system affected the resolution because if the system took a time t_r to respond to changes in light intensity, there would be a resolution limit of ds $= t_r$ dx/dt where dx/dt is the speed of the record scope beam across the record screen. There were two response times of interest in the system:

Delays in the photomultiplier, in the threshold detector and in the SEM's beam blank circuitry--the total of these delays was about one microsecond. This delay was much smaller than the other response time, and thus posed no significant limitation. In fact, the major effect of

this delay was a lateral shift in the pattern; this was a form of distortion and was easily corrected.

Record screen phosphor decay time--this was the significant limitation on the FSS resolution. The phosphor used (type P11) had a decay time of about 50 microseconds. At a sample current of 10^{-11} amps and a magnification of 10,000 X, the horizontal sweep of the beam on the record screen had to be about 800 cm/sec. This gave a resolution limit of .04 cm on the record screen, or 40 nm on the sample. (All exposed areas were thus 40 nm larger in the horizontal dimension than they would have been without this resolution problem.) This was the resolution limit of the flying spot scanner system. The use of a record scope tube with a faster phosphor would have increased the resolution dramatically.

This resolution of the flying spot scanner was not the factor which limited the minimum size of the microbridges produced. As mentioned above, the scattering of the electrons in the resist limited the minimum size of the exposed pattern to about one-fourth of the resist thickness.[10] In all samples produced this scattering limitation was larger than the flying spot scanner limitation.

The flying spot scanner system worked quite well in practice; Figure 2.7 shows a structure produced using this system.

2.4 Thin Film Deposition and Etching

2.4.1 Thermal evaporation

Thin films of Pb, Sn, In, Al, Cu, Cr, and Ag were produced in a standard evaporator. The source to substrate distance was 20 cm, and the
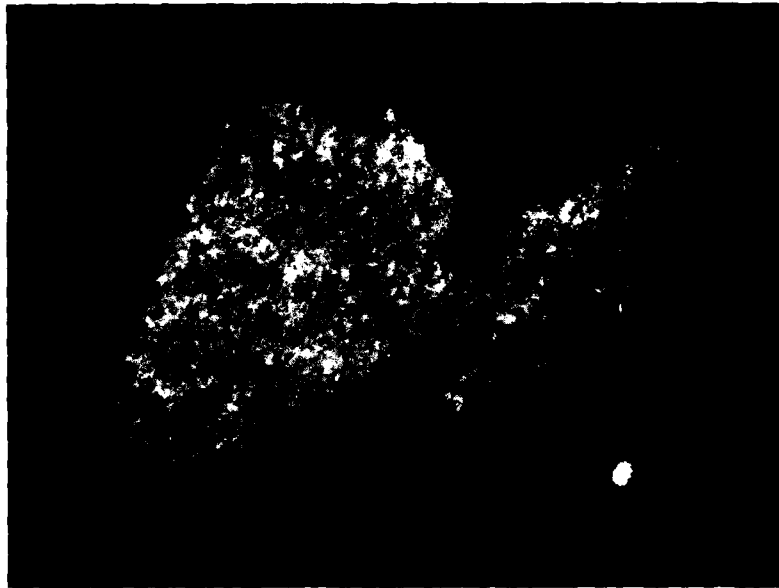
1 μm

Figure 2.7   Uniform-thickness tin microbridge produced with EBL.
The tin is about 100 nm thick.

thickness was monitored with an Edwards film thickness monitor. The substrates were cooled with liquid nitrogen to about 100°K. Base pressures before evaporation were about 1×10^{-6} Torr.

Al films were deposited from resistively heated tungsten baskets, at a rate of about 1 nm/sec. Cr films were deposited from heated Cr-plated tungsten rods, at a rate of about 1 nm/sec. Pb, Sn, In, Au, and Ag were deposited from heated tantalum boats, at rates ranging from 50 nm/sec for lead down to 10 nm/sec for Cu.

It was essential to cool the substrates and to evaporate the films as fast as possible for two reasons: it was necessary have grain sizes less than 100 nm, and the resist stencils could not tolerate much heating.

All of the films produced by thermal evaporation were patterned using the lift-off method.

2.4.2 Ion-beam cleaning

The production of the Pb-Cu-Pb microbridges required that the Cu bridge films be cleaned immediately before the Pb-bank films were deposited in order to remove the oxide on the copper and the resist residue remaining from the copper-stripe fabrication step. This cleaning was accomplished using the ion mill depicted in Figure 2.8. The ion source was purchased from Ion-Tech Inc.; the electronics were constructed in-house from a circuit which was nearly the same as the circuit provided by Ion-Tech. The ion beam had a diameter of 2.5 cm at the source, and a diameter of about 10 cm at the substrates. Thermal evaporation sources were placed alongside the ion mill so that films could be deposited just after the ion cleaning was done without breaking the the vacuum.

The Cu films were ion-cleaned for 150 sec at an accelerating voltage of 600 volts and an ion-current density of about 0.2 ma/cm^2 at the substrate. It was estimated from Cu sputtering-yield data[11] that about 10 nm of Cu was removed by this cleaning. The pressure before cleaning was less than 1×10^{-6} Torr; the argon pressure in the bell jar was about 5×10^{-4} Torr. One advantage of this ion-cleaning was that the Pb films deposited after ion-cleaning were much more adherent than Pb films deposited without this cleaning step.

Immediately after the cleaning, the ion mill was shut off, the argon flow was stopped, and the Pb was evaporated. This switch-over from ion cleaning to film evaporation took about 10 sec; this delay did not seem to cause any noticeable problems in the Pb-Cu interface. Production of Pb-Al-Pb microbridges in the same fashion was attempted, but a good Pb-Al interface could not be obtained. Either the Al oxide was not removed completely, or the Al was re-oxidizing during the switch-over between cleaning and evaporation.

2.4.3 Sputter deposition and etching of Nb films

The very high melting temperature of niobium prevented the thermal evaporation of niobium in the available apparatus, so niobium films were produced by sputter deposition. A Varian rf-diode sputtering system was used. This system had a base pressure of 2×10^{-7} Torr, and the turbo-pump used did not have to be throttled during sputtering; the contaminating residual gases were thus kept to a minimum. The sputtering gas was argon at a pressure of 10^{-2} Torr. The films were bias-sputter deposited at a cathode potential of 1600 volts, a substrate potential of 40 volts, and an input power of 500 watts. The deposition rate was

determined by interferometric methods to be 0.65 nm/sec; since this rate was very repeatable, films of a desired thickness were made by sputtering for a pre-determined time interval. Although the substrate table was water-cooled, previous measurements[12] indicated that during deposition the substrate temperature could rise as high as 250°C. The films produced in this system were of high quality: films 100 nm thick had a T_c of 9.1 K and a resistance ratio of 4; films 35 nm thick had a T_c of 5.6 K and a resistance ratio of 3.

A few attempts were made to use the lift-off method with these films, but the sputtering process proved to damage the resist so badly that the films would not lift off. Consequently, sputter etching was used to pattern the niobium films after they were deposited. Both the electron-beam resist and aluminum were used as etch masks. The sputter-etching was done in argon at 5×10^{-3} Torr, with a substrate potential of 500 volts and an input power of 100 watts. The etch rate was about .086 nm/sec; this etch rate was not as repoducible as the deposition rate, so consecutive etches, each etch much shorter than the previous etch, were used to obtain the desired removed thickness of niobium.

The sputter etching could also be used to clean the substrate and/or previously deposited films since it was not necessary to break the vacuum between sputter etching and sputter deposition.

2.5 Fabrication Details of Specific Samples

2.5.1 Dayem bridges

The first samples produced in this research effort were uniform thickness (Dayem) tin bridges, an example of which is shown in Figure 2.7.

These samples were produced using the flying spot scanner and a single
tin deposition. Although these samples were quite small (500 nm wide
by 500 nm long) their performance was only mediocre. Because of this
poor performance they were studied only briefly.

2.5.2 Indium variable-thickness bridges

Indium variable-thickness microbridges (Figure 2.9) were produced in
a two-step process, both steps using EBL and the lift-off method. First,
the indium bridge line was laid down using the line-exposure EBL tech-
nique; these bridge lines were about 80 nm thick. Next, the indium banks
were laid down using the flying spot scanner technique; these films were
about 300 nm thick. These microbridges had very poor performance, probably
due to very bad interfaces between the bridge films and the banks films;
no cleaning steps were used between the two indium depositions.

2.5.3 Pb-Cu-Pb microbridges

The most successful microbridges produced were those in which the
birdge was made from copper and the banks were made from lead (Figure
2.10). The fabrication process for these bridges was the following:
First, two registration pads were put on the substrate; these pads
were made using photolithography and the lift-off technique. The pads
were about 10 microns wide and 150 microns apart; they consisted of 80
nm of silver on top of 20 nm of chromium.

Next, the copper bridge line (200 microns long, about 0.2 micron
wide) was placed between the registration pads using line-exposure EBL
and the lift-off method. The copper line was about 60 nm thick.

After the bridge line deposition, the resist stencil for the banks
was put down. This pattern, shown in Figure 2.3, was done in a series of
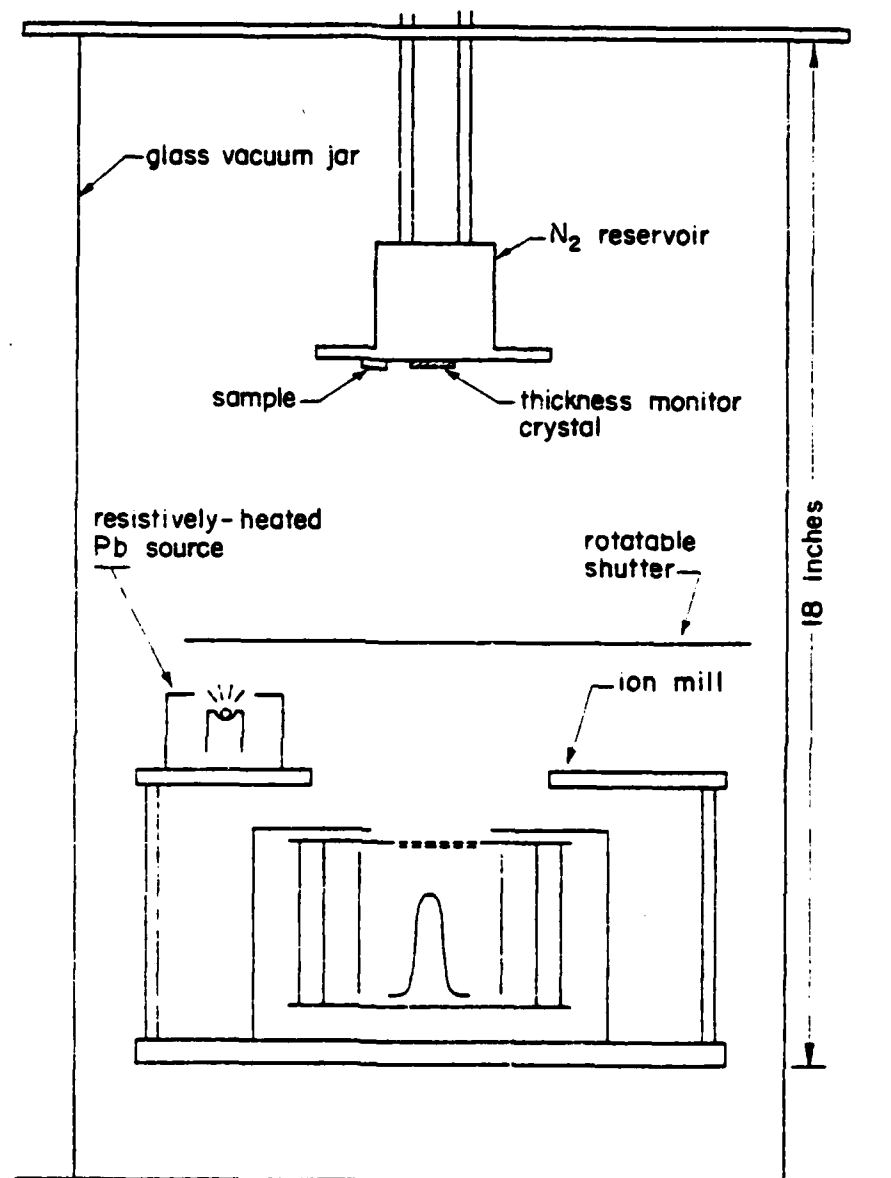
Figure 2.8   Diagram of the ion mill - evaporator system.

1 μm
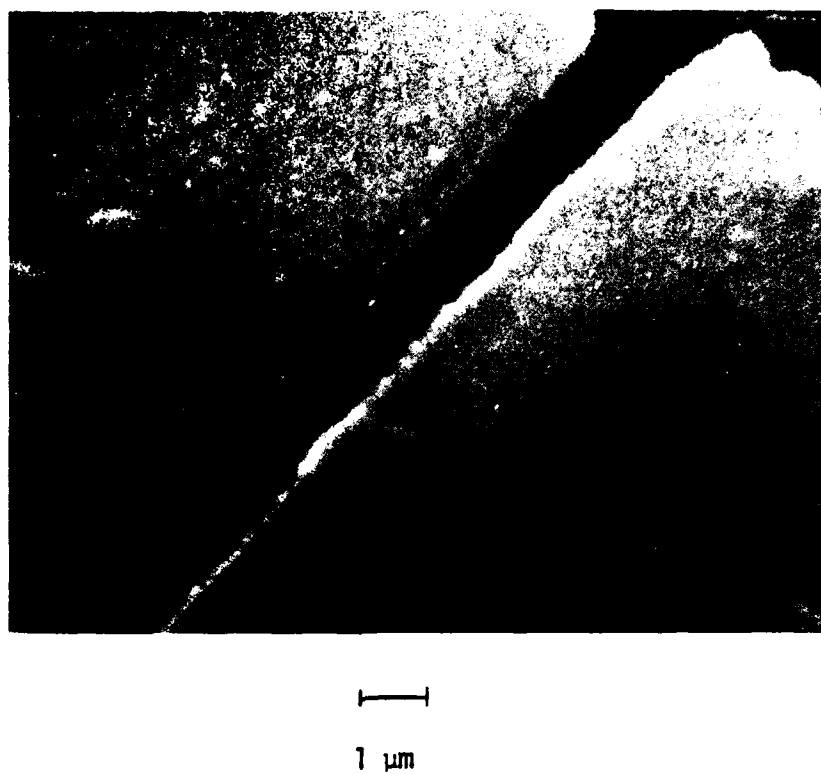
Figure 2.9 Indium variable-thickness microbridge. The bridge is
about 80 nm thick and the banks are about 250 nm thick.

Figure 2.10 Lead-copper SNS microbridge. Although the banks seem to be shorted together, electrical measurements showed that they are not (Pb-Cu-7).

three consecutive exposures; the first exposure was done with the flying spot scanner at a magnification of 10,000 X. The second and third exposures were done in the rectangle-exposure mode, at mangifications of 1000 X and 100 X, respectively. After development, the copper was ion cleaned, the lead banks (about 150 nm thick) were evaporated, and then the unwanted lead was lifted off by dissolving the resist.

The final fabrication step was the deposition of the gross electrodes. A narrow ($\sim$0.5 mm) strip of aluminum foil was taped over the bridge, leaving both ends of the lead banks sticking out. The exposed lead was then ion cleaned and about one micron of lead was deposited; the protective aluminum foil strip was then removed and the sample was ready for testing.

2.5.4 Nb-Cu-Nb and Nb-Al-Nb microbridges

Microbridges which had a bridge made of aluminum or copper and banks made of niobium were produced using a combination of the lift-off method and the sputter-etch method to pattern the films. First, registration pads and the bridge line were laid down in a fashion similar to the procedure used for the Pb-Cu-Pb structures; in these cases the copper films were 40 nm thick and the aluminum films were 40 nm thick.

Next, the bridge was cleaned by sputter-etching and a niobium film (65 nm thick) was deposited through a tantalum foil mask; this mask patterned the niobium film in the gross electrode structure (Figure 2.2). Note that this niobium film completely covered the bridge line.

After the niobium deposition, the rectangle-exposure and the line-exposure EBL modes were used to produce the PMMA etch mask on top of the

niobium film; the niobium was then sputter etched to form the bank geometry. Care had to be taken during this etch in order that all the niobium was etched out of the gap but the bridge was not etched through. Because the PMMA sputter etched three times faster than the niobium, and because the resist could only be about 300 nm thick, the niobium banks had to be less than 100 nm thick. In addition, the sputter-etching process hardened the resist making it difficult to remove; fortunately this unsightly resist residue did not affect the microbridge's performance.

Finally, thick ($\approx$ 1 micron) gross niobium electrodes were deposited using a technique similar to that used for the final gross electrode fabrication of the Pb-Cu-Pb microbridges, except that sputter etching and sputter deposition were used. An example of the final result is shown in Figure 2.11.

The performance of these Nb-Cu-Nb and Nb-Al-Nb microbridges will be discussed in Chapter 5. In general, the bridges had long effective lengths as a result of short electron mean free paths in the bridges. These samples had relatively small $I_c R$ products, and the Nb-Al-Nb samples had poor response to microwave radiation.

2.5.5 Nb-Nb-Nb microbridges

Variable-thickness microbridges in which both the bridge and the banks were niobium were produced by depositing a niobium film and then using sputter-etching to produce both the bridge and the banks. First, a niobium film (100 nm thick) was deposited thorugh a tantalum mask. Next, a thin aluminum line (40 nm thick) was laid over the top using

200 nm
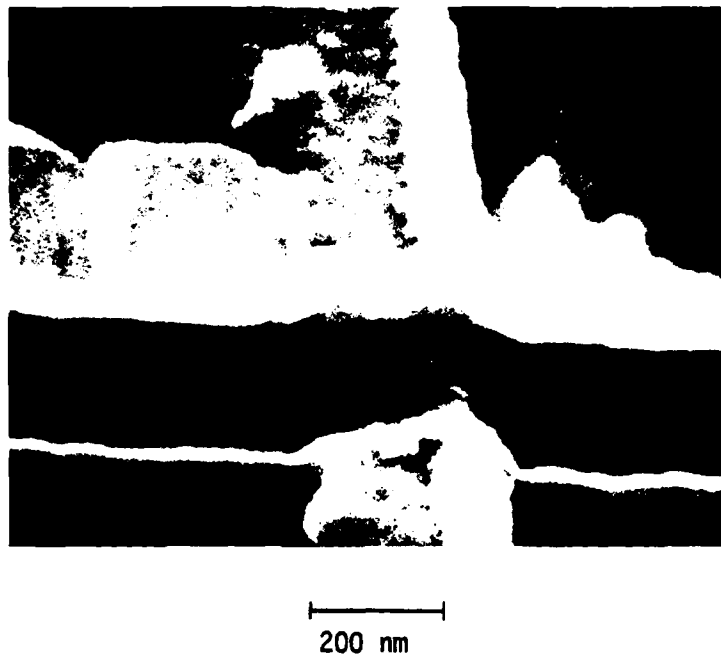
Figure 2.11 Niobium-copper SNS microbridge.

line-exposure EBL and lift-off. This line was used as an etch mask to form a raised line in the niobium by sputter-etching away about 35 nm of the niobium. The aluminum was then removed in NaOH.

Next, the gap for the banks was sputter etched in a fashion similar to that used to produce the gap in the niobium in the Nb-Cu-Nb structures. Again care had to be taken to ensure that the etch was long enough to remove all the niobium in the gap, but not so long that the bridge (corresponding to the raised portion of the niobium) was not etched completely away. Since both aluminum and PMMA etch much faster than niobium, the original niobium films had to be less than 100 nm thick. This meant that the bridge and banks were relatively thin compared to the length and width of the bridge, resulting in poor performance for these microbridges. Figure 2.12 shows one of the bridges of this type, and Figure 2.13 shows a photograph of one of these samples.

1 μm

Figure 2.12   Niobium variable-thickness microbridge.   The bridge is
about 25 nm thick and the banks are about 60 nm thick
(Nb37-2).

Figure 2.13 Photograph of the sample shown in Figure 2.12.

Chapter 3

MEASUREMENT APPARATUS AND TECHNIQUES

The measurement of the electrical properties of the microbridges required an apparatus to cool the samples and electronics with which to make the actual measurements. Since our laboratory has had many years of experience in cryogenic technology, obtaining a cryostat in which to cool the samples was relatively straightforward. On the other hand, the electronics used in this work was somewhat different from that used previously in our laboratory, primarily due to the fact that the quality of the electronic equipment available was constantly improving. In light of these facts, the cryogenic apparatus will be dealt with in a general manner, while the electronics will be discussed in more detail.

3.1 The Cryostat

The cryostat used in this work was originally built by Dr. James Lukens, but many changes have been made to it since his work. Jackel[3] has described the construction and operation of this cryostat in detail. Since we made no changes in the thermal construction and operation of this apparatus, the reader is referred to Jackel for a description of these aspects. Almost all of our alterations concerned the electrical wiring of the cryostat, and these aspects will be considered here.

Figure 3.1 shows a schematic diagram of the lower part of the cryostat; only the electrical features are shown in detail. There were two distinct sets of electrical connections to be made; the first was the dc current and dc voltage connection, and the second was the

Figure 3.1   Schematic diagram of the lower portion of the cryostat.
For clarity most of the temperature control components
have not been included.

Stainless steel tube

.l4l in. stainless steel semi-rigid coax

Brass I,V leads

4.2 K filters

Vacuum can pump-out line

Hermetic OSM feedthrough

Indium seals

Nb I, V leads

Stainless steel coax with thermal isolation loop

Terminal block

Hermetic OSM feedthrough

Indium seals

Nb I, V leads

Lead-plated lid

OSM connector

"Relia-Tac" connector

Copper semi-rigid coax

Copper I, V leads

Rf loop

Phenolic sample holder

Lead-plated can for shielding

"Relia-Tac" connector

Exchange gas can

Vacuum can

Figure 3.1

microwave connection. In implementing both of these sets of connections it was necessary to preserve the vacuum integrity of the vacuum can and the exchange-gas can, as well as preserving the weakness of the thermal connection between these two cans.

3.1.1 Sample holder

Figure 3.2 shows a schematic diagram of the sample holder. The sample was clamped between the phenolic block and a piece of transparent epoxy, with the electrical connections made by spring-loaded indium-coated brass pins. The epoxy piece was made transparent so that the sample could be observed during mounting to ensure that the pins made contact at the correction locations. This sample holder worked very well; there was seldom a loss of electrical contact during thermal cycling, and the sample could be removed and then remounted at a later date for additional testing. A photograph of this holder is shown in Figure 3.3.

3.1.2 DC I-V wiring

The dc I-V wiring can be seen in Figure 3.1. Because the micro-bridges were quite small, they had to be protected against burn-out caused by high-frequency induced currents. To protect the sample, a low-pass filter was placed in series with the I-V leads. This filter is shown in Figure 3.4. These filters effectively shorted out the sample at frequencies above about 1 kHz, while allowing dc measurements to be performed below about 1 kHz; this upper limit on the measurement frequency was not a hindrance to the measurements.

In order to protect the sample from dc current surges when the electronics was connected, a room-temperature shorting box was put at the

SAMPLE HOLDER FOR
I-V MEASUREMENTS
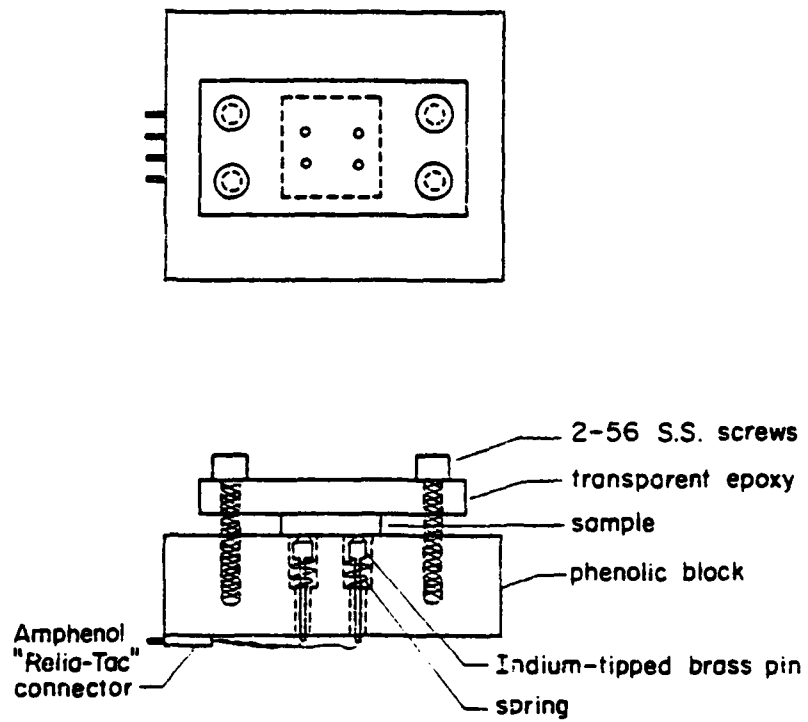
Figure 3.2 Schematic diagram of the sample holder.

Figure 3.3 Photograph of the sample holder.

Cryostat Wiring
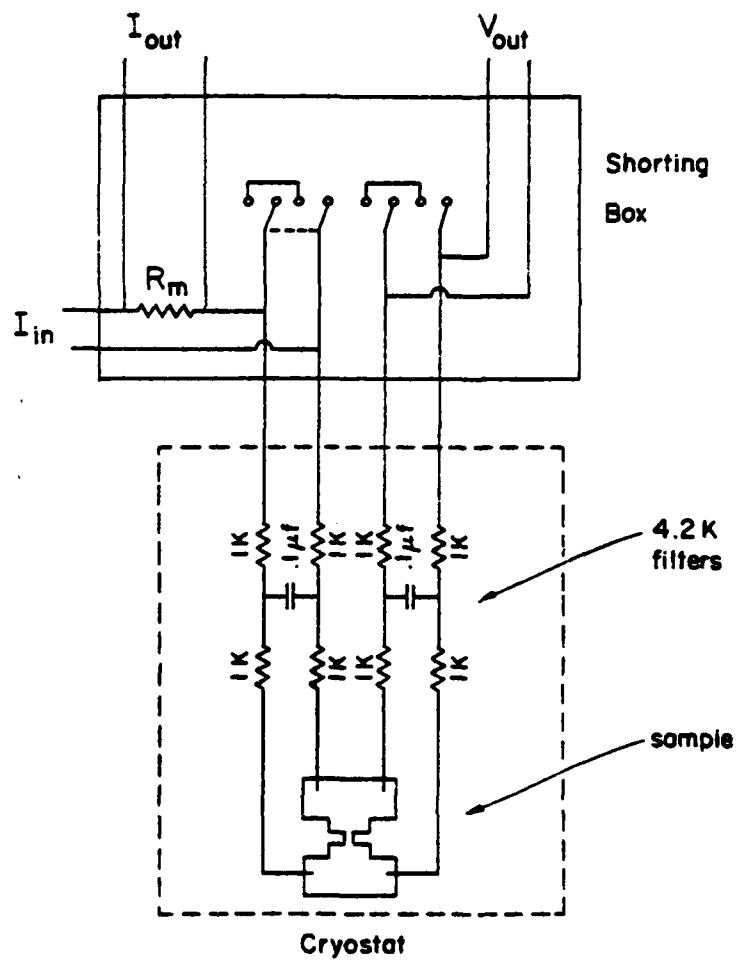
Figure 3.4   Schematic diagram of the low-temperature filters and
the room-temperature shorting box.

top of the cryostat. This box had a switch which could short the I leads together and the V leads together while the electronics was being connected, and then isolate the leads while measurements were made. This box is depicted in Figure 3.4.

To obtain the required thermal isolation, the I-V leads were brass from room-temperature down to the 4.2K filters, niobium from the filters down to the shielding can, and copper from there to the sample holder. The wires were fed through the vacuum can and the exchange-gas can via vacuum-tight epoxy feed-throughs.

3.1.3 Microwave connection

The sample could be fed by a microwave current by inductively coupling the sample to a microwave coaxial line via a loop which terminated the line. Although no serious attempt was made to optimize this coupling, sufficient coupling was produced for our purposes. The coaxial line had a silver-plated steel inner conductor and a stainless-steel outer conductor from room temperature down to the shielding can. Although this coax had a fairly high attenuation, it was necessary in order to achieve the desired thermal isolation. From the shielding can to the sample both the inner and outer conductors were made of copper.

3.1.4 Measurements below 1.5K

This cryostat was useful down to about 1.5K. In order to make dc I-V measurements down to about 0.5K, a cryostat which was cooled by pumped ^{3}He was used; this cryostat was cheerfully provided by Alan Kleinsasser.

3.2 Electronics

Several different configurations of electronics were used since different types of measurement were made. In general, since the voltages and currents of interest were small (as low as 100 nA and 100 nV), it was necessary to use the lowest-noise electronics available. But, since the available electronics quite often produced a small signal-to-noise ratio, it was often necessary to average the measurements for long periods of time.

Extreme care was taken to minimize the effects of an electrically noisy environment. The dewar was in a shielded enclosure, and most of the electronics were placed, along with the dewar, in a shielded room. Digital electronics had to be kept outside the shielded room due to their excessive noise radiation. In order to reduce 60 Hz noise, which the shielded room could not screen out, all wires were either twisted pairs or triaxial shielded cable. Ground loops were very carefully eliminated by having all circuits grounded at only one point.

3.2.1 Basic I-V measurement system

Figure 3.5 shows the basic configuration for dc I-V measurements or dV/dI measurements. The sample was current biased by a current source (shown in Figure 3.6). This current source produced a current ramp, or it converted a voltage ramp from a triangular oscillator into a current ramp. The current was measured by a current-monitoring resistor (CMR); either a resistor in the current source or a resistor in the shorting box was used for a CMR. The voltage across the CMR was fed into the input of a PAR 113 low-noise differential amplifier and the output of the 113
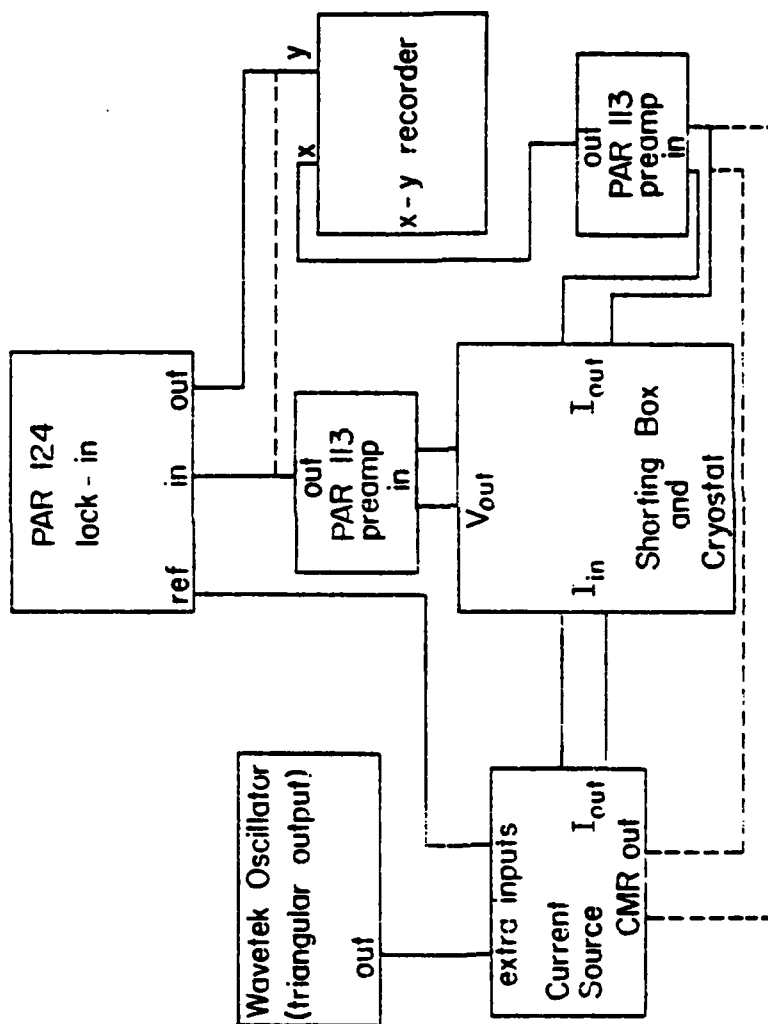
Figure 3.5 Schematic diagram of the basic measurement electronics.
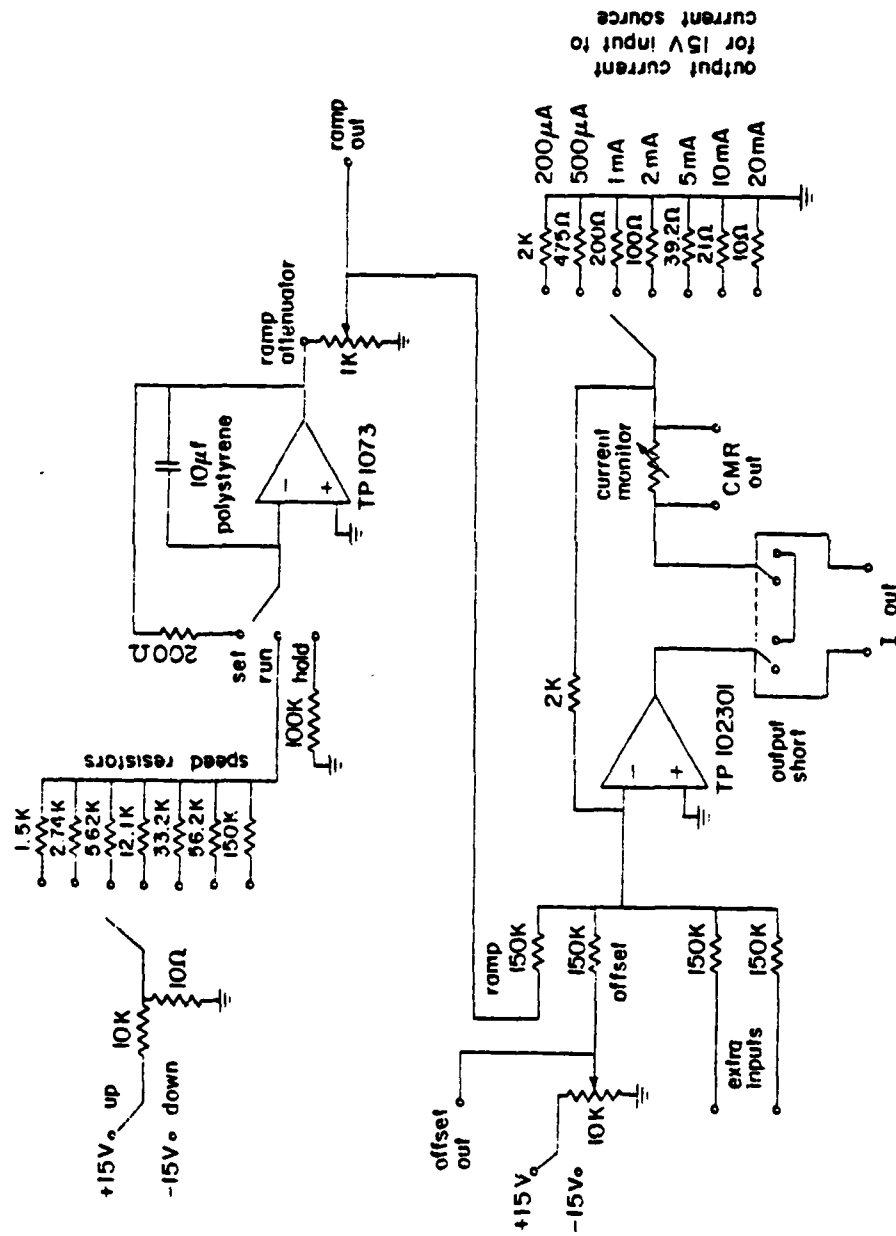
Figure 3.6 Schematic diagram of the current source.

went into the horizontal axis of an x-y recorder.

The voltage across the sample was fed directly into a PAR 113 pre-amplifier, and the output of this 113 went into the vertical axis of the x-y recorder.

For dV/dI measurements, a small ac voltage (from the reference of a PAR 124 lock-in amplifier) was also fed into the current source, resulting in a small ac component to the sample bias current. (Usually, an ac frequency of 1 kHz was used, with an ac magnitude of about one percent of the peak bias current.) The output of the voltage-measuring PAR 113 was now fed into the vertical axis of the x-y recorder. The signal from the voltage 113 and the dV/dI were plotted on the same piece of paper, resulting in curves like the ones shown in Figure 3.7.

The basic problem with this configuration was that if the signal-to-noise level was small, very slow ramps were necessary. Not only was it difficult to generate very slow ramps, but the dc drift in the pre-amplifiers put a lower limit on the speed of the ramp.

3.2.2 Digital data acquisition

Because of the problem with dc drifts in the preamplifiers, a digital data acquisition system was often used. This system is shown in Figure 3.8. In this setup, the dc current-ramp biasing the sample was repeated many times, the corresponding voltage or dV/dI curves for each separate ramp were added together digitally with a Northern signal averager. If the time for one complete ramp was less than the characteristic dc drift time of the preamp, the dc drift of the preamp would appear as a constant offset in the averaged curve. Thus the system allowed the data to be averaged over long periods of time without the

Pb-Cu-13
5.67 K

2 mV
2.5 mA
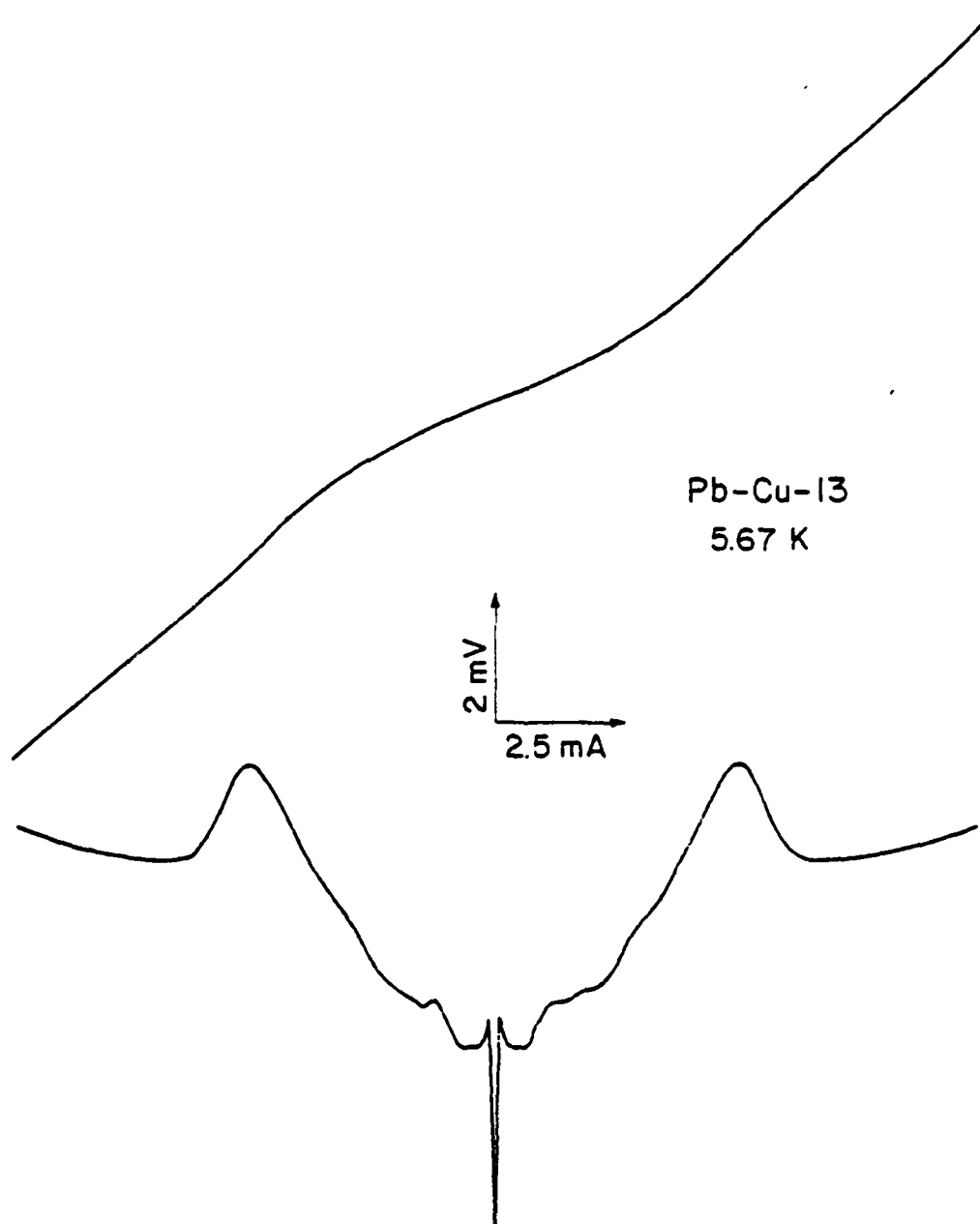
Figure 3.7 Typical high-voltage I-V and dV/dI curves generated with
the basic electronics configuration. The curves are
symmetric about the I = 0 point. Both curves have the
same current (horizontal) scale; the vertical scale for
dV/dI is in arbitrary units.
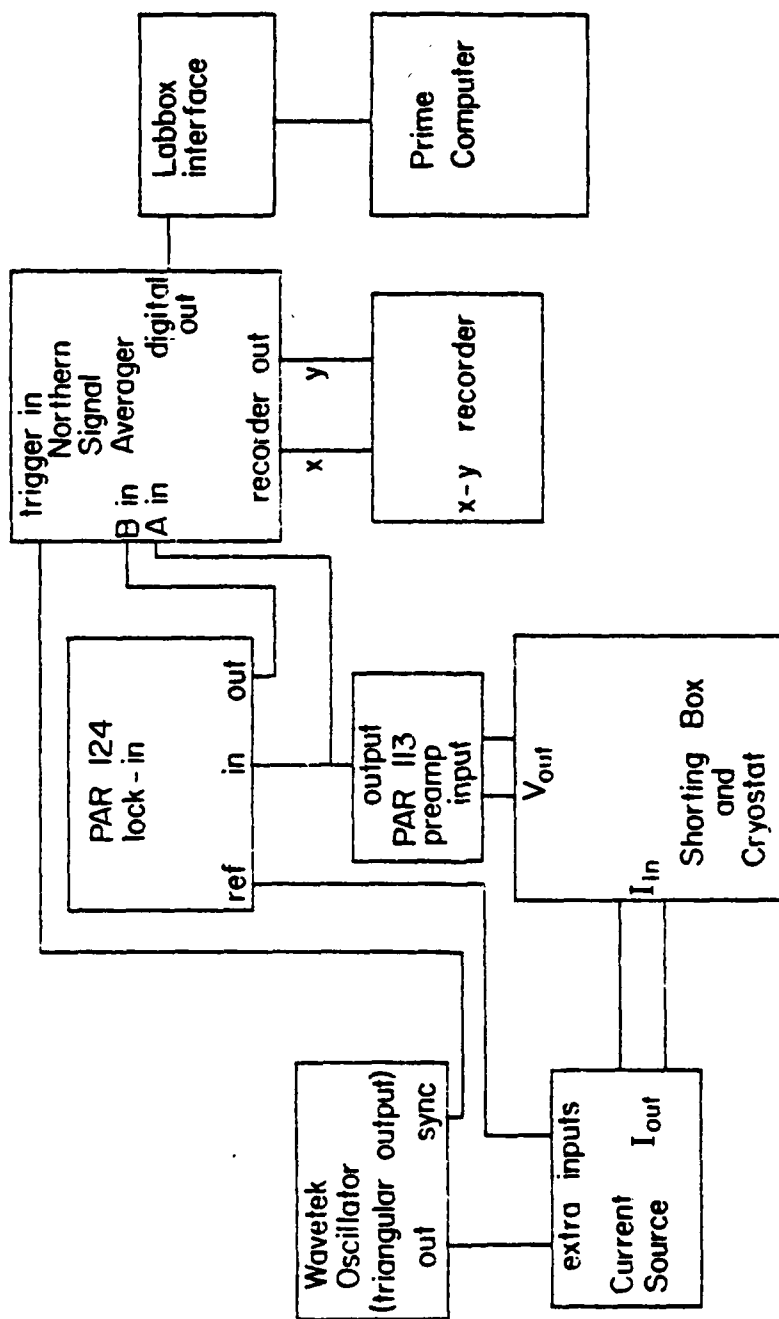
Figure 3.8 Schematic diagram of the digital data acquisition system.

dc drift changing the shape of the curves.

In this configuration the sample bias current was not measured directly, but was measured by assuming the current to be proportional to the amount of time since the sync pulse of the oscillator producing the ramp.

For most of the data taken in this work the digitally-averaged data were far superior to the data produced using the more basic system; in fact, nearly all of the experimental data presented in this thesis was taken using this system. This digital configuration was not without its problems, however. The most serious disadvantage was that the zero of the vertical axis was not known; in fact, the offset from zero varied from one curve to the next. This prevented using this system to determine the temperature dependence of the magnitude of dV/dI; the more basic system had to be used in this case.

Another serious disadvantage was that hysteresis in the data was not easily observed. To observe hysteresis, it was necessary to separately average the curves for increasing bias current and the curves for decreasing bias current, and then compare the averaged curves. This was something of a nuisance.

The digital system was not as accurate as the more basic system. The non-linearity in the A-D converter of the signal averager was about one percent. In addition, the gain of the signal averager was not accurately known; the peak-to-peak voltage of the output of the preamp had to be measured on an oscilloscope to determine the gain. A similar measurement had to be done to measure the current gain.

3.2.3 Digital data processing

One advantage of the digital data acquisition system was that the data could not only be plotted on an x-y recorder, but it could also be sent directly to a Prime computer. This allowed the data to be manipulated by the computer before it was plotted out. For example, in measuring the dV/dI data the direct result was a curve of dV/dI versus current. But since the signal averager could simultaneously acquire both the dV/dI versus current curve and the voltage versus current curve, it was easy to program the computer to plot dV/dI versus voltage. The dV/dI versus voltage curves presented in Chapter 4 were obtained in this way.

It was also possible to derive dV/dI versus voltage curves from voltage versus current curves with the computer. An example of this is shown in Figure 3.9. In this way it was possible to make precise measurements of the voltages $V_{inflection}$ and V_{lower} discussed in Chapter 4.

Having the data stored in the computer also made it possible to replot the data at any time, at any scale; if necessary, very small regions of a curve could be blown up, or two different curves could be compared. This was very useful in analyzing the data, since it was possible to look at features of the data which were not necessarily considered noteworthy when the data was taken.

3.2.4 Microwave electronics

Figure 3.10 shows a schematic of the electronics used to bias the sample with an rf current. For frequencies less than 9 GHz, a TWT oscillator was used as a source of microwaves. In this case the post-directional-coupler attenuator was held constant, and the pre-directional-coupler attenuator was changed to vary the magnitude of the applied rf.
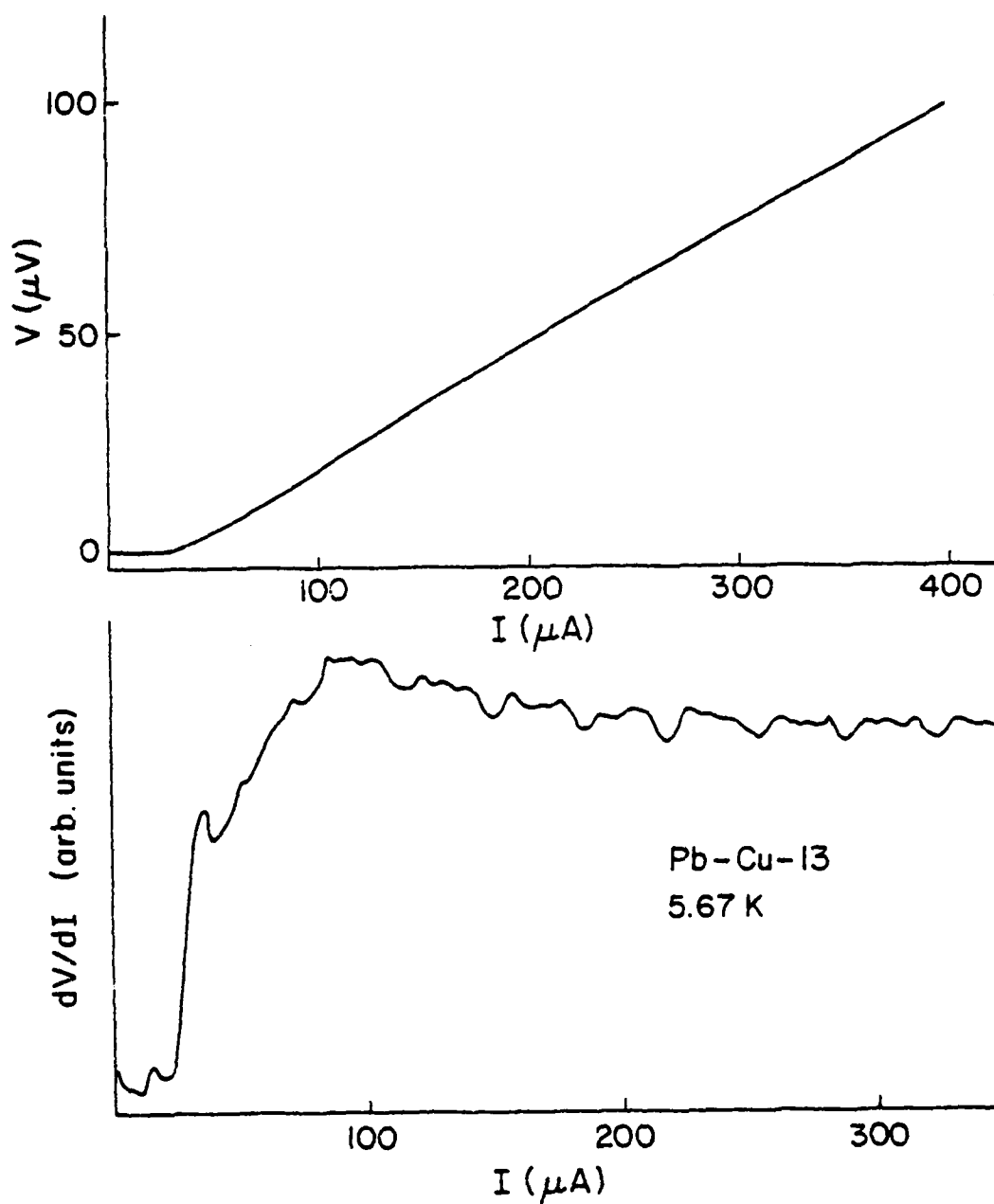
Figure 3.9   Low-voltage I-V and dV/dI curves obtained with the digital data acquisition system. The dV/dI curve was generated by a numerical differentiation of the I-V curve.
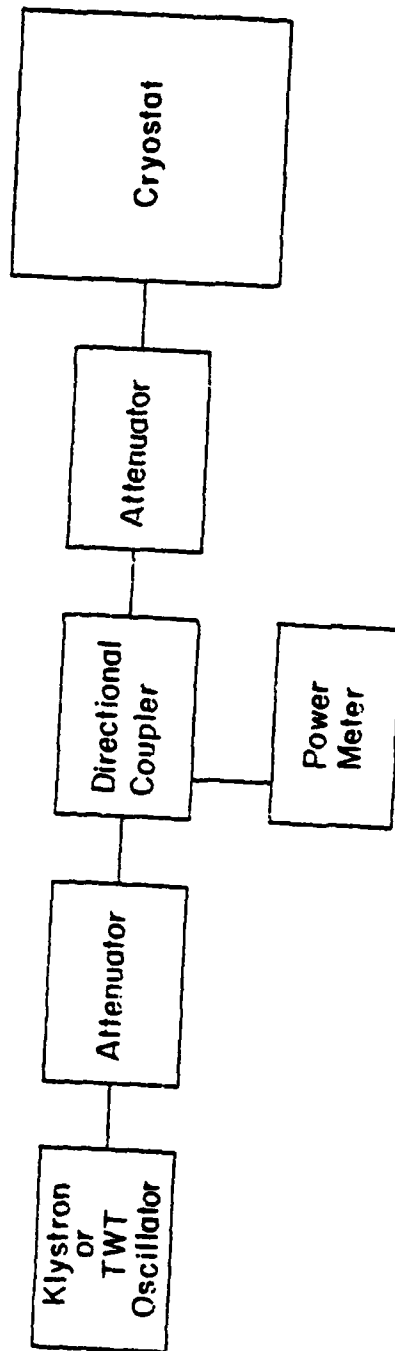
Figure 3.10 Schematic diagram of the microwave electronics.

The power (or, equivalently, the magnitude of the rf current) was deter-mined by observing the power meter. For these frequencies all of the components were connected by coaxial lines.

For frequencies above 9 GHz a klystron was used as a microwave source. In this case the magnitude of the applied rf was varied by changing the post-direction-coupler attenuator, and the power applied to the sample was measured by noting the attenuator setting. The pre-directional-coupler attenuator was used to hold the power to the post-directional-coupler attenuator constant, as measured by the power meter. For these frequencies all of the components up to the final attenuator were connected by rectangular waveguide, in order to minimize excess attentation. A waveguide-to-coax adaptor was inserted between the final attenuator and the cryostat's coaxial line.

For all frequencies, it was necessary to tune the frequency for maximum rf power coupled into the sample because of the strong mismatches present in the cryostat's coaxial lines and the mismatch between the terminating loop and the sample.

Chapter 4

RESULTS ON Pb-Cu-Pb JUNCTIONS

The measurements of the electrical properties of the SNS junctions
produced in this work were multi-faceted; in light of this, the results
are arranged here in separate sections, with the appropriate theoretical
and experimental backgrounds presented with each separate aspect of the
observed results. This division of results is somewhat artificial,
however, in that the behavior seen in one type of measurement was often
very useful in understanding the results of other measurements. Some
of the results were fairly simple in nature, and the understanding of
these results was relatively simple. Other results were complex, and
the understanding of these results was correspondingly complex. A few
of the measurements showed quite unexpected effects, and some of these
effects are still poorly understood.

4.1 Temperature Dependence of the Critical Current

    4.1.1 Theory

The existence of supercurrents in an SNS microbridge at first
thought seems surprising since the bridge is made from a normal metal.
After all, the electron-phonon interaction responsible for super-
conductivity has a range of only a few interatomic distances[13] and
allowing for retardation effects only increases the interaction length
to about 20 nm; the microbridges produced in this work had normal-
metal bridges 200 nm long or longer. The answer, of course, is that
there is still a coupling between the superconducting banks. This
coupling is due to the fact that a superconducting bank imposes on the

normal bridge a change in the density of states. It is important to note that this change in the density of states does not include an induced energy gap in the normal metal.[14]

The bank also induces a correlation in the electron distribution in the normal metal. In the superconductor some of the electrons are paired in states of opposite momentum; this pairing between electrons extends into the normal metal (proximity effect). This correlation decays exponentially with distance into the normal metal, with the decay length given by

$$\xi(T) = \left[\frac{\hbar v_f \Lambda}{6\pi kT}\right]^{1/2}$$

(v_f = fermi velocity in the normal metal, Λ = electron mean free path in the bridge). In spite of this decay, the opposite superconductor still "sees" some of this correlation; i.e., the two superconductors are coupled together. It is this coupling which gives rise to supercurrents in the normal metal. Figure 4.1 illustrates this idea.

Putting this electron-correlation picture of SNS structures on a firm theoretical footing has been the subject of a great deal of work. The calculation of the density of states near the interface will be discussed later in this chapter. The calculation of the critical current has been carried out using several different methods.

Microscopic treatments for clean systems (mean free path much greater than the junction length) were performed by Kulik[15], Ishii[16], Bardeen and Johnson[17], and Bezuglyi et al.[18] Ishii restricted himself to the T=0 K case. The remainder of these authors predicted that I_c should be
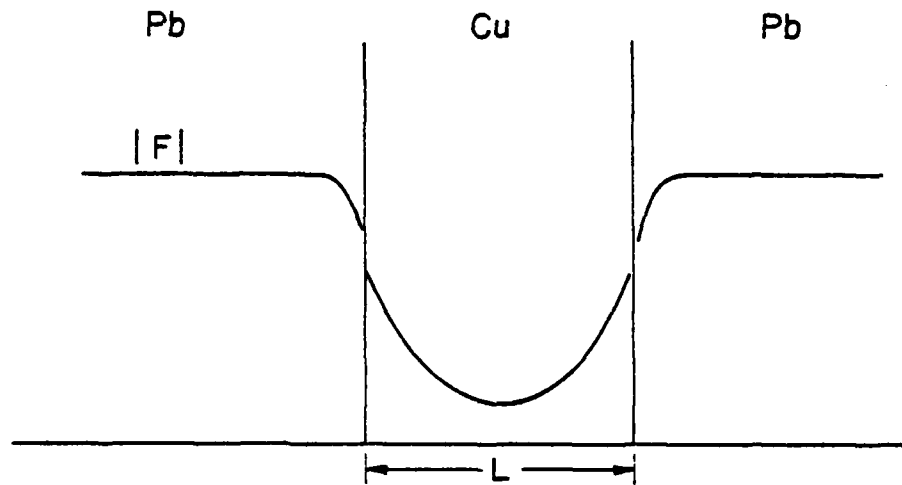
Figure 4.1 Schematic diagram of the spatial variation of the paired-electron density ($|F|$) in a SNS microbridge.

proportional to e^{-T}.

Kulik and Mitsai[19] microscopically calculated I_c versus T for a moderately dirty ($\xi_0 \ll \Lambda \ll L$) junction and found $I_c \sim \exp -[(\frac{2\hbar}{\xi_0} + \frac{L}{\Lambda})]$.

DeGennes[7] used a Ginzburg-Landau treatment for the banks and a microscopic treatment for the bridge and found $I_c \sim (1 - T/T_c)^2$, where T_c is the transition temperature of the banks.

Fink[20], using Ginzburg-Landau theory for both bridge and banks, found $I_c \sim (1 - T/T_c)^n$ where $1 \leq n \leq 2$. The calculations of both deGennes and Fink are restricted to the dirty limit near T_c.

Likharev[21] has done a microscopic calculation in the dirty limit using the equations of Usadel.[22] Since this calculation has been very useful in this work, it will be explained here in some detail. In this theory the correlation picture of superconductivity is put on a rigorous footing by defining a correlation parameter

$$F(\vec{r}) = \langle \psi_\uparrow(\vec{r}) \psi_\downarrow(\vec{r}) \rangle$$

where $\psi(\vec{r})$ is the one-electron operator. $F(\vec{r})$ is thus the probability of finding two electrons in the condensed (correlated) state at the point $\vec{r}$. Usadel developed a set of diffusion-like equations for determining F. He used the expression for F obtained in the temperature-dependent Green's function method; thus he derived an infinite set of equations. For a one-dimensional system like the microbridges produced here, Usadel's equations reduce to

$$2\omega F(\omega,x) - D \frac{d}{dx} \left\{ [1 - |F(\omega,x)|^2]^{1/2} \frac{dF(\omega,x)}{dx} \right.$$
$$\left. + \frac{1}{2} \frac{F(\omega,x)}{[1 - |F(\omega,x)|^2]^{1/2}} \frac{d|F(\omega,x)|^2}{dx} \right\} = 2\Delta(x) [1 - |F(\omega,x)|^2]^{1/2}$$

where $D = \frac{v_f \Lambda}{3}$ is the diffusion constant (v_f = fermi velocity, Λ = electron mean free path), ω = Matsubara frequency = $(2n+1)\pi kT$ (n a non-negative integer), and

$$\Delta(x) = \lambda N(0) 2\pi kT \sum_{\omega > 0} <F(\omega,x)>$$

($N(0)$ = density of states at fermi surface, λ = interaction constant). Note that all of these equations are coupled together via the expression for Δ; this coupling makes the general solution to these equations extremely difficult to obtain. But for a normal metal $\lambda = 0$, a fact which uncouples the equations and greatly simplifies finding the solution.

Usadel also found the expression for the supercurrent density to be

$$j_s(x) = 2ieN(0)\pi TD \sum_{\omega > 0} F^*(\omega,x) \frac{d}{dx} F(\omega,x) - F(\omega,x)[\frac{d}{dx} F(\omega,x)]^*$$

It is important to note that these equations of Usadel are valid only in the dirty limit.

Following Likharev we obtained the solution to these equations by numerical integration; these calculations provided an $I_c R$ versus T relation which depends on the length of the bridge. Figure 4.2 shows the results of Likharev's calculations. We duplicated Likharev's calculations in order to get precise theoretical curves with which to fit our data; the details of these numerical calculations are given in the Appendix. In these calculations it was necessary to impose boundary conditions on F at the superconductor-normal metal interface. We assumed that $|F|$ at the boundary had the same value as it did in the bulk of the super-conductor; i.e.
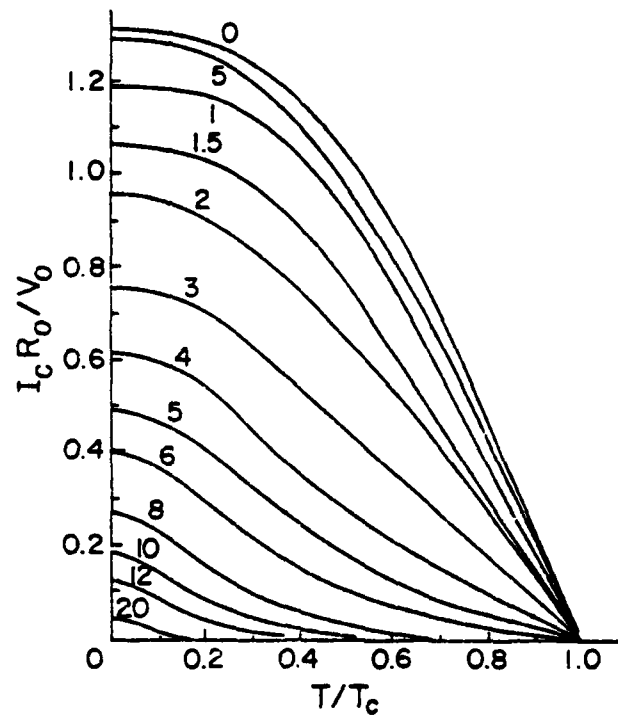
Figure 4.2 Theoretical calculation of the temperature dependence
of I_cR_0 (from Ref. 10).

$$|F_\omega|_{banks} = \frac{\Delta(T)}{[\omega^2 + \Delta(T)^2]^{\frac{1}{2}}}$$

where $\Delta(T)$ is the temperature-dependent gap in the bulk of the super-conductor. This assumption is not valid near T_c where the gap in the superconductor is depressed near the bridge due to the proximity of the normal-metal bridge. DeGennes[7] has calculated this depression, but application of his boundary condition to this problem was not attempted since it requires a better knowledge of the nature of the bank-bridge interface than we had available.

These equations for F are somewhat simplified if lengths are scaled in units of the decay length (coherence length)

$$\xi(T) = \left(\frac{\hbar v_f \Lambda}{6\pi kT}\right)^{\frac{1}{2}}$$

Thus a bridge of physical length L can be said to have a reduced length $\ell = \frac{L}{\xi(T_{c-banks})}$; i.e., the length of the bridge in units of the value of the decay length at the transition temperature of the banks.

4.1.2 Previous experimental work

There have been two previous measurements made of the I_c versus T relation for SNS junctions. Clarke[23] made measurements on layered (as opposed to planar) Pb-Cu-Pb junctions. His junctions had a cross-sectional area of about .04 mm^2. He found $I_c \sim (1 - T/T_c)^2$ between about 6.5 K and 7.0 K, in agreement with the theory of deGennes.[7] Below this temperature range the critical current was limited by its own magnetic field due to the relatively large size of the junctions.

Shepherd[24] also measured layered Pb-Cu-Pb junctions; his samples had an area of about .1 mm^2. He found that $I_c \sim e^{-T}$ for $3K \le T \le 5K$.

Since his samples were in the clean limit, this result is in agreement with
the microscopic calculations for clean junctions. Below 5K the critical
current of his samples was self-limited.

The most significant difference between these previous experiments
and the measurements of this work is in the size of the junctions.
DeGennes[7] has calculated that for a 400 nm long junction the penetration
depth is on the order of 1 mm. Since our samples had widths and thick-
nesses less than .001 mm, the critical current was uniform across the
entire cross section of the bridge at all temperatures; i.e., there was
no self-limiting of the critical current, and meaningful comparisons with
the theory were made down to the lowest temperature achievable (0.5K).

4.1.3 Experimental results

Figure 4.3 shows experimental critical current versus reduced
temperature (T_c = 7.26K) data for several samples. (The critical currents
for each sample have been multiplied by the normal-state resistance R_0
for that sample; the determination of R_0 will be considered in the
low-voltage I-V section of this chapter.) The current is plotted on a
logarithmic scale, and it is significant to note that the data for the
shorter samples cannot be fit by a straight line at low temperatures.
This lack of a straight-line fit implies that the critical current at low
temperatures is not proportional to a power of T. (This is not in con-
flict with those theories which predict an exponential behavior since
those theories were done in the clean limit, while our samples are
clearly in the dirty limit.)

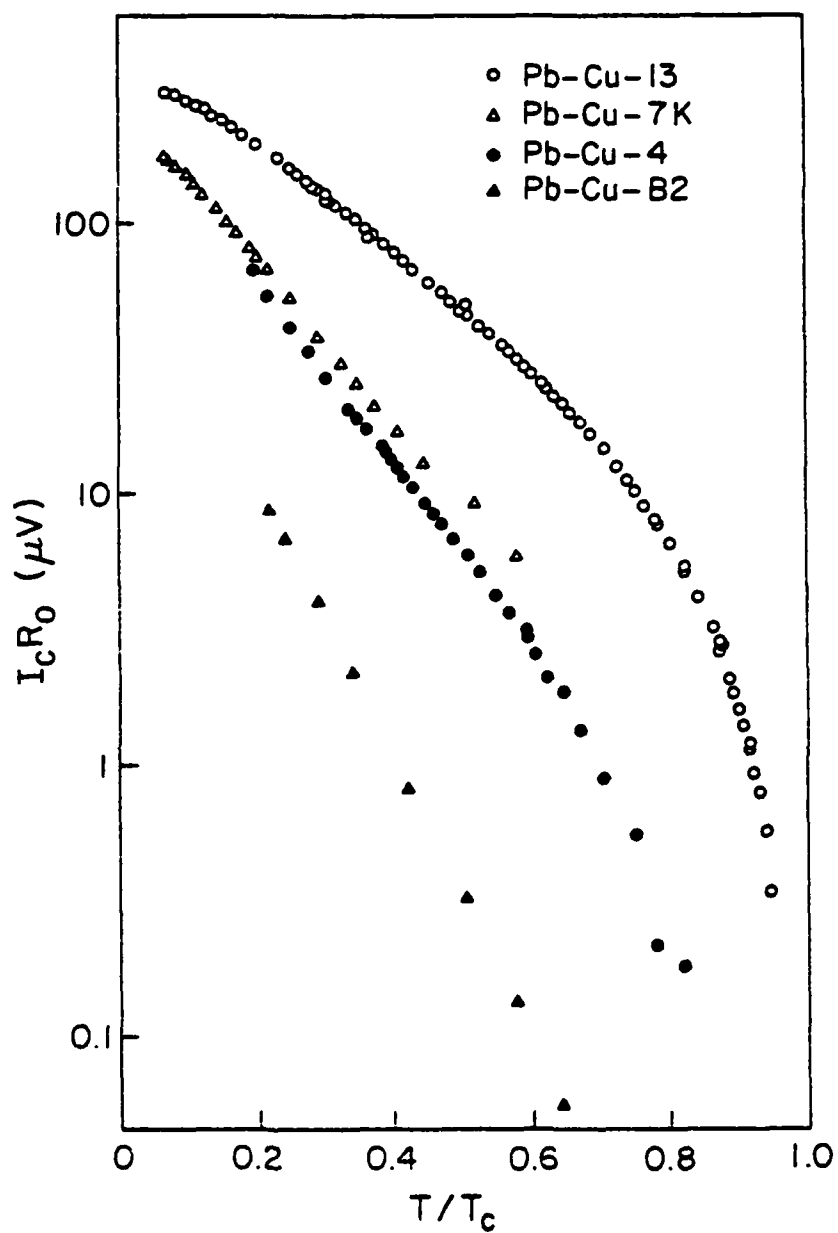Figure 4.4 shows a fit of our Likharev-like[21] calculations to the

Figure 4.3 Experimental data on the temperature dependence of I_cR_o for four Pb-Cu-Pb microbridges (T_c = 7.26 K).
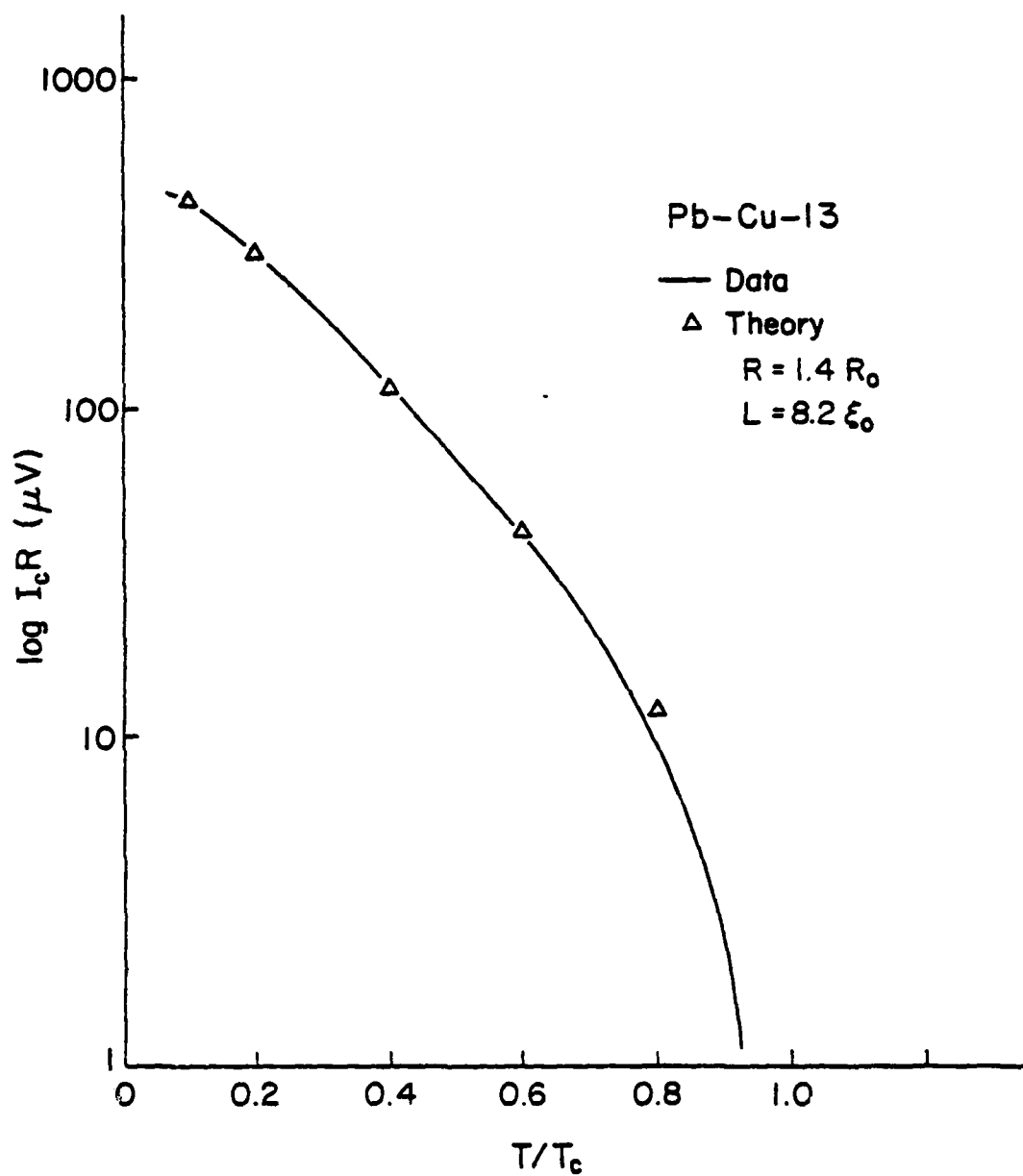
Figure 4.4 Fit of the theoretical I_cR versus T relation for a bridge of reduced length ℓ = 8.2 to the data for Pb-Cu-13. The data has been multiplied by a factor of 1.42.

data for Pb-Cu-13. Because the mean free path Λ and the physical length L were not accurately known for our samples, the reduced length ℓ could not be directly calculated. Instead, ℓ was determined by using it as a fitting parameter in fitting the experimentally determined I_cR versus T curves with the theoretical curves. We found that for the shorter samples it was necessary to increase the resistance slightly in order to fit the shape of the theoretical curves to the experimental data. This can be seen in Figure 4.5. The calculation for $\ell = 8.9$ fits the magnitude of the data best, but the $\ell = 8.2$ fit matches the shape best. There are two possible explanations for our data to have a lower I_cR than predicted. The measured resistance might be too low since the portion of the bridge very close to the banks might not contribute to the measured resistance since the density of pairs is very high there; this effect would be more pronounced in shorter bridges.

The other possible explanation is that since the bridge and the bank have different densities of states, the assumption that $|F|$ is continuous across the interface might be slightly wrong.

We have chosen to adjust the resistance so that the data fits the theory at low temperatures. We have thus taken the ℓ value determined in this way to be the correct reduced length for the bridge. In any case, the different possible ℓ values only differ by less than 10%.

Table 1 gives the reduced lengths and the corrected resistances used to obtain them for some of the samples measured.

The success of this theoretical calculation in fitting the experimental data has two important consequences. First, it provides a good
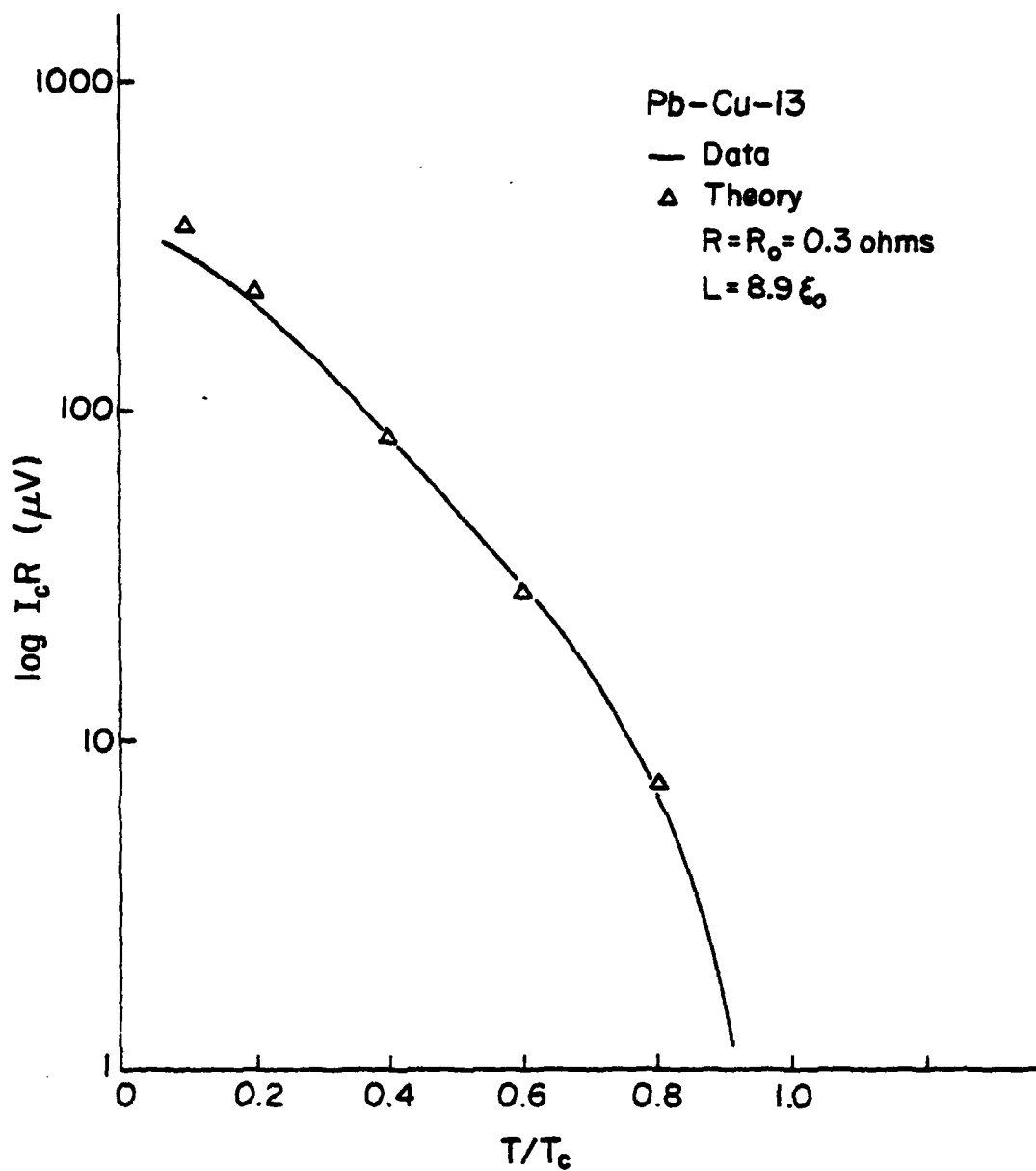
Figure 4.5 Fit of the theoretical $I_c R$ versus T relation for a bridge
of length ℓ = 8.9 to the data of Pb-Cu-13. The data has
not been rescaled.

74

Table 1. Characteristic parameters for Pb-Cu-Pb samples. The values of $V_R(max)$, $I_R R_0(max)$, $I_R(max)$, and Γ_R for Pb-Cu-B2 are only lower bounds since we could not cool this sample to temperatures where these values become constant; a reasonable extrapolation to $T = 0$ gives a value of Γ greater than 4 for this sample.

Sample	R_0 (Ω)	R_f (Ω)	V_{lower} (μV)	V_{upper} (μV)	$V_R(max)$ (μV)	$I_R(max)$ (μA)	$I_R R_0(max)$ (μV)	ℓ	Γ_R
Pb-Cu-13	0.30	0.43	41	200	45	218	65	8.2	5.5
Pb-Cu-7K	0.43	0.55	21	120	25	70	30	11.6	5.1
Pb-Cu-4	0.83	0.83	18	250	21	30	25	12.4	4.8
Pb-Cu-B2	0.075	0.075	5.7	95	8+	104+	7.8+	17.7	3+

test of the validity of Usadel's equations. This appears to be the first experimental verification of these equations. Second, it gives reduced lengths ℓ for the measured samples. Knowledge of these lengths has proven very useful in understanding the low-voltage behavior of these samples.

It can be seen in Figure 4.4 that the Likharev calculation does not fit the data at high temperatures. This is to be expected since this theory ignores the effect of the bridge in reducing the order parameter in the banks, an effect which is non-negligible close to T_c.[7] Close to T_c, however, the theory of deGennes[7] should be valid. Figure 4.6 shows a plot of I_c versus $(1 - T/T_c)^2$ close to T_c for Pb-Cu-13. The data can be fit by a straight line in agreement with the theory of deGennes. Similar plots for the other samples are not possible since the critical currents for those samples were too small to be observed close to T_c of the banks.

4.1.4 Current-phase relation

We have also measured the current-phase relation for these samples. That is, the supercurrent is dependent on the phase difference between the order parameters of the opposing superconducting banks, $I_c = I_0 f(\Delta\phi)$, and we have measured the functional form of f. The details of these measurements has been given by Jackel.[3] We found that for all accessible temperatures $f(\Delta\phi) = \sin\Delta\phi$.

All of the microscopic theories discussed above have predicted that for very short SNS samples the current-phase relation should be non-sinusoidal at low temperatures. But for samples as long as the ones used
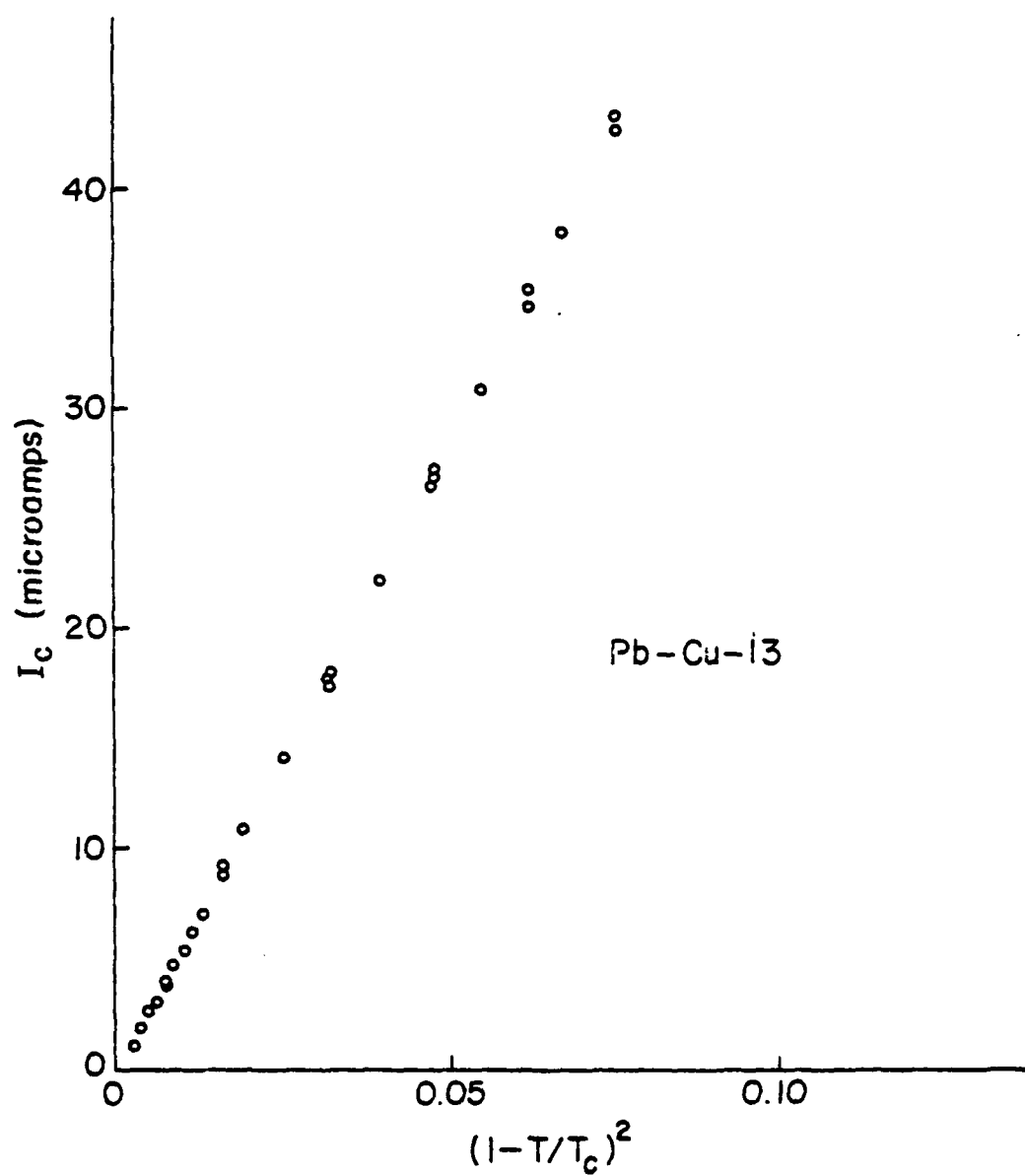
Figure 4.6   Critical current of Pb-Cu-13 plotted versus $(1-T/T_c)^2$ for $T/T_c > 0.9$.

in this work, a sinusoidal current-phase relation has been predicted.
The details of this prediction are given in the Appendix in the discussion
on the integration of Usadel's equations.

4.2 Low Voltage I-V Characteristics

4.2.1 Experimental results

Figures 4.7 through 4.9 show the low-voltage critical current versus
voltage (I-V) curves for some of the samples measured. All of these I-V
characteristics have certain features in common. For almost all tempera-
tures below the transition temperature of the banks there is a critical
current; above this critical current a voltage appears across the sample.
Between two characteristic voltages V_{lower} and V_{upper} the I-V curve is a
straight line. (V_{upper} is not shown in these figures but it is shown in
later figures and its magnitude for various samples is found in Table 1.)
For a given sample the value of the slope of this straight line is inde-
pendent of temperature, except for very close to T_c. (Near T_c the slope
of this line increases with increasing temperature. In Part 4 of this
chapter it will be shown that this increase in slope with temperature is
most likely due to an extra dissipation occurring in the banks.) We
have chosen the low temperature value of this slope to be the normal-
state resistance R_o of the bridge. R_o was the resistance required in
Part 1 to fit the temperature dependence of the critical current to
theory.

The character of the I-V curves above the critical current but
below V_{upper} can be classified by three temperature regimes. At high
temperatures the I-V curve is continuous, rising smoothly from the

Figure 4.7   Low-voltage current versus voltage (I-V) curves
             for Pb-Cu-13.
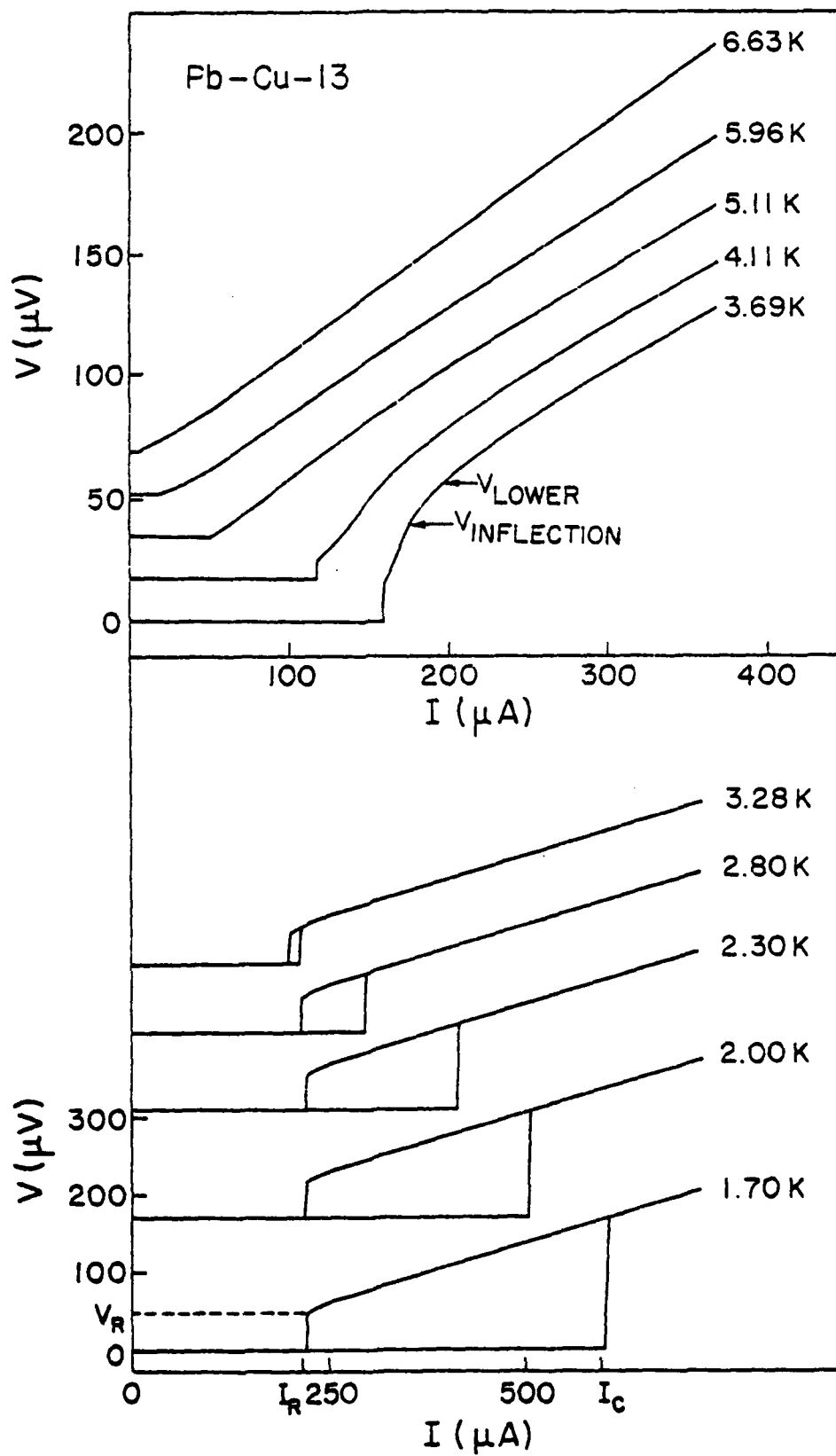
Figure 4.8 Low-voltage I-V curves for Pb-Cu-7.
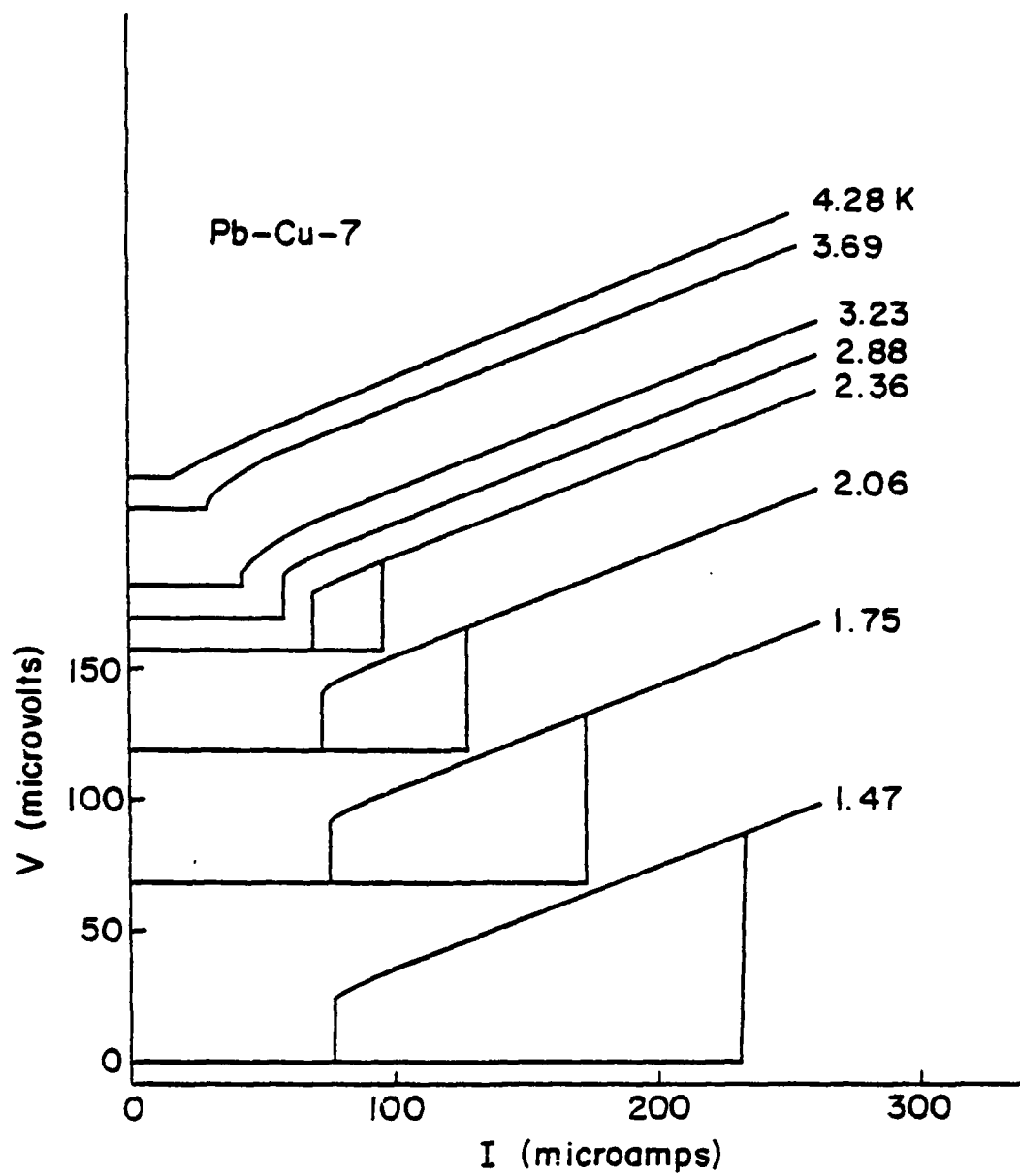
Figure 4.9 More low-voltage I-V curves for Pb-Cu-7.

zero-voltage axis up to the voltage V_{lower} where the curve becomes a straight line. At lower temperatures there is a discontinuous jump in the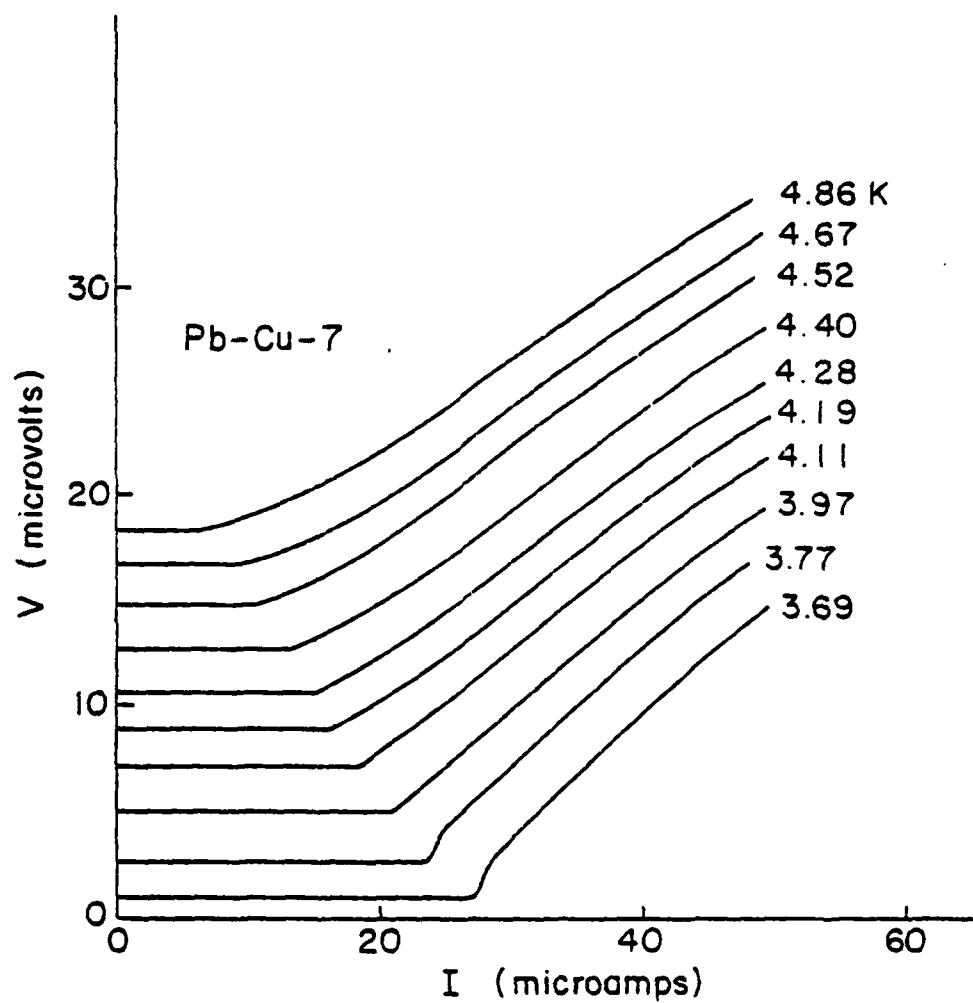 voltage at the critical current, but the curves are still single-valued. At still lower temperatures the curve becomes hysteretic; i.e., if the current is increased from zero the voltage jumps to a finite value at the critical current I_c, but if the current is slowly decreased from above I_c the voltage does not return to the zero-voltage axis until a lower current I_R is reached. Each of these temperature regimes will be discussed in detail.

Single-valued, continuous regime

In this regime the I-V curve rises from the zero-voltage axis with an initially upward curvature; at the inflection point $V_{inflection}$ the curvature changes sign; when the voltage V_{lower} is reached the I-V curve becomes a straight line. The temperature dependence of these voltages $V_{inflection}$ and V_{lower}, as well as the temperature dependence of the currents $I_{inflection}$ and I_{lower} at which these voltages occur, are shown in Figures 4.10 and 4.11. It was found that within the accuracy of the data the voltages $V_{inflection}$ and V_{lower} are independent of temperature. On the other hand, the corresponding currents $I_{inflection}$ and I_{lower} seem to be decreasing with increasing temperature. (See the Measurement Techniques chapter for a discussion on the measurement of V_{lower} and $V_{inflection}$.) Note that if the currents $I_{inflection}$ and I_{lower} are multiplied by the temperature-dependent (near T_c) low-voltage resistance (Figure 4.35) the resulting voltages are still decreasing with increasing temperature.
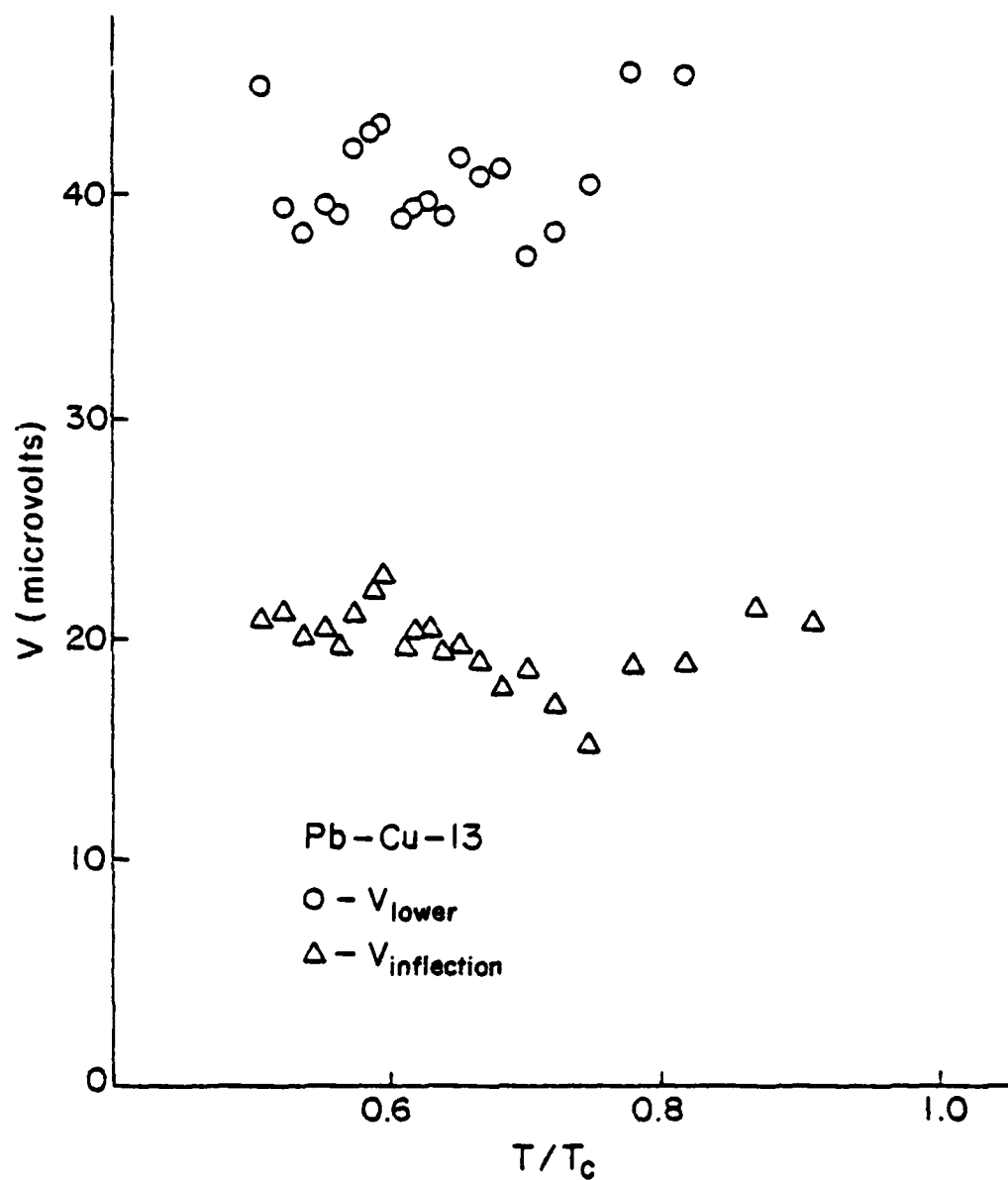
Figure 4.10 Temperature dependence of the characteristic voltages
V_{lower} and $V_{inflection}$ for Pb-Cu-13.
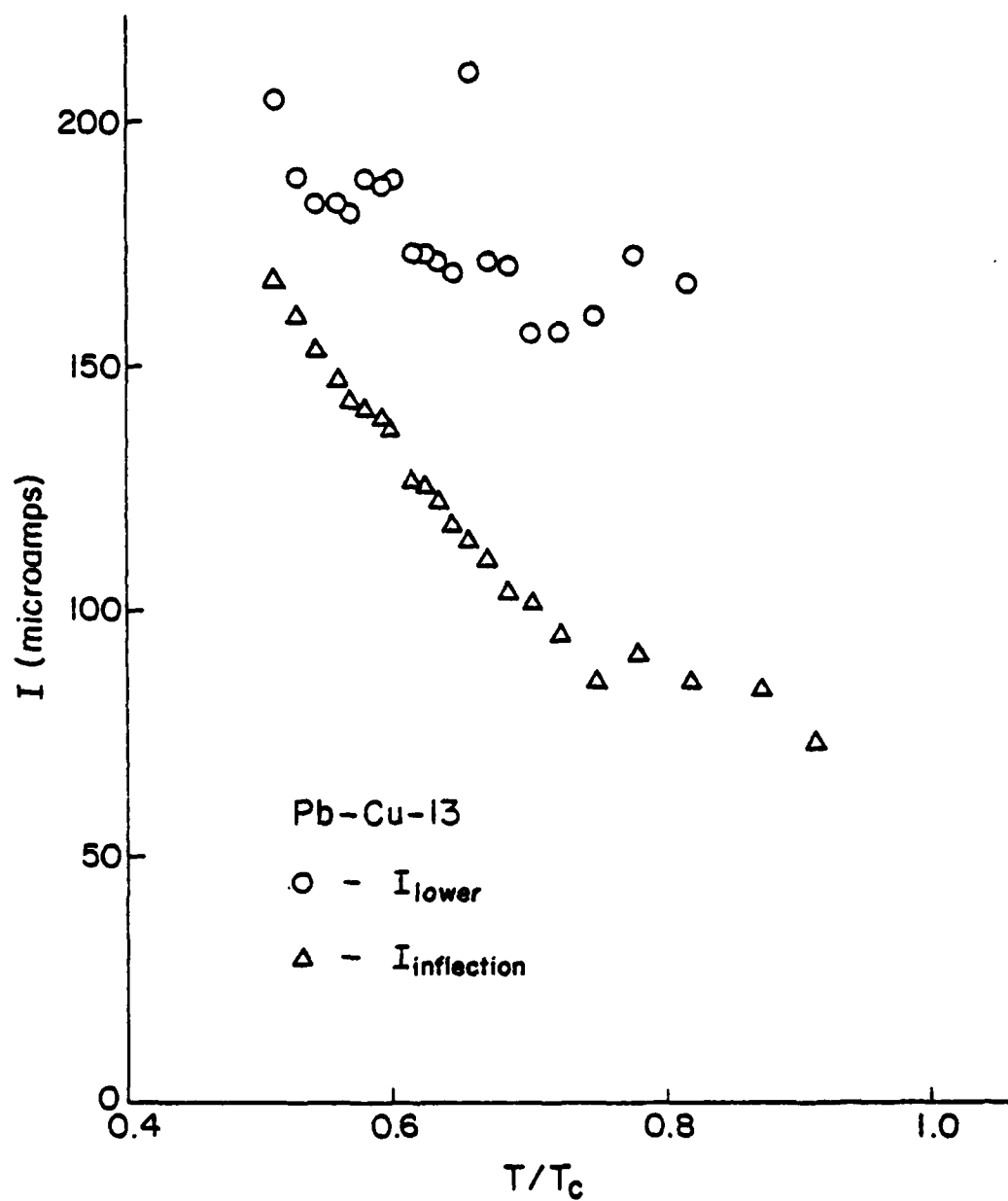
Figure 4.11   Temperature dependence of I_{lower} and $I_{inflection}$ for Pb-Cu-13.

Single-valued, discontinuous regime

At intermediate temperatures the I-V curve leaves the zero-voltage axis discontinuously, jumping up to a continuous curve whose shape is very much like the shape of the I-V curve in the continuous regime. At the high-temperature end of this regime the I-V curve has an inflection point at the same voltage as in the continuous regime. As the temperature is lowered, the magnitude of the voltage jump increases; at the low-temperature end of this regime this magnitude has increased beyond $V_{inflection}$ and the curve no longer has an inflection point. Just before the magnitude of the jump reaches V_{lower} the I-V curve becomes hysteretic.

Hysteretic regime

At low temperatures the I-V curve is hysteretic; this hysteresis can be characterized by a return voltage V_R and a return current I_R. Figures 4.12 and 4.13 show the temperature dependence of I_R and V_R. It was found that at low temperatures both I_R and V_R become independent of temperature. It can be seen in Table 1 that the low-temperature limit of V_R is very nearly equal to V_{lower} for the samples studied. It was also found that after I_R and V_R cease to depend on temperature the only change with temperature of the I-V curve was the critical current—the finite-voltage portions of the I-V curve do not change with temperature. Note that while the low-voltage resistance is temperature independent below about 0.7 T/T_c (Figure 4.35), the I-V curve becomes temperature independent only below about 0.5 T/T_c.

The temperature at which the return voltage and the return current become constant is related to the sample length; i.e., longer samples
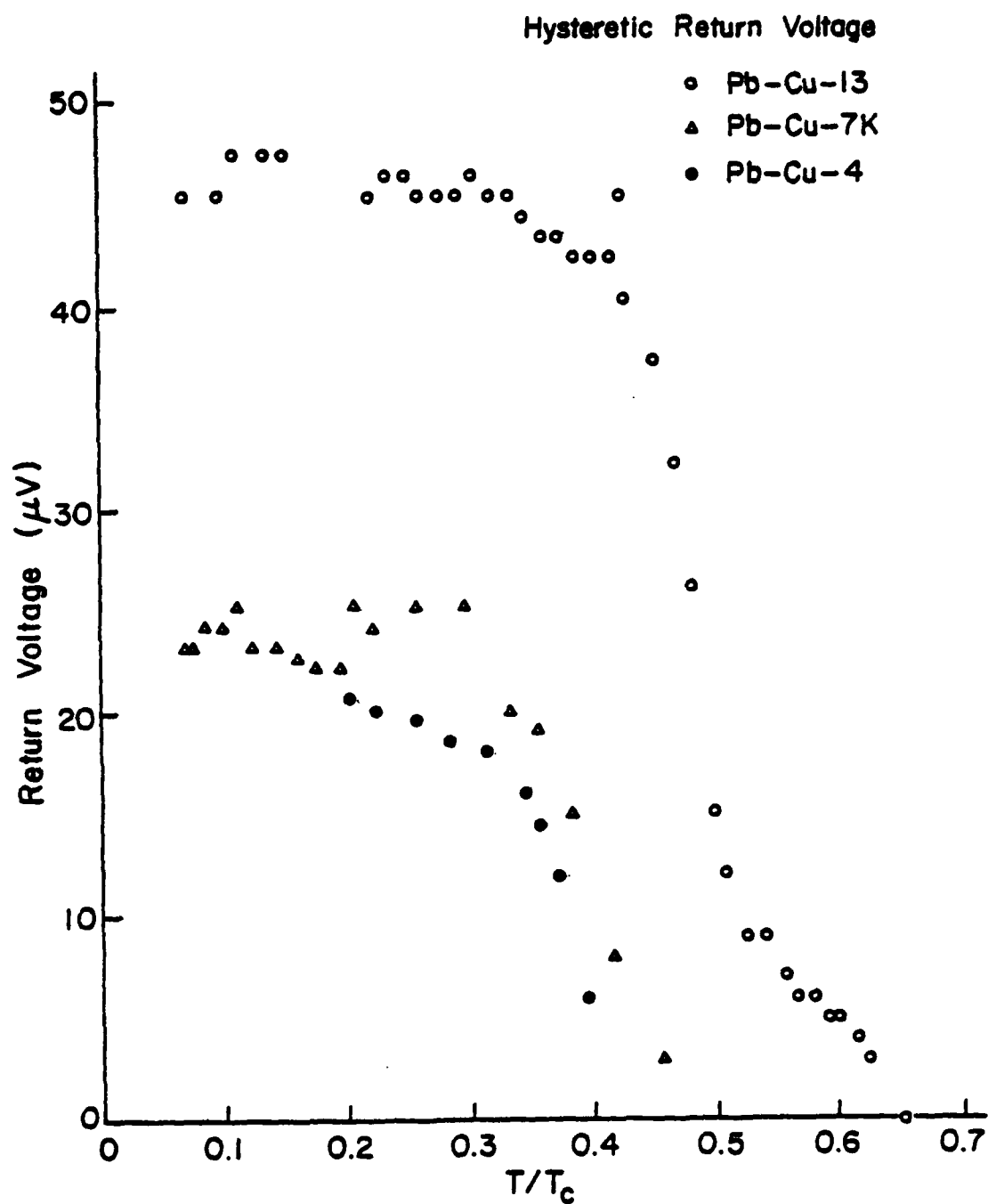
Figure 4.12 Temperature dependence of the return voltage V_R for three Pb-Cu-Pb samples.
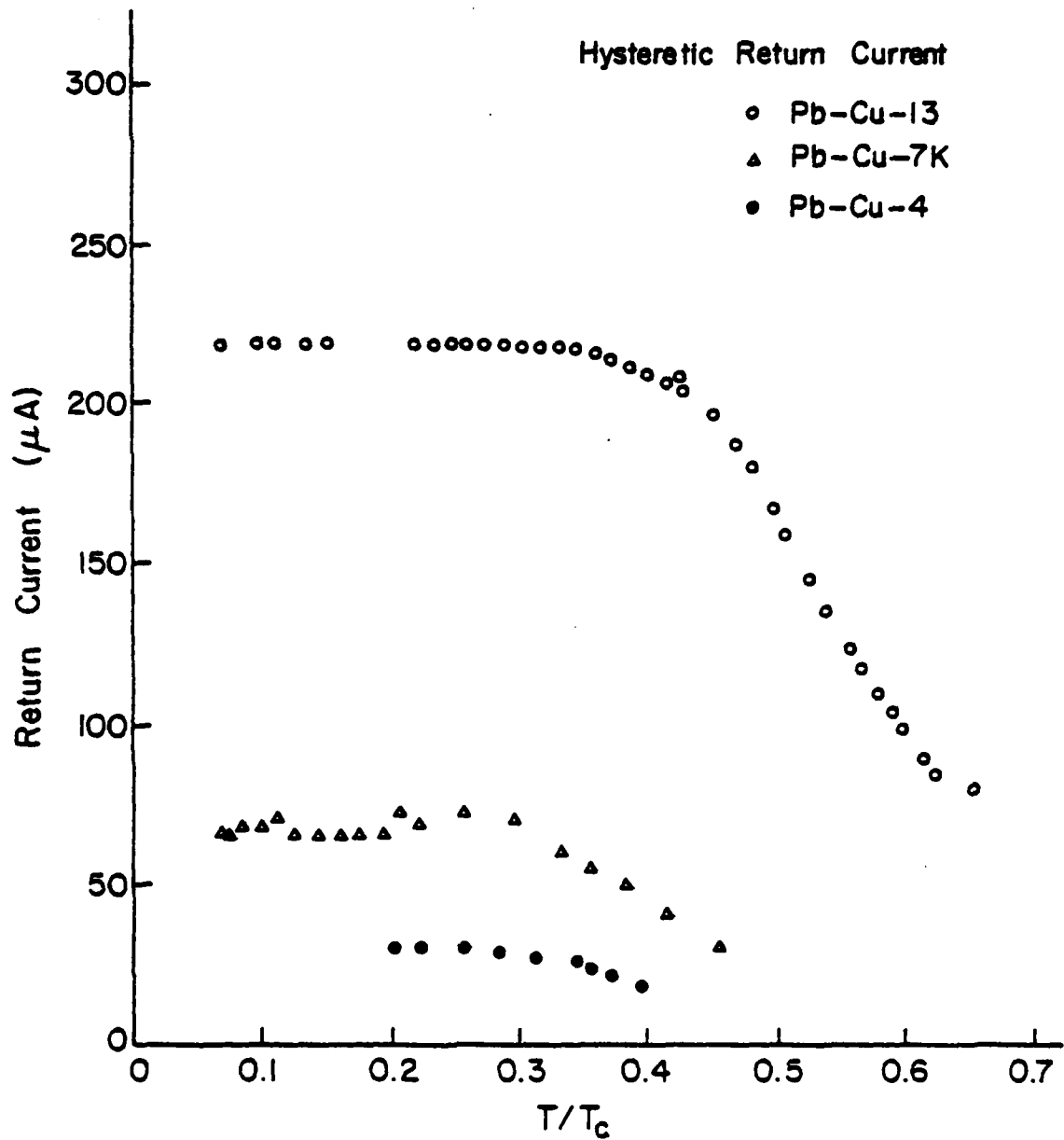
Figure 4.13   Temperature dependence of the return current I_R for the samples as in Figure 4.12.

reach this stage at lower temperatures. In fact, for some of the longer samples we could not lower the temperature low enough for this return voltage to become constant, although the trend in this voltage indicated that it would become constant. For very long samples no hysteresis was observed in solely dc measurements, but hysteresis could be induced in these very long samples by irradiation with microwaves.

4.2.2 Theoretical considerations

Hysteresis

The hysteresis found in these SNS samples is unusual in that all of the other popular types of superconducting weak links (oxide tunnel junctions, point contacts, and microbridges with superconducting bridges) do not exhibit temperature-independent return currents at temperatures where the critical current is not also temperature independent. Thus the unusual nature of the observed hysteresis is due to the fact that the bridge is made from a normal metal.

There have been three sets of theories advanced as explanations for hysteresis in superconducting weak links. The first theory proposed was that the capacitance between the electrodes was the cause of the hysteresis.[25,26] This explanation can be ruled out for two reasons: the planar geometry of our samples has far too little capacitance to cause any hysteresis, and these capacitance theories require a change in the return current if the critical current changes.

The second possible possible explanation is the joule heating theory of Skocpol et al.[27] This theory is also unable to account for the observed temperature dependence of I_R, since this theory requires I_R to

be proportional to $(1 - T/T_c)^{\frac{1}{2}}$; our samples have an I_R which is independent of temperature at low temperatures. In addition, it will be shown later that the response of these microbridges to microwave radiation precludes the existence of sufficient joule heating to cause hysteresis.

The third possibility, and the one which seems to be applicable to our samples, is that the hysteresis is a result of an intrinsic relaxation time. This relaxation-time explanation was first proposed by Song[28], and it has been put on a stronger theoretical footing by other authors.[29,30] These theories are set in a time-dependent Ginzburg-Landau framework, and this framework allows some qualitative comparisons to be made.

Time-dependent Ginzburg-Landau relaxation time

The time-dependent Ginzburg-Landau (TDGL) theory contains an intrinsic relaxation time which is valid for superconductors above T_c; we can use this time by considering a normal metal to be a superconductor with a T_c of 0 K. This TDGL relaxation time is given by[31]

$$\tau_{GL} = \frac{\pi\hbar}{8k(T - T_{c-bridge})} = \frac{\pi\hbar}{8kT}$$

where we have used $T_{c-bridge} = 0$. If the spatial-gradient terms of the TDGL equations are taken into account, the effective relaxation time for a microbridge of length L is given by

$$\tau_{eff} = \ell^2 \tau_{GL} = \left(\frac{L}{\xi(T)}\right)^2 \tau_{GL} = \frac{\ell^2 \pi\hbar}{8k\, T_{c-banks}} = \frac{\pi^2 L^2}{4D} \quad ; \quad D = \frac{v_f \Lambda}{3}$$

This time is essentially the time required for electron pairs to diffuse through the normal-metal bridge. It is also the time for any electron to diffuse through the normal metal. This diffusion process is the reason

why the effective time is proportional to the square of the length of the bridge.

There are two important features of this relaxation time which are easily accessible to experimental measurement. The first is that τ_{eff} is independent of temperature, and the second is the dependence of τ_{eff} on ℓ.

Baratoff and Kramer (BK)[29] have numerically solved the TDGL equations for the case of a weak link whose bridge is a gapless superconductor with reduced length $\ell = 1$. They found that the I-V characteristics could be classified by a quantity Γ:

$$\Gamma = \tau_{eff}/\tau_J \quad \text{where} \quad \tau_J = \frac{\hbar}{2eI_cR_0} .$$

For our samples τ_{eff} is a constant, independent of temperature; thus Γ is inversely proportional to I_c for our samples.

BK have shown that the relaxation time affects the shape of the I-V curve in two ways. First, when the microbridge is in a finite-voltage state the magnitude of the oscillating supercurrent, $|I_s|$, is reduced below the zero-voltage value I_c. For a constant temperature (corresponding to a fixed Γ and a fixed I_c) $|I_s|/I_c$ becomes smaller as V_{dc} is increased. This decrease in I_s as I is increased produces an I-V curve which becomes a straight line at a smaller value of I/I_c than the value predicted by the shunted junction model. In fact, BK have shown that above the voltage V_{lower} (the dc voltage at which the I-V curve becomes a straight line), the oscillating supercurrent is almost completely suppressed.

BK predicted that if Γ increases, V_{lower}/I_cR_0 should decrease. We

find this to be the case in our samples, except perhaps close to T_c. As the temperature is lowered, and Γ increases since Γ is inversely proportional to I_c in our samples, we find that V_{lower} is constant. (That is, in effect, a decrease in $V_{lower}/I_c R_o$ since I_c increases with decreasing temperature.) This temperature independence of V_{lower} can be seen in Figure 4.14 and in Figures 4.7 through 4.9.

The second relaxation effect found by BK is that for $\Gamma > 38$ the I-V curve should be hysteretic; this hysteresis is observed in our samples. We have defined a quantity Γ_R by the value of Γ at which our samples have just fully developed hysteresis; i.e., $\Gamma_R = (2e/\hbar)I_R R_o \tau_{eff}$. Values of Γ_R for different samples are shown in Table 1; although there is considerable variation in ℓ and $I_c R_o$, Γ_R is found to be very weakly dependent on length, showing a slight tendency to increase as ℓ decreases. As was found for V_{lower}, it has been observed that at low temperatures the voltage V_R at which the I-V returns to the zero-voltage axis is independent of temperature. We have found that V_{lower} and V_R have nearly the same low temperature values.

In summary, we have found that for dc voltages across the sample greater than about $5 \hbar/2e\tau_{eff}$, the I-V curve is almost independent of temperature. Considering the theoretical work of BK, we have concluded that as the dc voltage exceeds $\hbar/2e\tau_{eff}$ the magnitude of the oscillating supercurrent begins to decrease; when $V_{dc} > 5\hbar/2e\tau_{eff}$, the oscillating supercurrent is almost completely suppressed. Further, the temperature independence of τ_{eff} is confirmed by the temperature independence of V_R and V_{lower}, and τ_{eff} is found to scale nearly as ℓ^2.
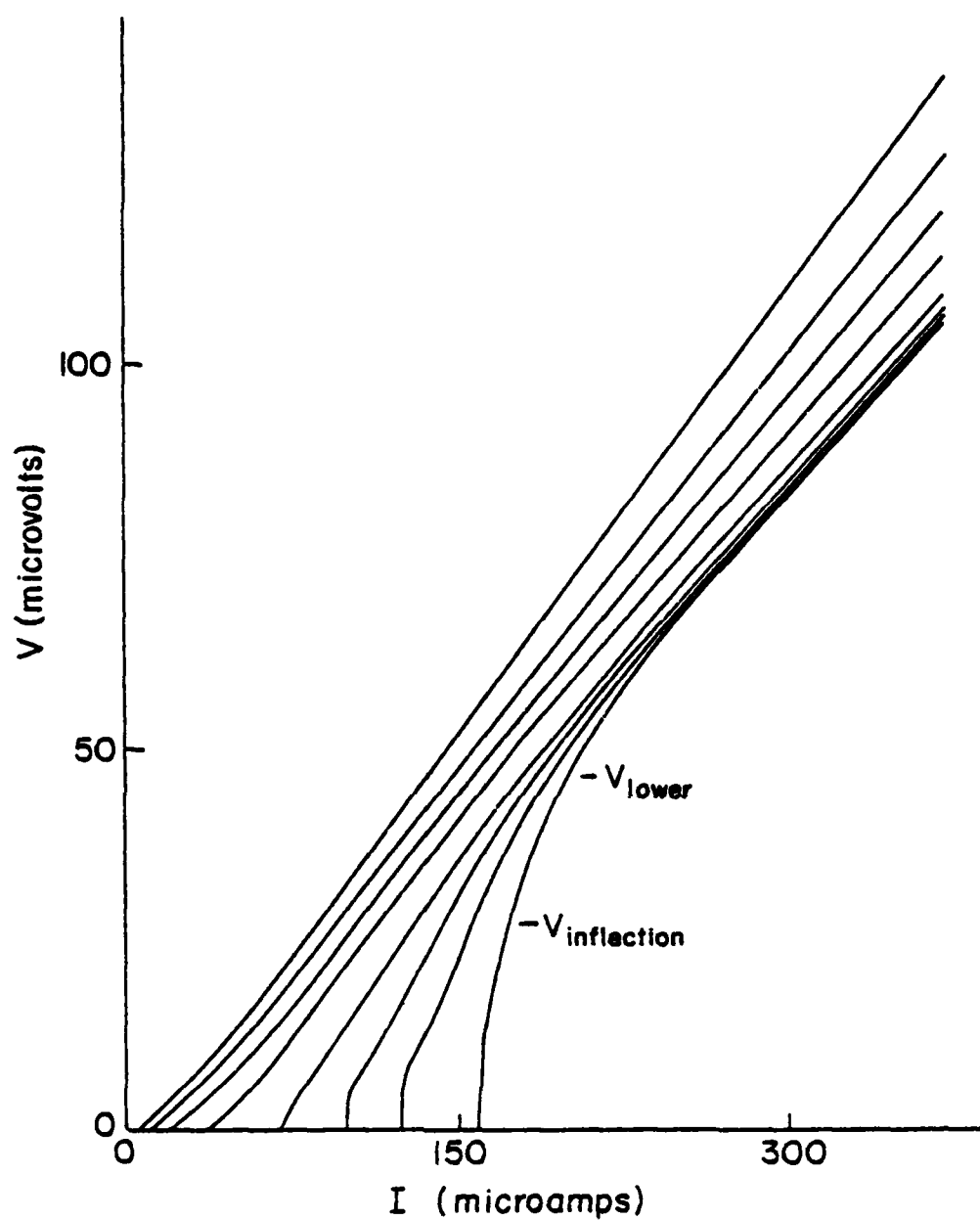
Figure 4.14   I-V curves for Pb-Cu-13.   In this figure the curves for
different temperatures are not offset in voltage as they
are in previous figures.   The curves were taken at
temperatures 6.63, 6.34, 5.96, 5.44, 4.76, 4.34, 4.04, and
3.69 K.

Our experimental findings on hysteresis are not in complete agreement
with the theory of BK, since they predicted an onset of hysteresis at
$\Gamma = 38$, while our result is that hysteresis beings at $\Gamma \simeq 2$.

The conclusion that above V_{lower} the supercurrent is almost completely
suppressed does not mean that for dc voltages above V_{lower} the bridge can
always be treated simply as a normal metal. It will be shown in the next
part of this chapter that microwave radiation can cause a supercurrent to
be re-established.

The theories of BK and others[32] also do not describe the straight-
line portion of the I-V completely satisfactorily since they do not
predict the observed behavior of the "excess current". This "excess
current" is seen in Figures 4.7 through 4.9 by the fact that the straight-
line portion does not pass through the origin; this portion of the I-V
is offset in current by an "excess current". These TDGL theories contain
an "excess current" which depends on I_c, while at low temperatures our
samples have an "excess current" which is independent of I_c.

Although the BK theory does not agree with all of our experimental
findings, the BK calculations did not use exactly the same model condi-
tions as are present in our samples; numerical calculations specific to
long SNS microbridges are needed to see if the TDGL equations are capable
of quantitatively predicting the observed hysteresis and "excess current".

Theories of the low-voltage curvature of the I-V

The TDGL theories have a severe problem in that they do not predict
the increase in I_c with microwave radiation (to be discussed in the next
part of this chapter). Secondly, they do not predict the inflection point

seen in the I-V at high temperatures. Theories have been recently advanced to explain this initial upward curvature of the I-V.[33,34] These theories are related to the TDGL theories, but they include the effect of non-equilibrium electrons in changing the magnitude of the gap in the density of states in the bridge region. The net prediction of these theories is that for I just above I_c the gap and hence the oscillating supercurrent increases with I, thus giving rise to an upward curvature. But because our SNS microbridges cannot have a gap in the bridge, these theories are not immediately applicable to our samples. It is possible that a similar effect could be found in the correlation picture of superconductivity which is applicable to SNS structures. The relaxation time τ_{eff} used above is a time which governs the ability of the correlation function F to respond to temporal changes in the current, and the temperature independence of this time may be the cause of the temperature independence of the inflection voltage $V_{inflection}$. This enhanced-correlation explanation will be discussed in more detail in the next part of this chapter, where the increase in I_c by microwave radiation will be considered.

4.2.3 Previous experimental work

There have been only three other measurements of the low-voltage I-V characteristics of SNS junctions. Clarke[35] measured his junctions up to only about 20 nV. He did not observe any hysteresis. His smaller junctions had I-V's which could be fit by the shunted-junction model, while his larger junctions had features characteristic of flux-flow. The other two sets of authors[24,36] did not describe their I-V measurements in detail, and no hysteresis or unusual curvature was noted.

4.3 Effects of Applied Microwave Radiation

The previous two parts of this chapter were concerned with the I-V characteristics produced when the sample was driven by only a dc current. In this part we will consider the I-V curve generated when the sample was driven by an ac current as well as a dc current; ac frequencies between 1 GHz and 26 GHz were used. The most important result is that the features of the I-V curves can be classified by whether or not the applied rf period was above or below a critical period. It has been empirically observed that this critical period was determined by the Josephson period or the Ginzburg-Landau relaxation time, whichever was longer.

There were two basic changes in the I-V curve when an ac current was applied. First, the critical current increased, an effect which is popularly known as the Wyatt-Dayem effect. Second, constant-voltage steps appeared on the I-V curves, an effect known as the ac Josephson effect. Both of these effects can be seen in Figure 4.15. Although these two effects are not entirely unrelated, they will be presented separately.

4.3.1 Previous experimental work on microwave-enhanced critical currents

The first observations of a microwave-enhanced critical current were made by Wyatt et al.[37] and by Dayem and Wiegand.[38] They used samples of the uniform-thickness constriction type and observed an enhancement only very close to T_c. Gregers-Hansen et al.[39] found a similar behavior in scribed tin and indium bridges, with enhancements only seen close to T_c. Fjordbøge et al.[40] observed an enhancement in

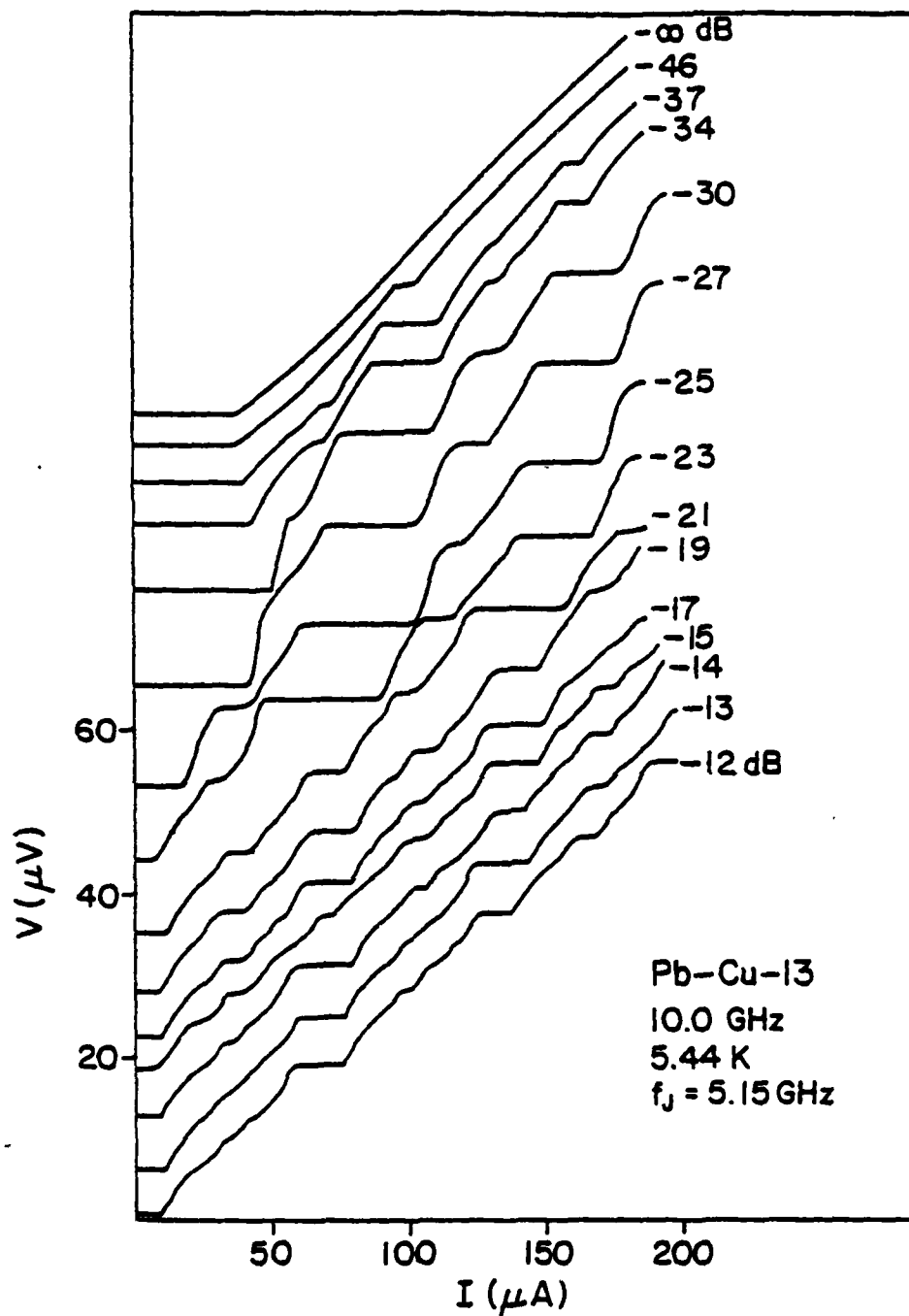Figure 4.15   I-V curves for Pb-Cu-13 with 10.0 GHz applied microwave
radiation.   T = 5.44 K and ω_{rf}/ω_J = 1.94.

aluminum point contacts; they also found the enhancement to occur most strongly very close to T_c.

Notarys et al.[41-43] conducted a study of the dependence of the critical-current enhancement on the length of the bridge. They used samples in which the weak region was obtained by underlying a section of a strip of superconductor with a lower T_c material (gold under tin or titanium under tantalum) or by ion-implanting a section of the super-conducting strip (copper or iron into tantalum). They found large enhance-ments in the tin-gold samples, with the largest enhancements occurring in the shortest samples. The tantalum-based samples had smaller enhance-ments than the tin-gold samples, with the longer tantalum-based samples having larger enhancements than similar shorter tantalum-based samples. (The tantalum-based samples had much longer reduced lengths than the tin-gold samples.) For all of their samples the critical current was enhanced only at temperatures within about 0.2 of T/T_c.

Latyshev and Nad[44] conducted a thorough study of the frequency dependence of the enhancement in variable-thickness tin bridges. They found a lower frequency limit which was essentially independent of temperature. They also found an upper limit for the frequency; if the frequency of the applied microwaves was higher than the gap frequency, they found no enhancement.

It will be shown below that the results of all of these previous experiments differ significantly from our results.

4.3.2 Microwave-enhanced critical current, experimental results

Figures 4.16 through 4.19 show the temperature dependence of the critical current I_c when a microwave field was applied for several samples.
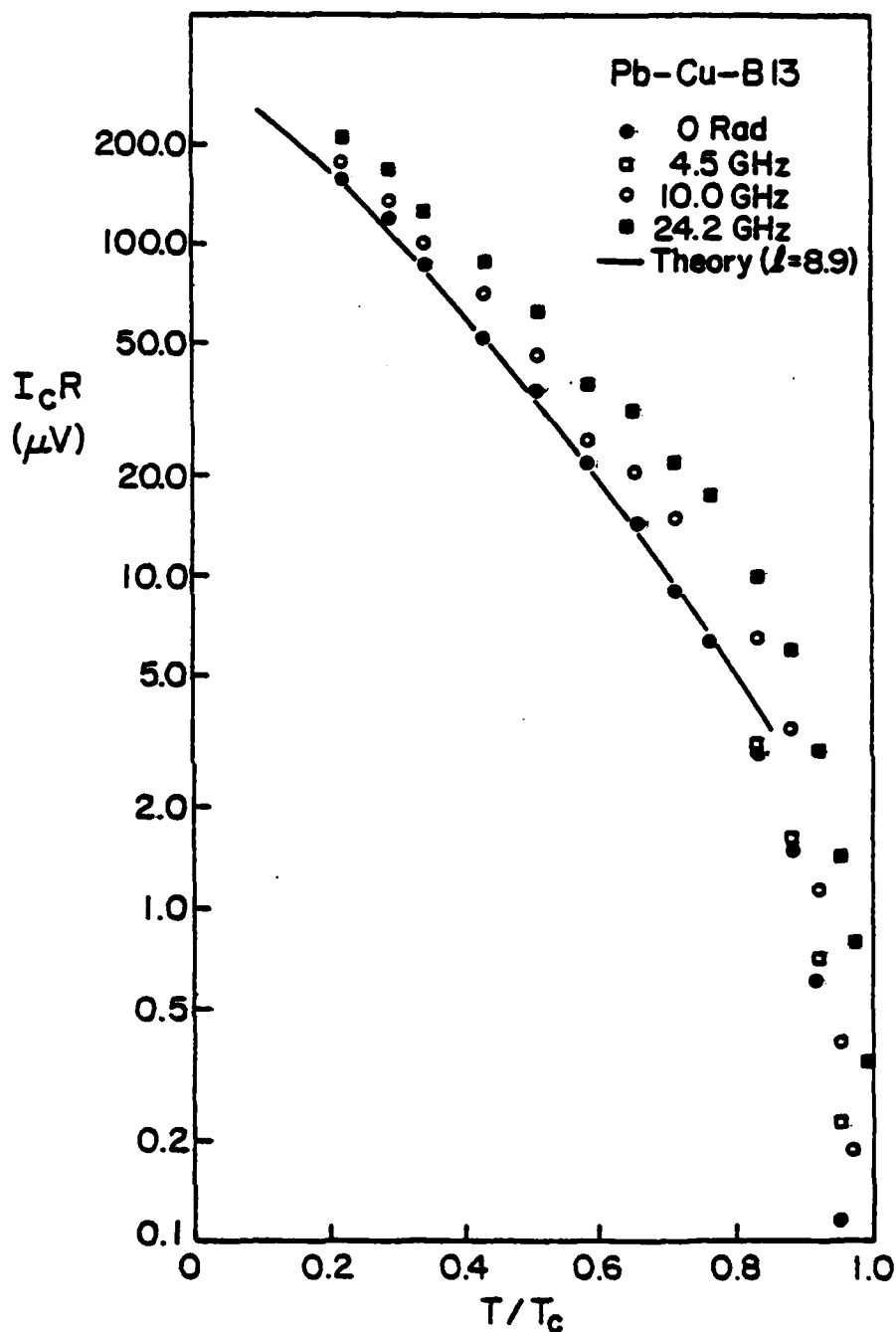
Figure 4.16 I_cR_0 versus T/T_c for Pb-Cu-13 with three different frequencies of applied microwave radiation. In each case the data were taken at the constant rf power level which maximized I_cR_0 at low T. The solid line is the theoretically calculated value for $\ell = 8.9$, but with magnitude reduced by a factor of 0.7.
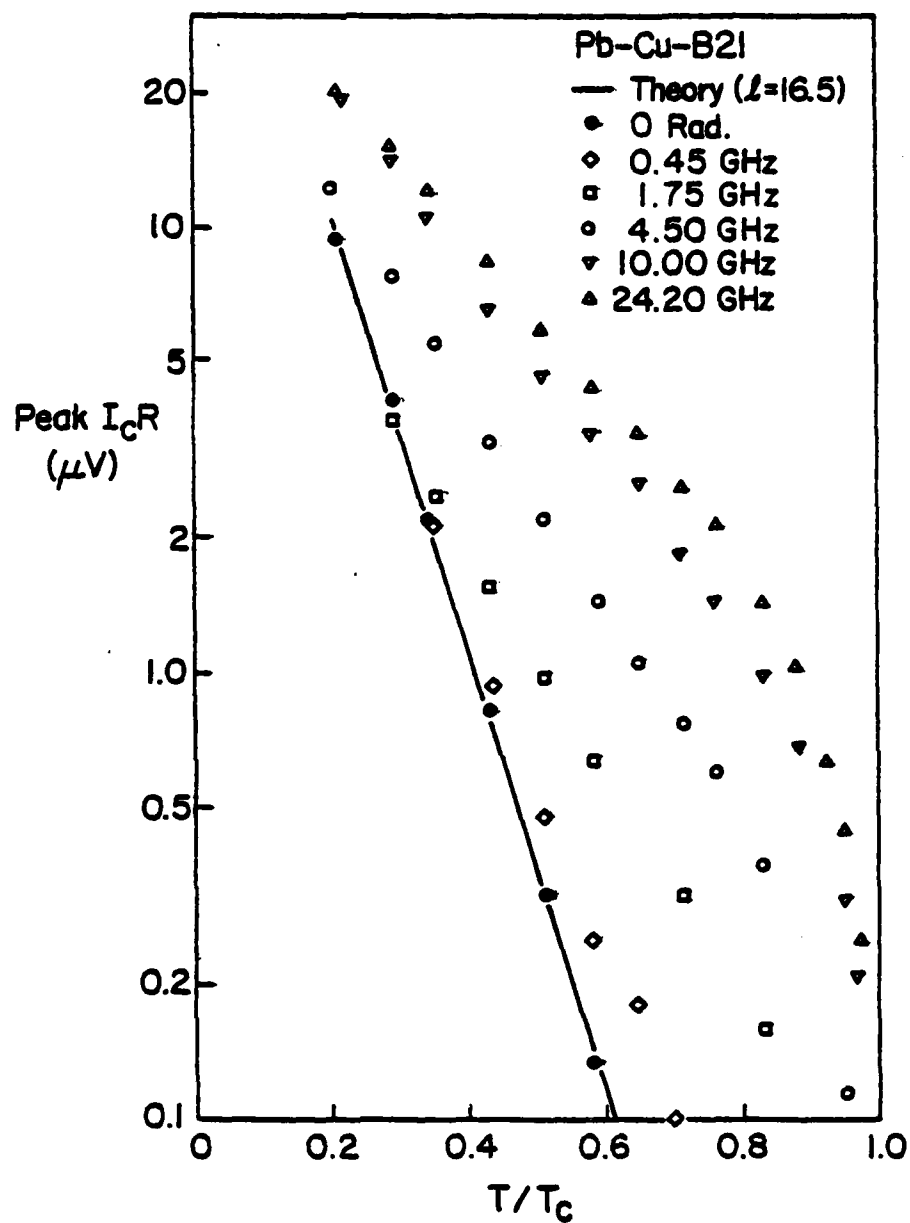
Figure 4.17 I_cR_0 versus T/T_c for Pb-Cu-B2 with five different fre-
quencies of applied microwave radiation. For each
frequency the rf power level was held constant. The
solid line is the theoretical prediction, reduced by a
factor of 0.7, for $\ell = 16.5$.
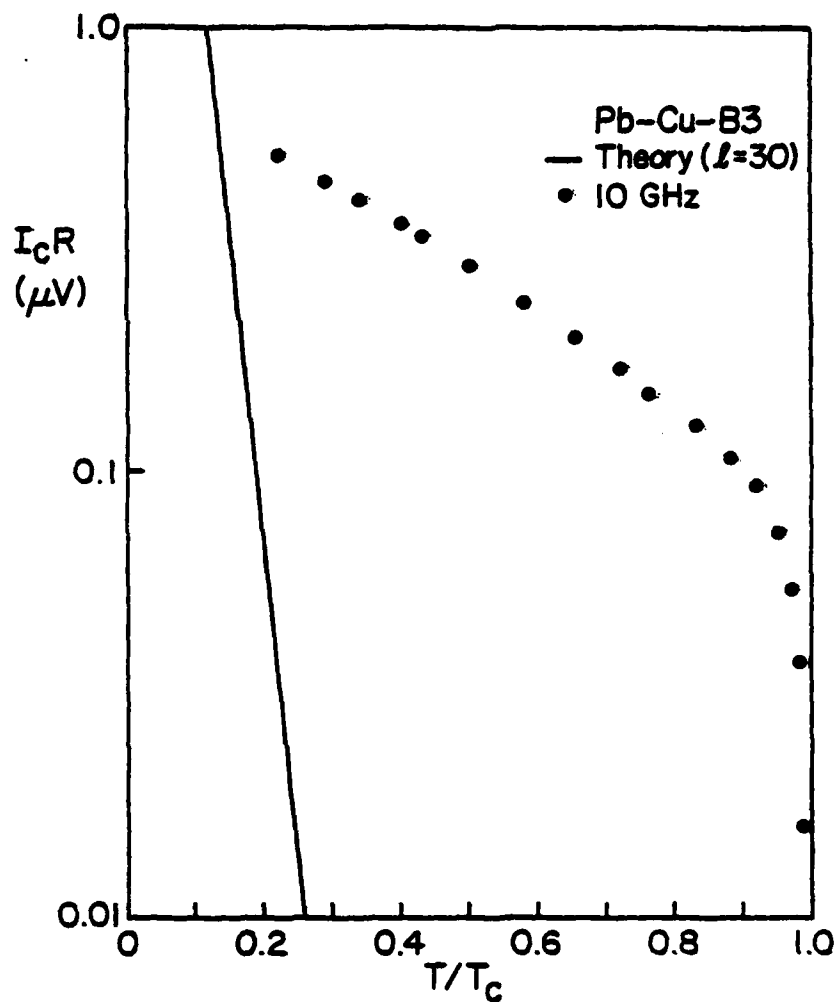
Figure 4.18 I_cR_0 versus T/T_c for Pb-Cu-B3 with 10 GHz radiation; the data was taken at a constant rf power level. The solid line is the calculation for $\ell = 30$ which is the estimated value for this junction. No critical current could be observed in the absence of microwaves.
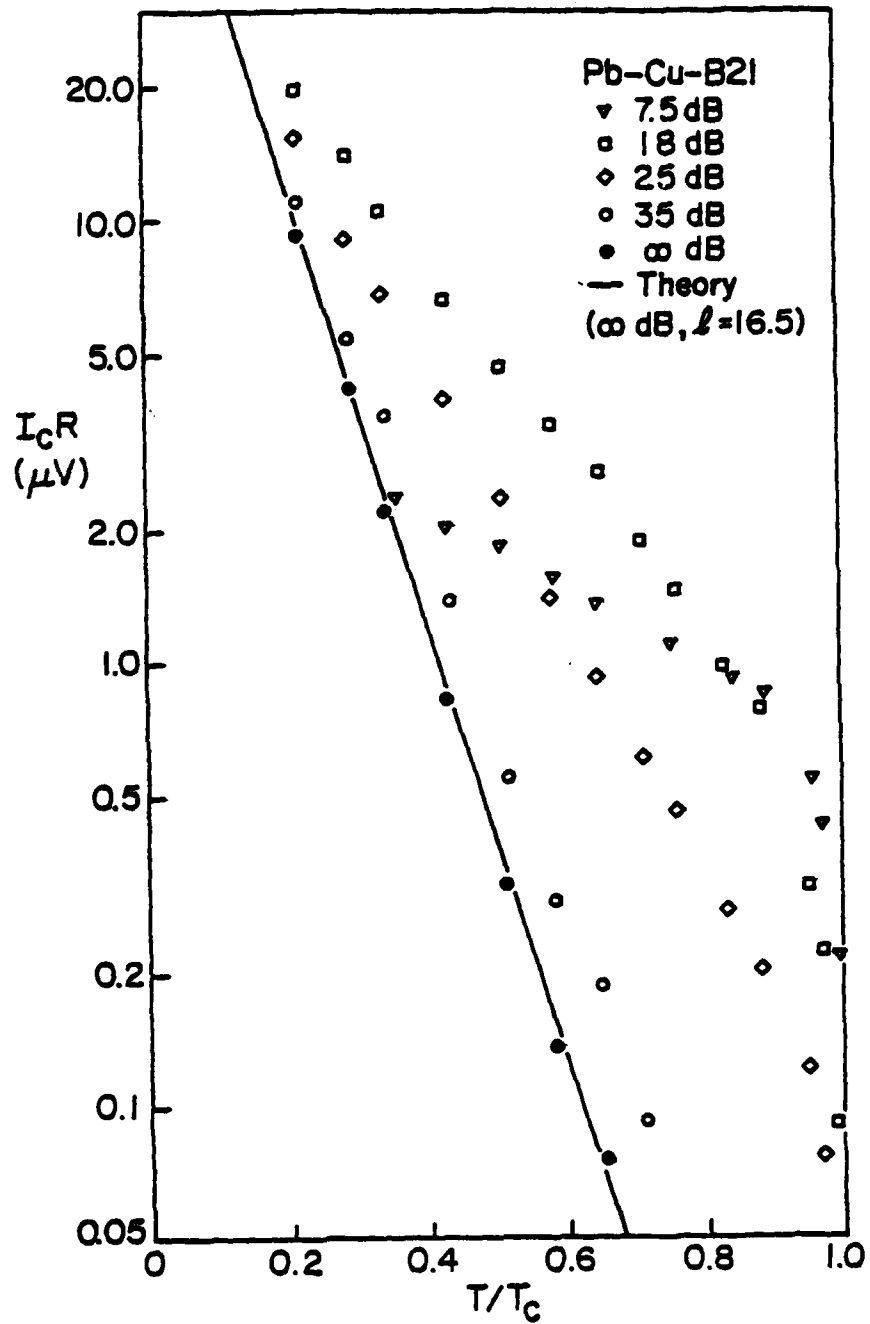
Figure 4.19 I_cR_0 versus T/T_c for Pb-Cu-B2 with 10 GHz radiation of different power levels. 18 dB is the power level that produced the first maximum in I_cR_0; 7.5 dB produced the second maximum.

It can be seen that the relative enhancement I_c/I_0 (I_0 is the critical current in the absence of microwave radiation) depended on the temperature, the frequency, and the length of the bridge. We have found that there was a minimum frequency necessary to observed an enhanced I_c. Two empirical criteria have been established for this minimum frequency; it was necessary to satisfy only one of the criteria to observe an enhancement.

The first criterion was that ω_{rf} had to be greater than the Josephson frequency $\omega_J = 2eI_c R_0/\hbar$. For a given microwave frequency this determined a temperature above which an enhancement could be seen, provided that the enhanced I_c was large enough to be observed above the noise.

The second criterion was that $\omega_{rf} > A/\tau_{eff}$ ($A \sim 2$), where τ_{eff} is the effective time-dependent Ginzburg-Landau relaxation time discussed in detail in the second part of this chapter. It is important to note that τ_{eff} is independent of temperature; thus when ω_{rf} was significantly greater than A/τ_{eff}, I_c enhancement would occur at all temperatures regardless of whether or not $\omega_{rf} > \omega_J$. Since τ_{eff} is proportional to ℓ^2 (ℓ is the reduced length of the bridge), this second criterion was satisfied for longer bridges at lower frequencies. It can also be observed that as ω_{rf} became much greater than ω_J, or as ω_{rf} became much greater than A/τ_{eff}, the relative enhancement became much greater, becoming as much as two orders of magnitude for the longest bridges studied.

Figure 4.19 illustrates the effect that different power levels of a constant microwave frequency had on the critical current. It can be seen that the effect of the microwave field can be interpreted as having

changed the temperature dependence of I_cR. As the power was increased, the I_cR versus T curves took on shapes appropriate for smaller values of ℓ. This slope-changing effect can also be seen in Figures 4.16 and 4.17. The longer the ℓ, or the higher the frequency, the more pronounced the change. However, while the microwave radiation radically changed the slope of the I_cR curves, the low-temperature values of I_cR remained at low levels. At no time did we observe an enhanced I_cR larger than the T=0 value predicted for a given junction by the Usadel equations.

Our experimental results are quite different from those of previous workers. We find that the critical current can be enhanced at all temperatures below the transition temperature of the banks, provided that the applied microwaves have a high enough frequency. This disagreement is probably due to the fact that our samples had bridges composed of a material which is not superconducting at any temperature, whereas the previous workers had bridges which were superconducting at relatively high temperatures.

4.3.3 Theoretical considerations on microwave-enhanced critical currents

There have been two different theories advanced to explain the microwave-enhancement of the supercurrent in superconducting microbridges. Both of these theories are based on the effect that non-paired electrons (quasiparticles) have on the density of paired electrons. The first theory was originally advanced by Eliashberg[45] and was further developed by Chang and Scalapino.[46] This theory suggests that the microwaves change the quasiparticle distribution by increasing the average energy of the quasiparticles; this change results in an increase in the

superconducting energy gap. Since the number of quasiparticles is highest near T_c, the gap is increased most near T_c. It seems that this mechanism should not apply to our samples, since there is no gap in the normal metal bridge. An increase in the gap of the banks could be induced, but since I_c depends at most on $(\Delta_{banks})^2$, the gap in the banks would have to be increasing by orders of magnitude at temperatures well below T_c. This theory predicts only a very small, if any, change in the gap at such temperatures. Thus it appears that this gap-enhancement theory does not apply to our samples.

The second theory was first proposed by Lindelof[47] and has been developed on a more theoretical basis by Aslamazov and Larkin.[48] This theory supposes that since quasiparticles of energy less than the gap are trapped in the bridge, the effect of the microwaves is to broaden the spatial distribution of the quasiparticles. Since charge-neutrality must be preserved, the spatial distribution of paired electrons is also broadened. This idea is depicted schematically in Figure 4.20. This spatial broadening results in an increased pair density in the center of the bridge, thus increasing the critical current.

The idea that it is the change in the quasiparticles which is causing the increased critical current is supported by our observation of two criteria for enhanced superconductivity. If the microwave period is longer than both the Josephson period and the relaxation time τ_{eff}, the ac current is carried almost completely by the paired electrons; the quasi-particles are essentially unaffected. But if the ac current oscillates faster than either of these times, the quasiparticles are forced to carry some of this ac current and thus their spatial distribution is altered.
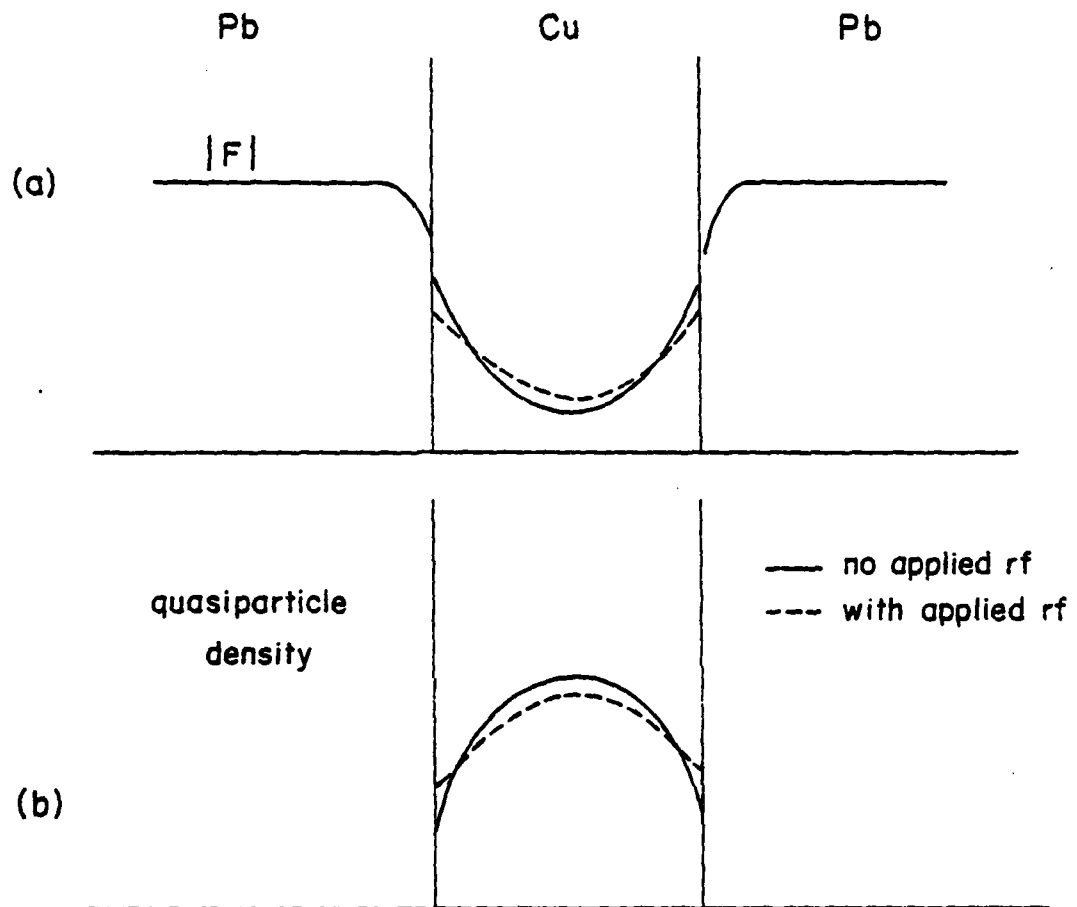
Figure 4.20 Schematic diagram of the change in the spatial distribution of (a) the paired-electron density and (b) the unpaired-electron (quasiparticle) density for a SNS junction when an rf field is applied.

This second theory does not predict an enhanced I_c in all-super-conducting microbridges far from T_c. In this case, the pair density is flat in the center of the bridge, and spatially broadening the pair density would not result in an increased pair density in the center of the bridge. Thus, this theory can explain why our samples show enhanced critical currents at all temperatures, while all-superconducting micro-bridges only show an enhanced I_c near T_c.

The gap-enhancement theories also predict an enhancement only near T_c for all-superconducting microbridges. This is due to the fact that, in contrast to our SNS samples, the relaxation time for all-superconducting microbridges gets shorter as the temperature is lowered. The gap-enhancement theories, however, have not been very successful in explaining the fact that, at least in some of the all-superconductor systems studied, longer bridges show a smaller enhancement than shorter bridges.

This spatial-averaging theory might also account for the low-voltage curvature in the dc I-V characteristics. In this region of the I-V, there is an oscillating voltage across the bridge, and thus there is an oscillating quasiparticle current. This oscillating quasiparticle current might broaden the spatial distribution of the paired electrons in the bridge, thus increasing the effective critical current. As the dc voltage across the bridge is increased, the quasiparticles oscillate faster and the critical current is increased. This increase in I_c as the voltage is raised causes an upward curvature in the I-V. This effect only applies for voltages less than $\hbar/2e\tau_{eff}$, since at voltages above this value the oscillating supercurrent decreases due to the inability of the supercurrent to oscillate with a period much shorter

than τ_{eff}.

The major difficulty in applying these theories to our samples is that the theoretical treatments have been done only for all-superconducting systems. It is certainly possible that a rigorous calculation for SNS systems might provide yet another explanation.

4.3.4 AC Josephson effect

It was mentioned in the introduction that when there is a voltage across a Josephson junction, the supercurrent oscillates in time. If both a dc and an ac current are used to bias the junction, the interaction between the oscillating supercurrent and the ac drive current produces constant-voltage steps in the dc I-V characteristics. These steps can be seen in Figure 4.15. If the junction is ideal, i.e., the current is sinusoidally dependent on the phase difference and there are no relaxation-time effects, the steps should occur only at dc voltages which are multiples of the voltage $V_{rf} = (\hbar/2e)\omega_{rf}$, where ω_{rf} is the frequency of the applied ac current. Furthermore, the step-height (the dc-current length of the step) oscillates as the magnitude of the ac current increases. Russer[49] has calculated on an analog computer the step-height versus the ac current level for an ideal junction for several values of ω_{rf}/ω_J ($\omega_J = (2e/\hbar)I_c R_o$). Figure 4.21 shows his results.

But the junctions produced in this work were not ideal. Even though the current-phase relation was sinusoidal, it has been shown in the previous sections of this chapter that there are strong relaxation-time effects present. The influence of this relaxation time on the I-V curves when the sample is driven with an ac and a dc current will be examined
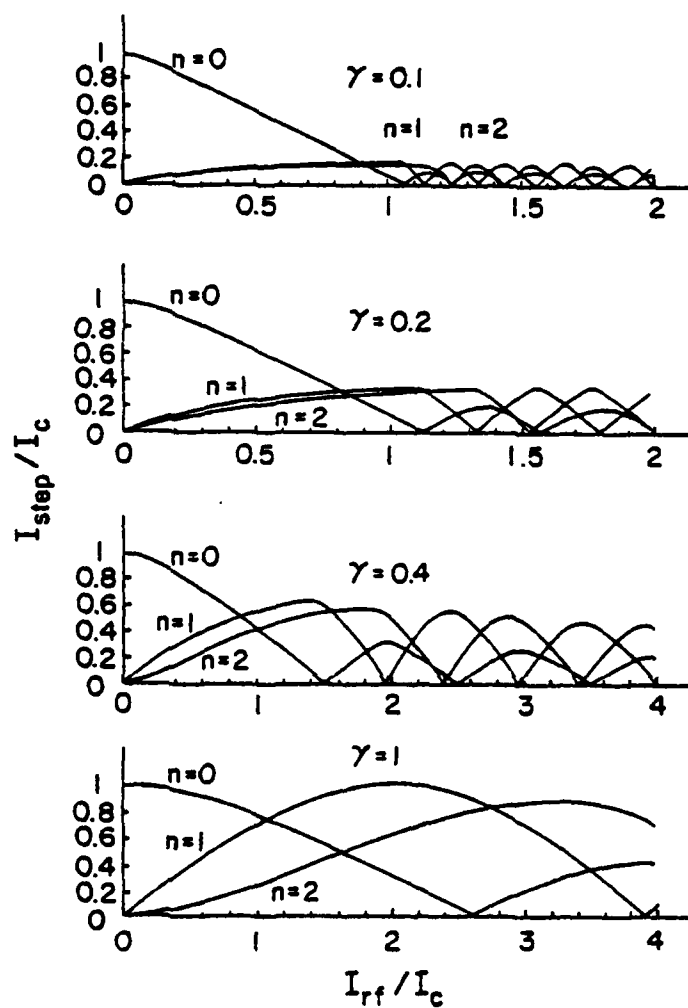
Figure 4.21 Theoretical calculation of the dependence of the critical current (n=0) and the first step (n=1) on the rf current level for an ideal resistively-shunted junction; $\gamma = \omega_{rf}/\omega_J$ (from Ref. 49).

for Pb-Cu-13; the rest of the samples studied showed similar effects.

Sample Pb-Cu-13 had an effective relaxation time τ_{eff} of 2.8 x 10^{-11} seconds. This corresponds to a frequency of 5.7 GHz. We have found that if the applied ac current was much less than 5.7 GHz, the data was some-what in agreement with the ideal-junction calculations. If the applied ac current was much higher than 5.7 GHz, the data was quite different than the ideal-junction calculations.

Figure 4.22 shows the I-V curves for various ac-current levels for an applied ac frequency of 1.94 GHz (ω_{rf}/ω_J = 1.41). It can be seen that the steps occur only at multiples of $(\hbar/2e)\omega_{rf}$ = 4.0 microvolts. Figure 4.23 shows a plot of the step-height versus ac current level for this I-V curve. Since Russer had not calculated the step-heights for ω_{rf}/ω_J = 1.4, we did a numerical calculation in the ideal-junction limit. (See the Appendix for the details of this calculation.) Note that the theory and data have similar curves; in particular, the magnitudes of the step heights agree. But the period of oscillation of the step heights with ac current level do not agree. This disagreement could be caused by the fact that the ac current had a magnitude such that regions of the I-V curve at voltages greater than $\hbar/2e \, \tau_{eff}$ were being sampled. Figure 4.24 shows 1.94 GHz step-height data for the same sample, but at a higher temperature. Again, the qualitative behavior is similar to that pre-dicted by the ideal-junction calculations. In addition, the I-V curve at this temperature only showed steps at voltages which were multiples of $(\hbar/2e)\omega_{rf}$.

Figure 4.15 shows I-V curves for 10.0 GHz applied ac currents. Note

Figure 4.22 I-V curves for Pb-Cu-13 with 1.94 GHz applied microwave
radiation; T = 6.34 K and ω_{rf}/ω_J = 1.41.
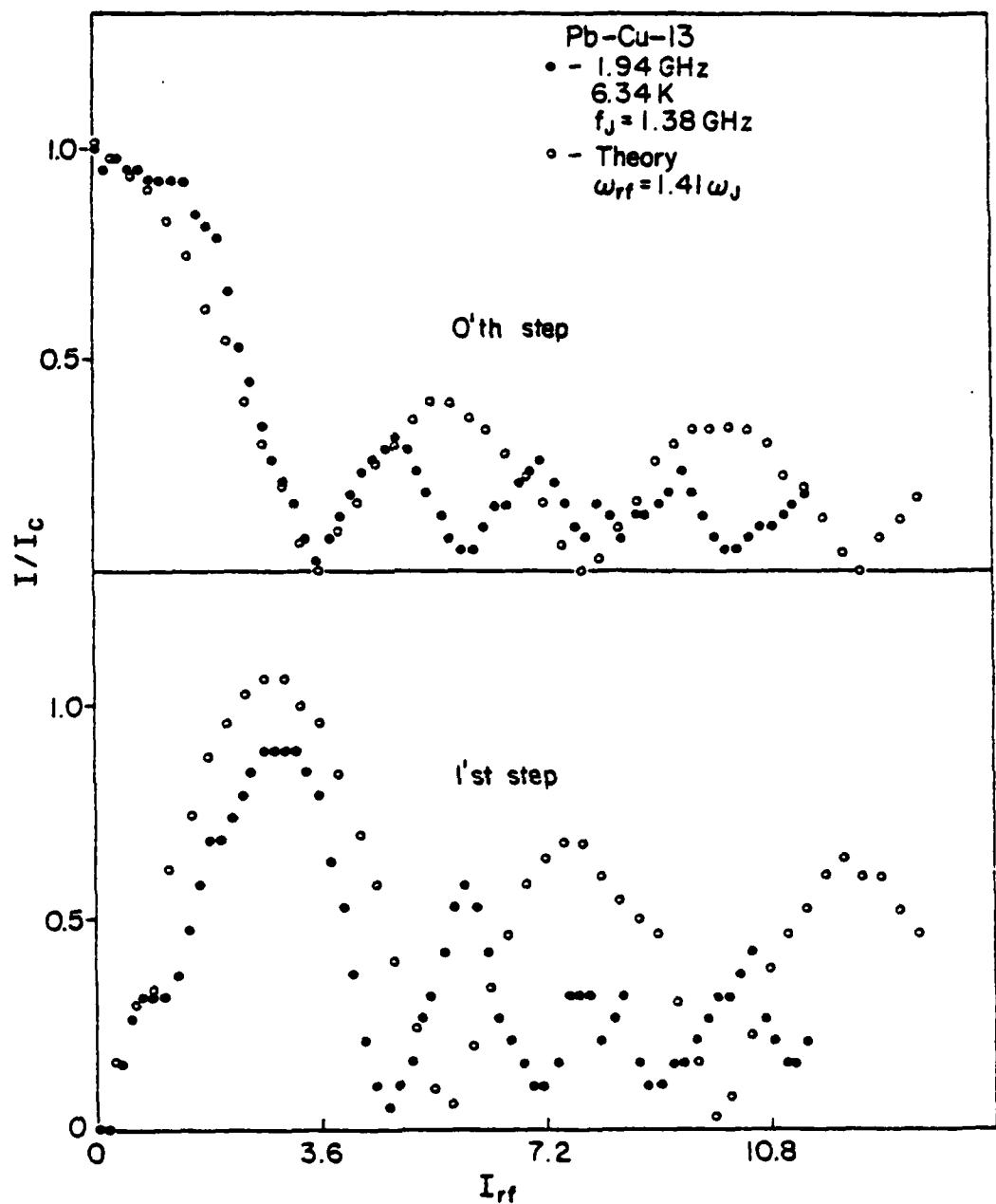
Figure 4.23 Step-height versus rf current level for the critical
current (0'th step) and the first step of the data in
Figure 4.22. The open circles are the results of a numerical
calculation for an ideal junction with ω_{rf}/ω_J = 1.41 (see
the Appendix for details). The data has been normalized to
the calculation by requiring the critical currents at
I_{rf} = 0 to agree and by requiring the first zeros of the 0'th
step to occur at the same value of I_{rf}.

Figure 4.24   Step-height versus rf current level for the 0'th and 1'st
              steps for Pb-Cu-13, with f_{rf} = 1.94 GHz, T = 6.69 K, and
              ω_{rf}/ω_J = 4.2

that in addition to steps appearing at multiples of $V = (\hbar/2e)\omega_{rf}$ (20 microvolts), there are constant-voltage steps at submultiples of this voltage. These are often called subharmonic steps. Figure 4.25 shows the step height versus ac current level for these I-V's. There are two features which are not in agreement with the predictions of the analog and numerical calculations: First, the variation of step height with ac current level is somewhat erratic. Second, there is an initial increase in the critical current, and the maximum height of the first step exceeds the zero-power critical current. This is the enhanced critical current discussed previously in this chapter.

Figure 4.26 shows I-V curves for ac currents at 24 GHz ($(\hbar/2e)\omega_{rf}$ = 50 microvolts), and Figure 4.27 shows the corresponding step height versus ac current level data. At this frequency, there are strong sub- harmonic steps, and the step height versus ac current level data is quite different from that expected from the calculations. In addition, the critical-current has been enhanced so much that the I-V curve becomes hysteretic.

It has been found that this behavior occurs for all the samples measured. If $\omega_{rf} \ll 1/\tau_{eff}$, the resulting I-V curves with an ac current drive are quite similar to those predicted by both analog and numerical calculations. If $\omega_{rf} \gg 1/\tau_{eff}$, there are constant-voltage steps at submultiplies of $(\hbar/2e)\omega_{rf}$, and the step height versus ac current level data is quite different from that predicted by the calculations.

It has also been observed that, for Pb-Cu-13 at least, the constant-voltage steps can be seen at dc voltages as high as two millivolts. In

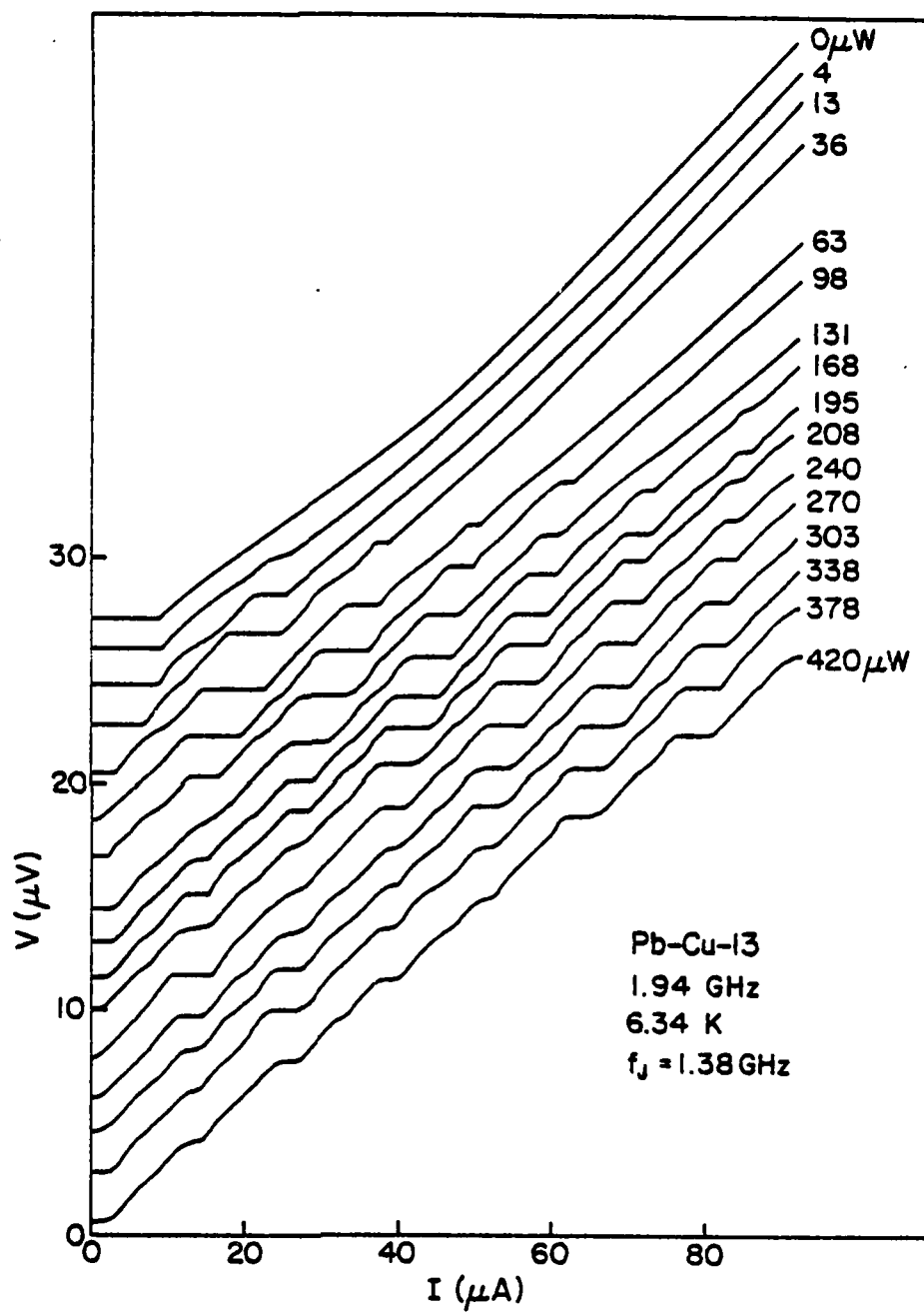Figure 4.25   Step-height versus rf current level for the 0'th and
1'st steps of Figure 4.15.

Figure 4.26   I-V curves for Pb-Cu-13 with 24 GHz applied microwave radiation.   T = 4.28 K and ω_{rf}/ω_J = 1.61.
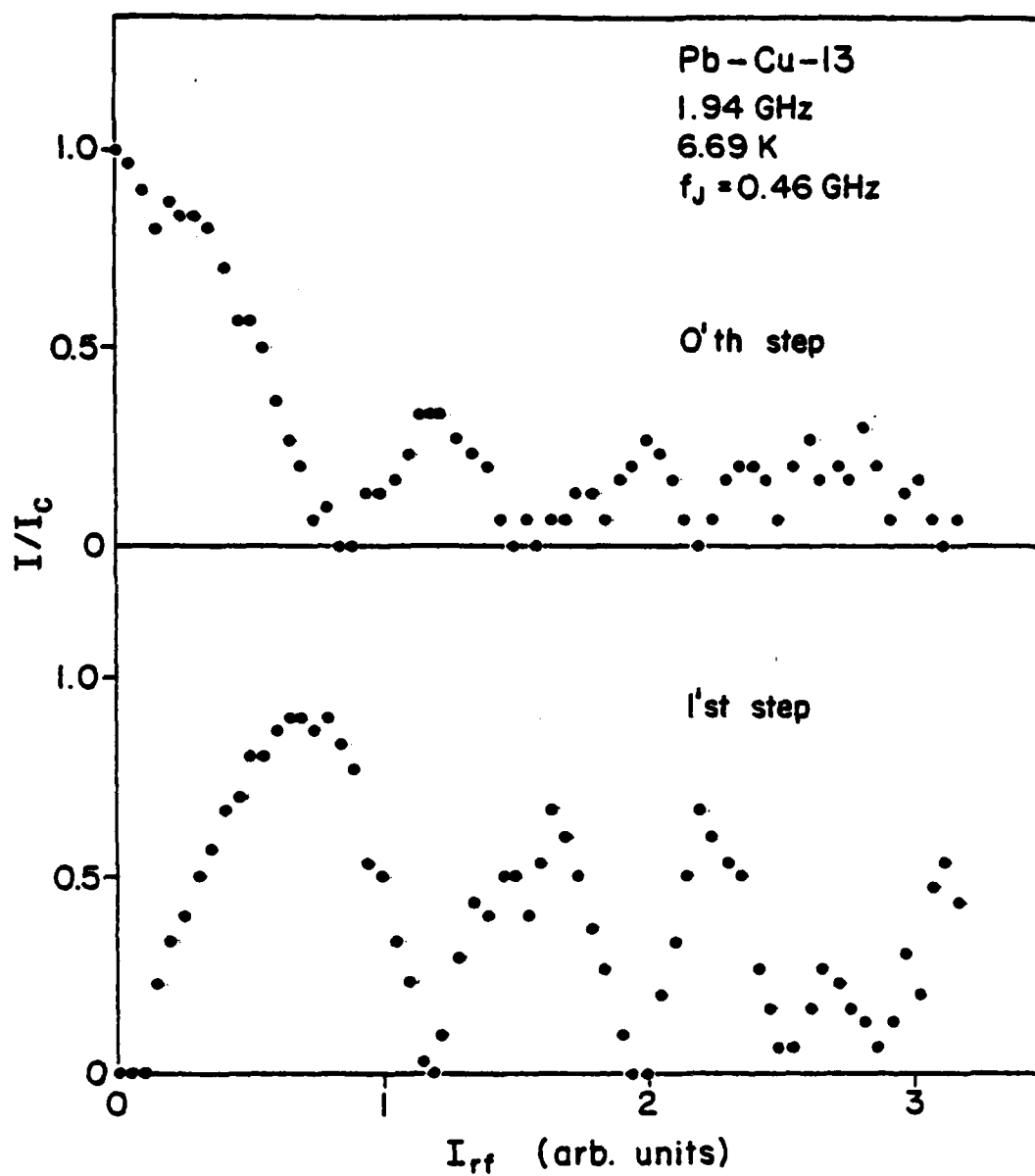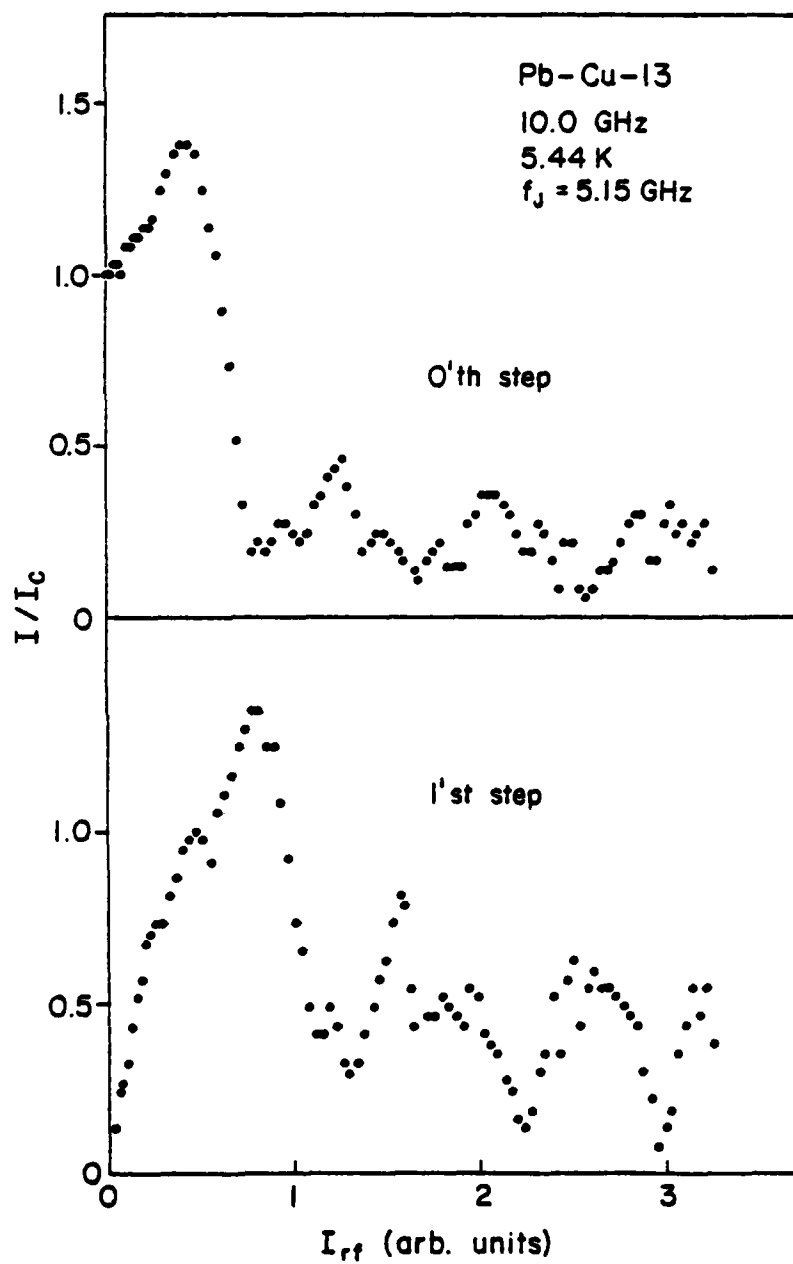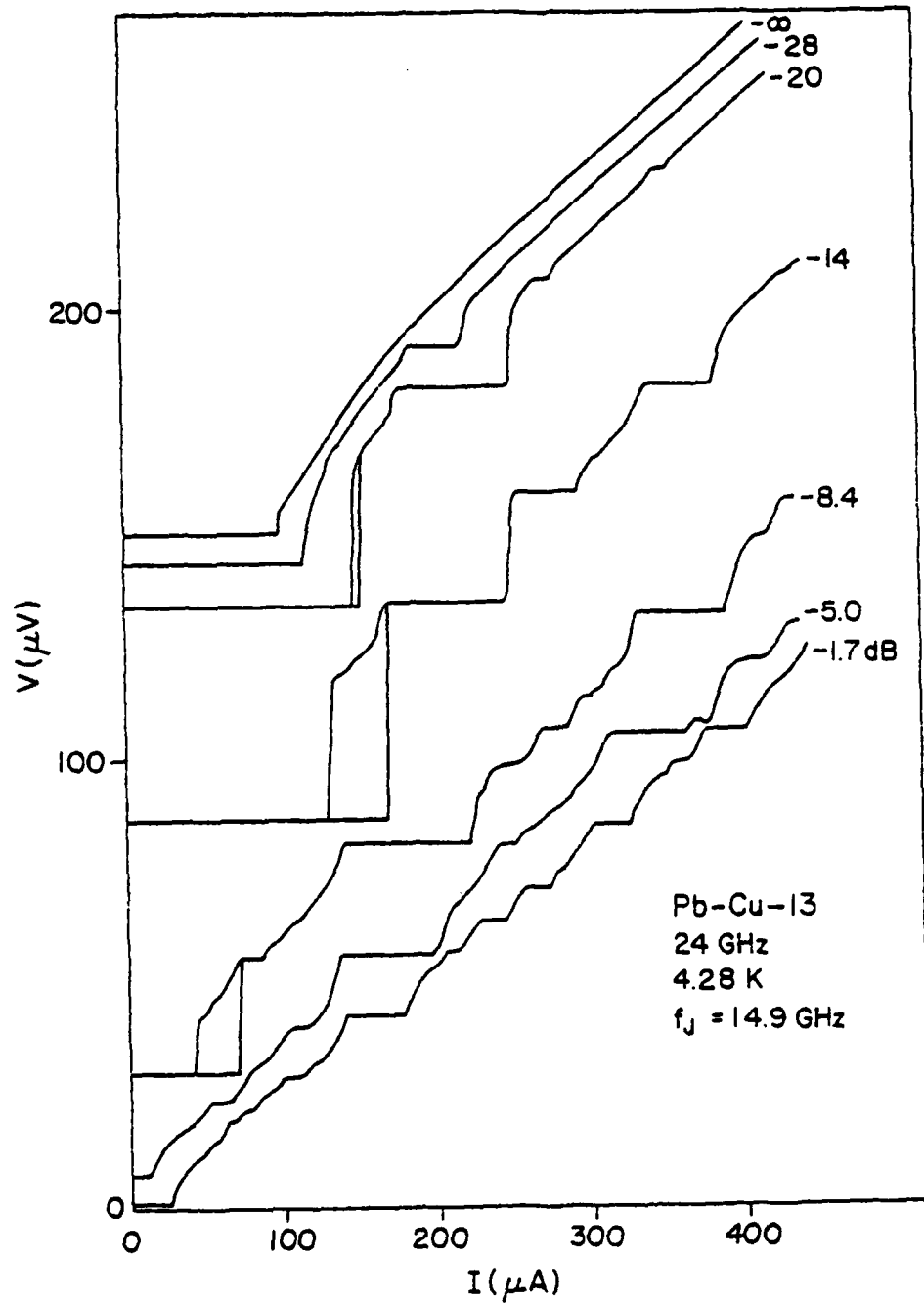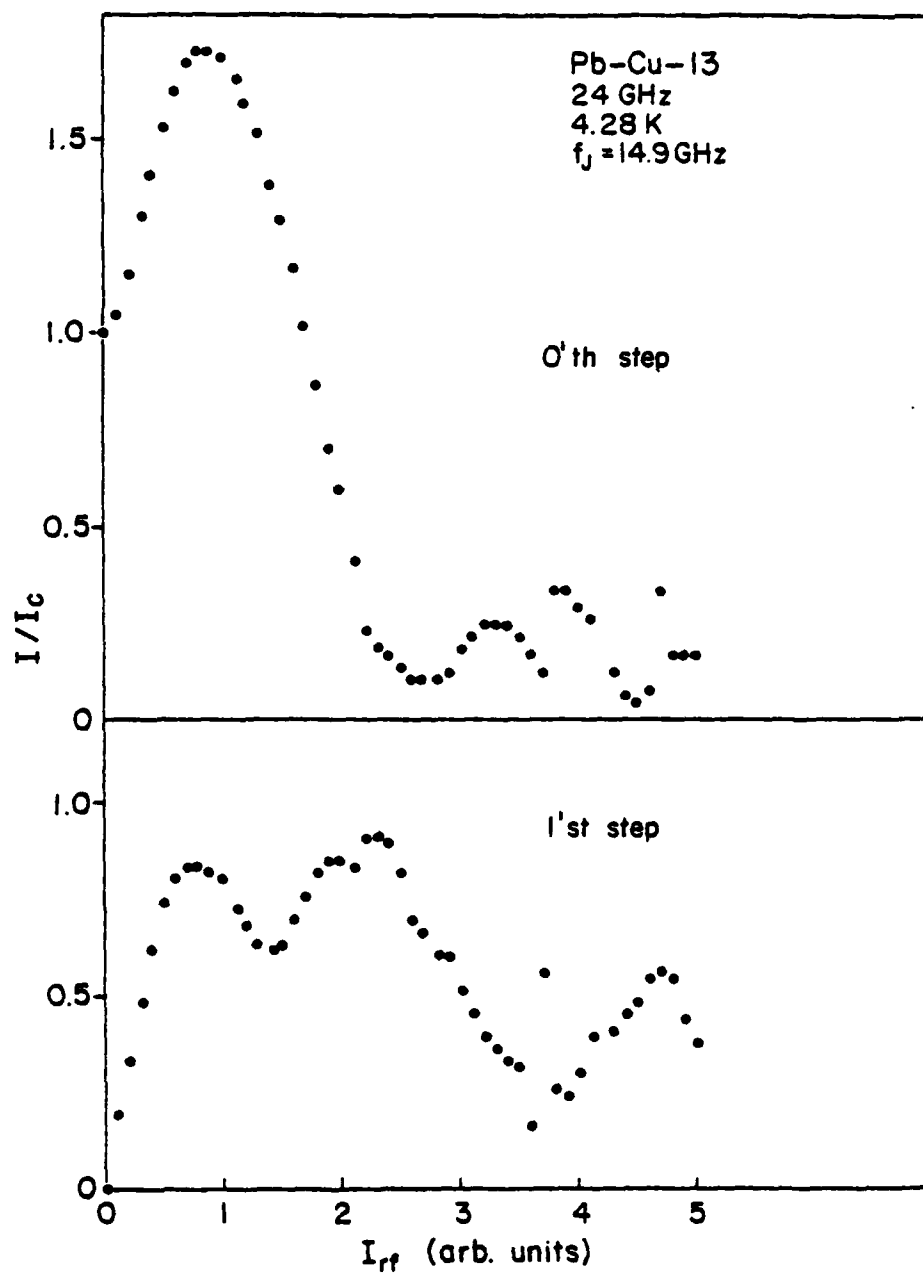
Figure 4.27 Step-height versus rf current level for the 0'th and 1'st steps of Figure 4.26.

previous discussions in this chapter it was speculated that above V_{lower} (about fifty microvolts) the bridge acted as if it were completely normal. It would thus seem that there is a contradiction. In fact, however, there is no contradiction, as the following argument will show. Figure 4.28 shows the results of an ideal-junction numerical calculation for $\omega_{rf} = \omega_J$, and for a dc voltage of 10 $I_c R_o$ = 10 $(\hbar/2e)\omega_J$. It can be seen that the supercurrent has two frequencies of oscillation, one much faster than ω_J and one much slower than ω_J. (This is just a result of the oscillating supercurrent beating against the applied ac current.) Now if a relaxation time equal to $1/\omega_J$ is introduced, as seen in Figure 4.29, there are again two frequencies of oscillation; the high-frequency oscillation of the supercurrent is significantly suppressed, but at some times there is still a significant supercurrent. It is this remaining supercurrent which is responsible for the observation of the constant voltage step at voltages much higher than $\hbar/2e\tau_{eff}$. (A relaxation time was introduced into the calculation by suppressing the oscillating supercurrent by a factor dependent on the instantaneous voltage across the bridge, i.e.,

$$I_s = I_c \sin\phi/(1 + V^2/V^2_{relax})$$

where V is the instantaneous voltage across the bridge and $V_{relax} = \hbar/2e\tau_{relax}$. See the Appendix for details of this calculation.)

It is important to realize that it is the presence of the applied ac current which gives rise to an ac supercurrent. If the applied ac current were absent, there would be no supercurrent. Thus, the observation of a constant-voltage step at a high dc voltage V does not imply

Figure 4.28 Numerical simulation of the supercurrent (I_S) versus time for an ideal resistively-shunted junction with applied rf radiation. I_{DC} = 10 I_c, I_{rf} = 10 I_c, ω_{rf} = ω_J = $(2e/\hbar)I_c R_0$. The time is measured in units of τ_J = $1/\omega_J$.
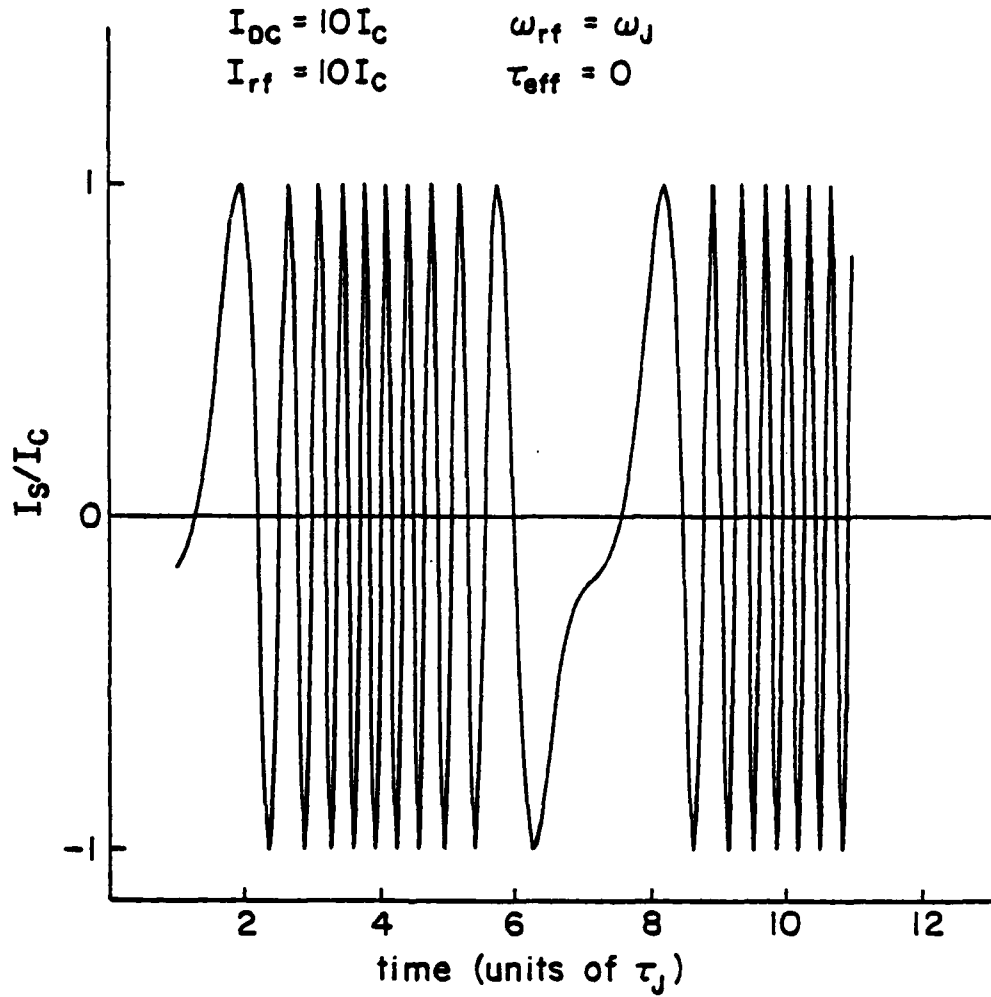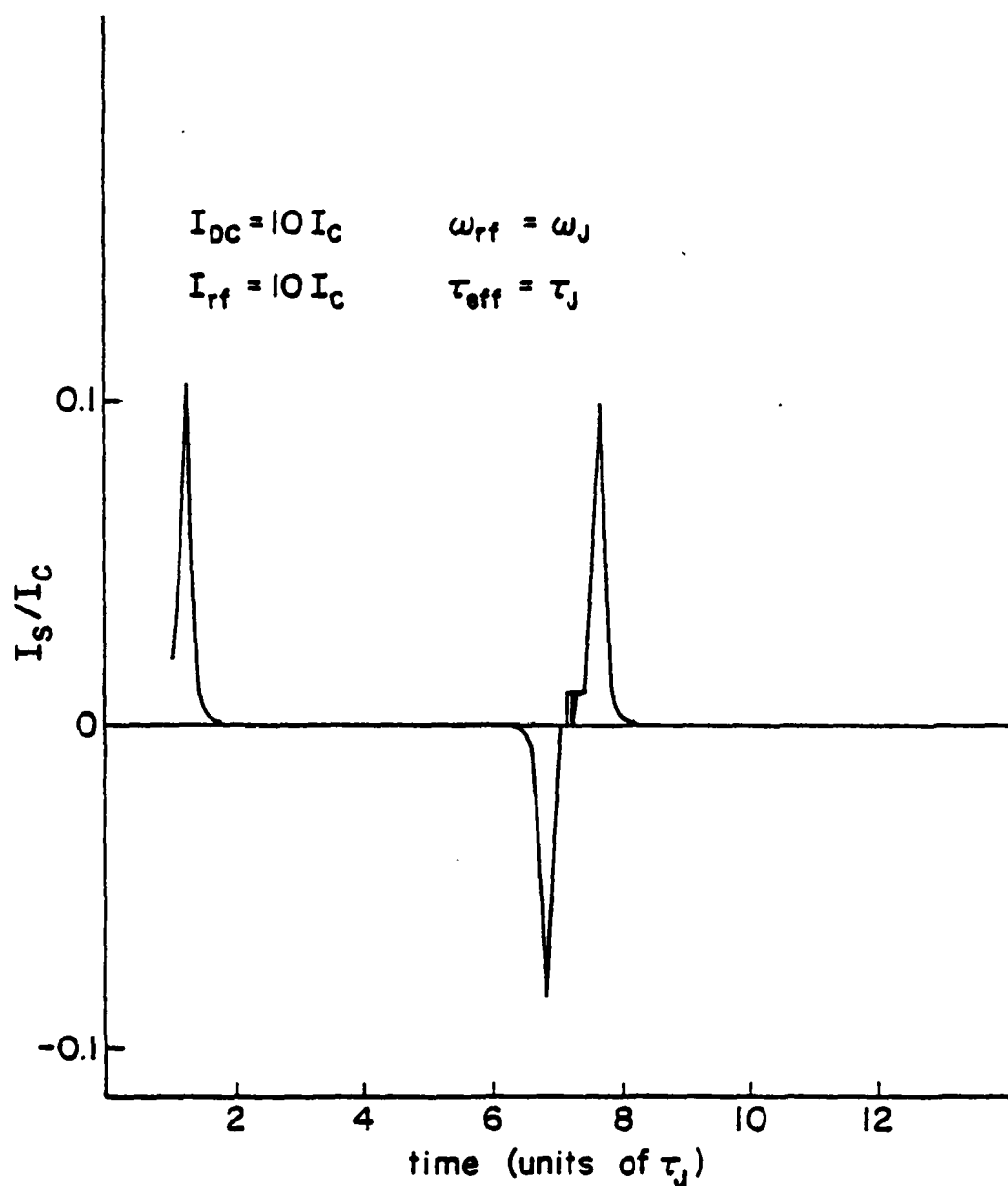
Figure 4.29 Numerical simulation of the supercurrent (I_s) versus time
for a resistively-shunted junction with an intrinsic relaxa-
tion time τ_{eff} and an applied rf current. $I_{DC} = 10\ I_c$,
$I_{rf} = 10\ I_c$, $\omega_{rf} = \omega_J$, and $\tau_{eff} = 1/\omega_J$. (See the Appendix
for the details of this simulation.)

that there is a supercurrent oscillating with frequency $2eV/\hbar$. In order to establish that a supercurrent is oscillating at $2eV/\hbar$, it is necessary to see a constant-voltage step with an applied ac current of frequency $\omega_{rf} = 2eV/\hbar$.

The observation of a high-voltage step does imply that joule heating has not heated the bridge to the point where there can no longer be a supercurrent, since no amount of mixing with an applied ac current could then result in a reappearance of a supercurrent. Thus the observation of a step at 2 mV implies that the hysteresis in the I-V seen at 50 microvolts is not caused by heating.

4.3.5 Previous experimental observations of the ac Josephson effect in SNS structures

Clarke[35] applied very low frequency (< 2 MHz) radiation to his junctions and observed both harmonic and subharmonic steps. He attributed the subharmonic steps to the large capacitance of his junctions. This is probably correct since his layered structures had significant capacitance. He also found that the step-height versus ac current level was similar to that predicted by calculations.

Komarovskikh et al.[36] observed steps at 39.8 GHz in their planar junctions, but very little additional information was reported.

4.4 Dynamic Resistances and the High-Voltage I-V

The three previous sections of this chapter dealt with phenomena associated with the existence of supercurrents across the SNS sample. The experimental I-V curves also showed features which were not due to supercurrents, but which instead were due to the influence the SNS

interface had on the density of states (and the occupation of these states) in the adjoining superconductor and normal metal. These non-supercurrent-related effects are the subject of this section.

4.4.1 Experimental results

Figure 4.30 shows a dc I-V curve for Pb-Cu-13 with the voltage ranging from zero to six millivolts. The supercurrent-related features are only present below one millivolt; the remainder of the I-V shows only a very weak strucutre. Figures 4.31 and 4.32 show dV/dI data for this sample; it can be seen that the weak features of the I-V curve are very pronounced on the dV/dI curves. Figure 4.33 shows a similar dV/dI curve for Pb-Cu-7.

Figure 4.34 shows a series of dV/dI curves for Pb-Cu-13, thus illustrating the temperature dependence of the various features. The 7.326 K curve was taken above the T_c of the banks; note that in all of the other curves the magnitude of dV/dI never exceeds the normal state resistance obtained at 7.326 K.

There are two features of the dV/dI curves which will be examined in detail. The first feature is the flat region occurring between about 0.1 mV and 1 mV. This is the constant-resistance region between V_{lower} and V_{upper} which has been discussed previously; the magnitude of this voltage-independent resistance was previously designated by R_0. Figure 4.35 shows the temperature dependence of R_0. At low temperatures R_0 is nearly constant, while close to T_c the resistance R_0 increases rapidly with temperature.

The second interesting feature is the large peak in the dV/dI curve
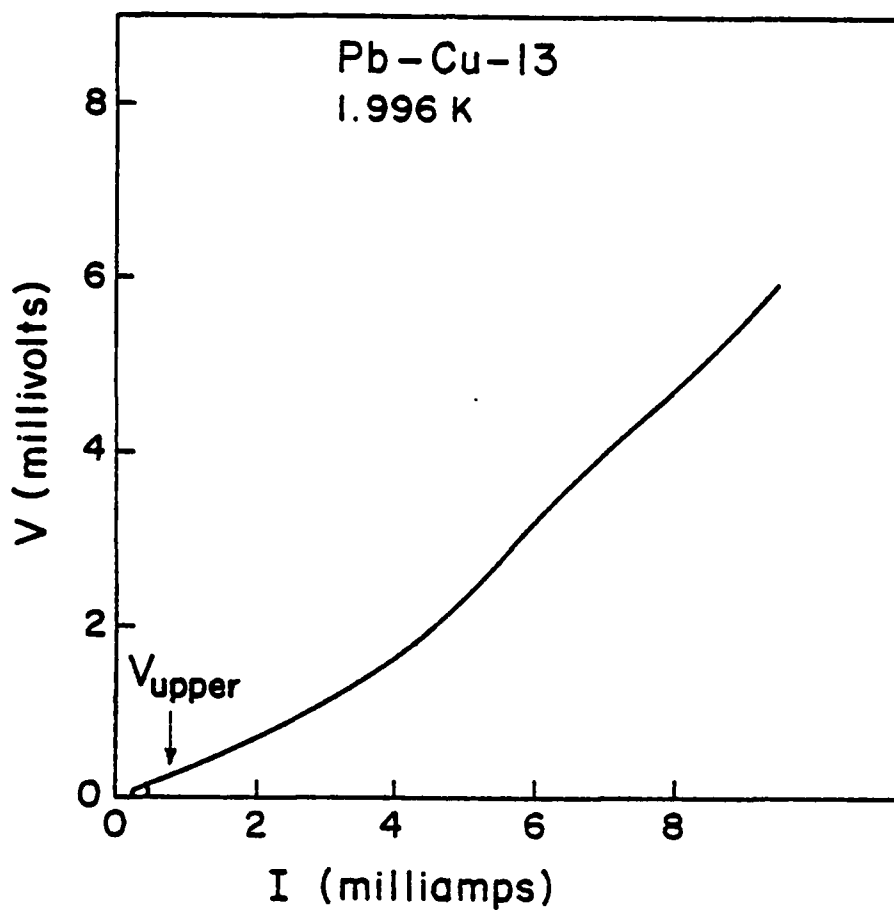
Figure 4.30   High-voltage I-V curve for Pb-Cu-13 at T = 1.996 K.
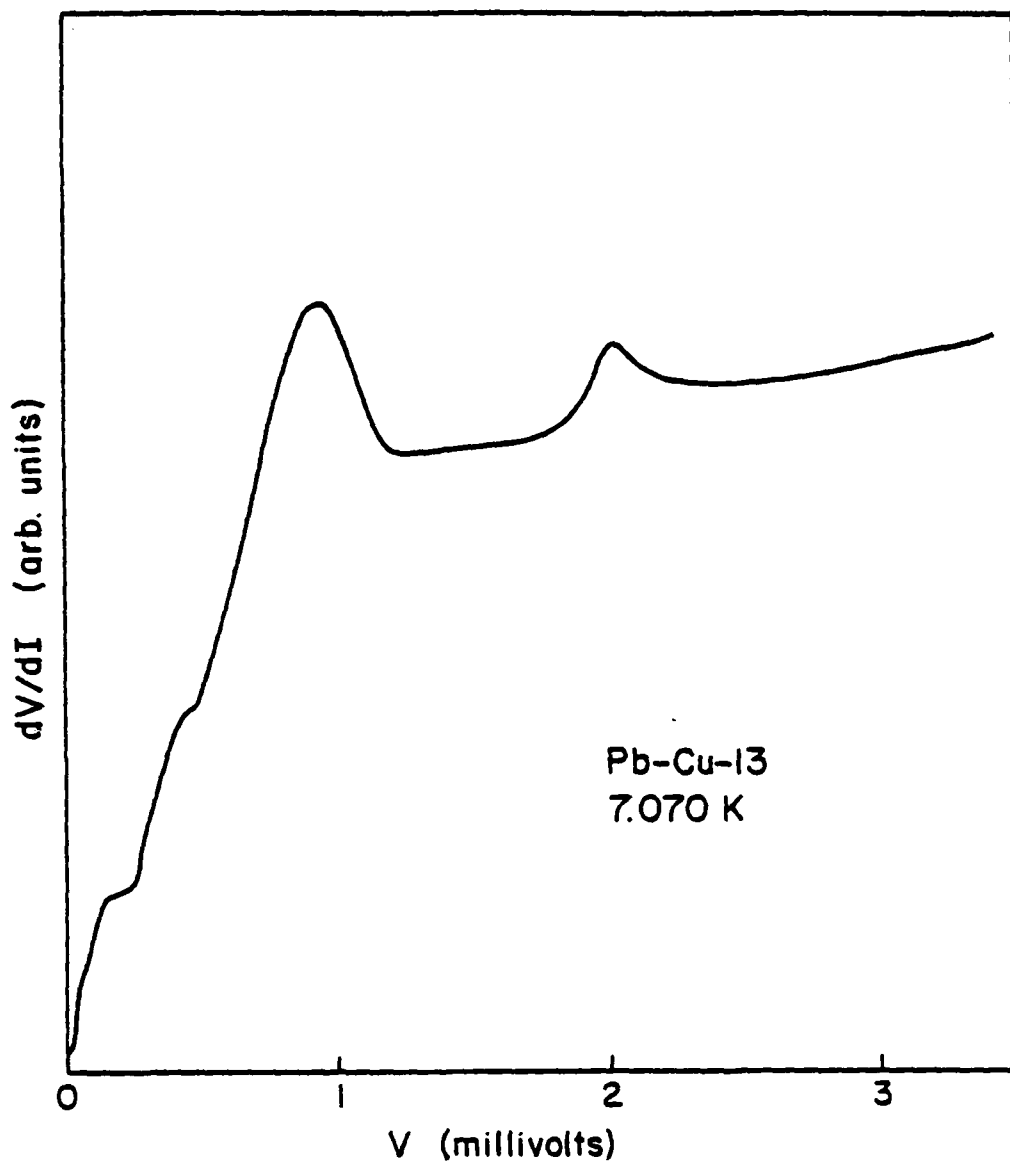
Figure 4.31   dV/dI versus V curve for Pb-Cu-13, T = 7.070 K.
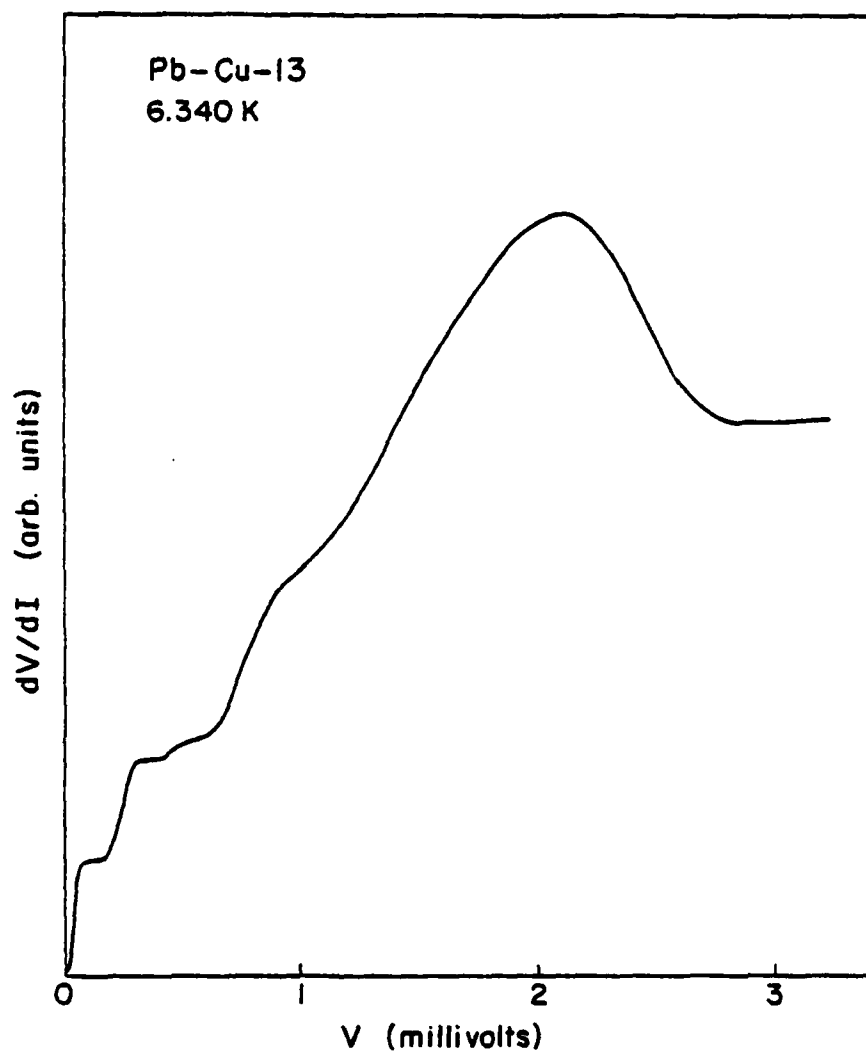
Figure 4.32   dV/dI versus V curve for Pb-Cu-13, T = 6.340 K.
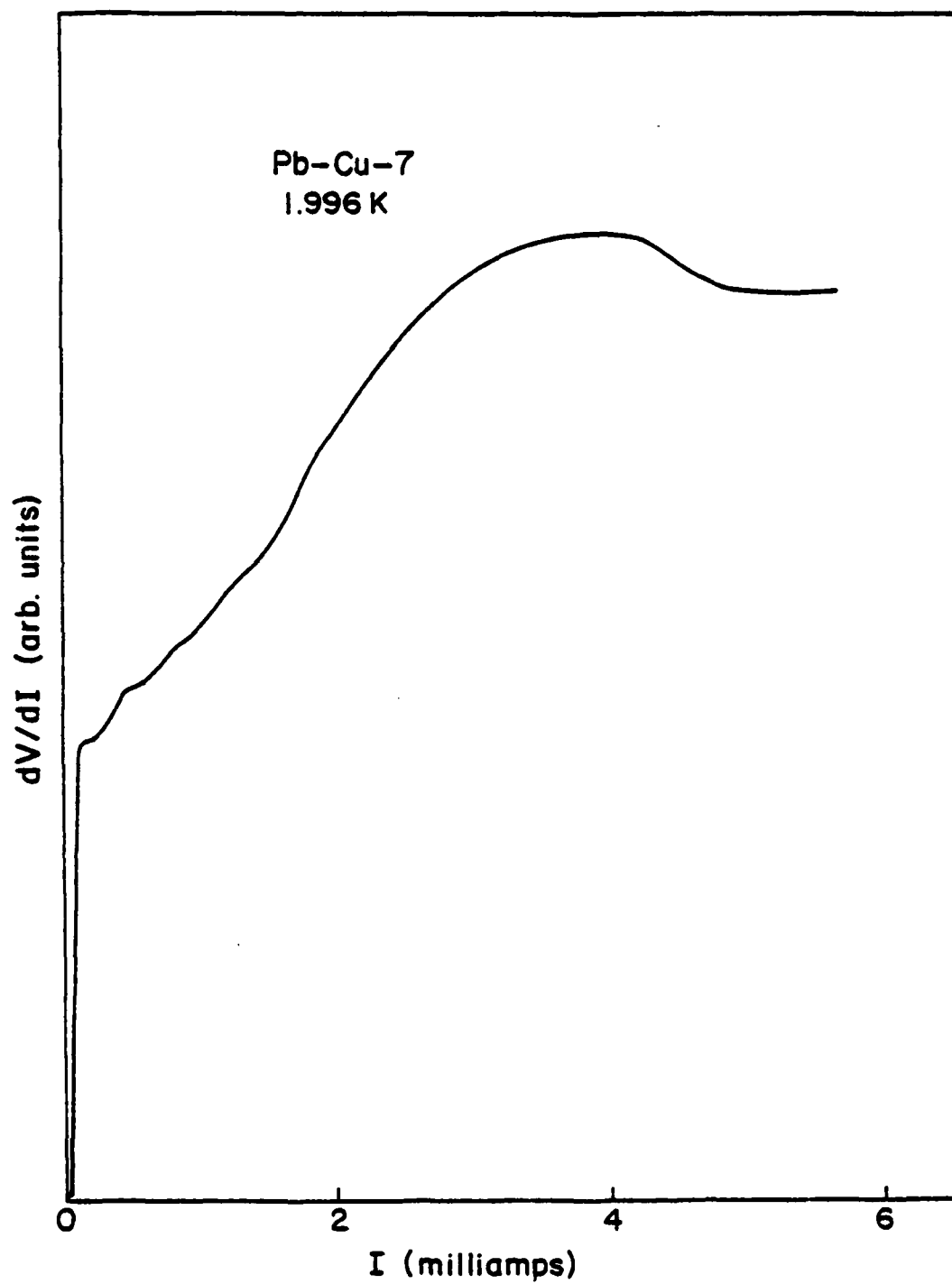
Figure 4.33 dV/dI versus I for Pb-Cu-7, T = 1.996 K.
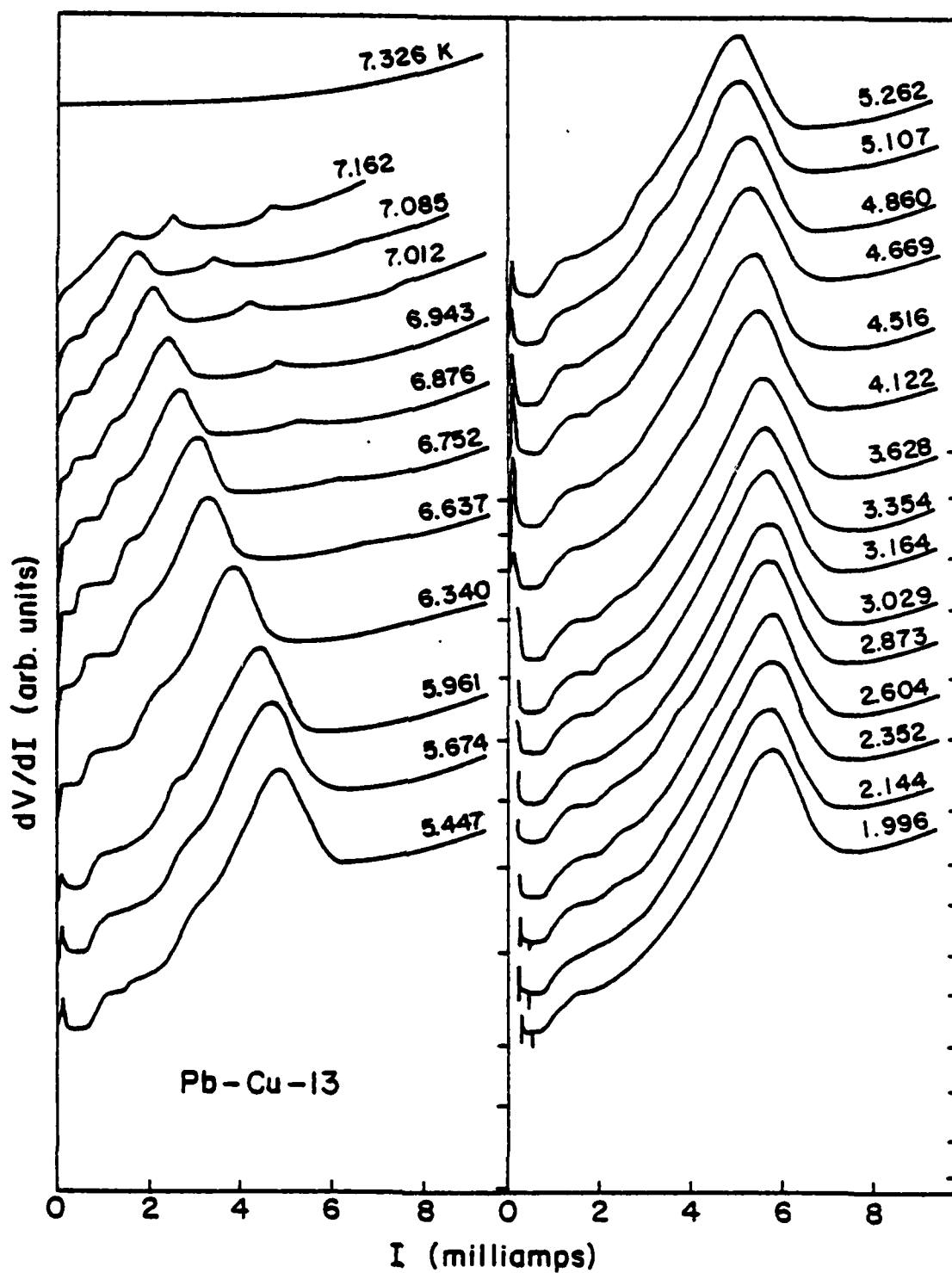
Figure 4.34 dV/dI versus I for Pb-Cu-13 for several temperatures.
The tic marks on the right-hand sides of the figure indicate
the points where dV/dI = 0 for each curve.
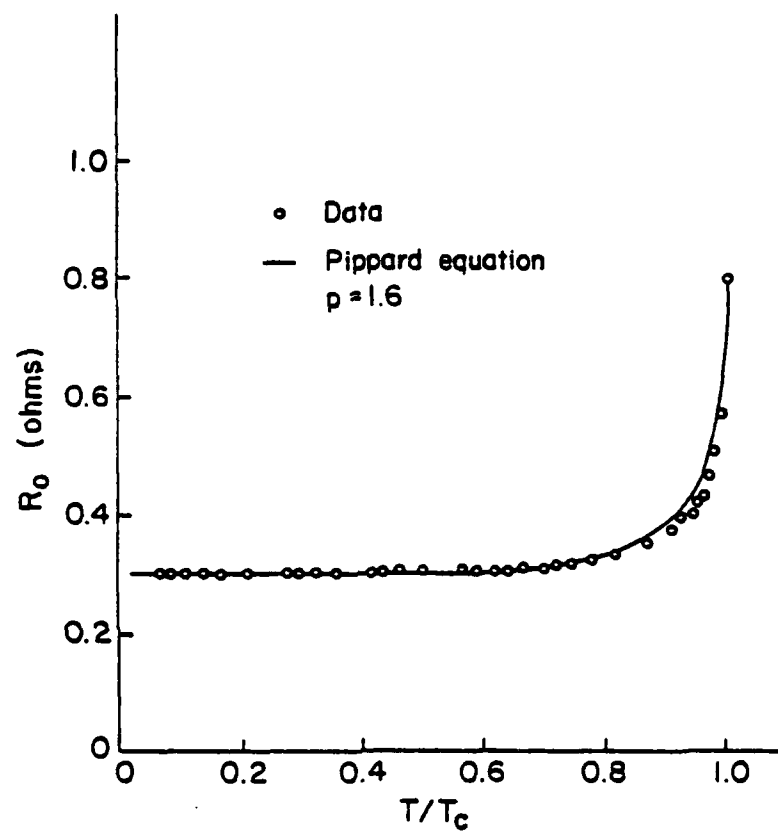
Figure 4.35 Temperature dependence of R_0 for Pb-Cu-13. The solid curve is a fit to the phenomenological equation of Pippard et al. (Ref. 50), with p = 1.6.

which occurs near 2.7 mV at low temperatures. Figure 4.36 shows the temperature dependence of the voltage at which this peak occurs. At temperatures very close to T_c there is a second, smaller peak occurring at about twice the voltage of the large peak.

In addition to these two features, there are smaller bumps occurring between the flat region of R_0 and the large peak. It will be argued below that these bumps are probably related to the large peak.

4.4.2 Theoretical considerations and previous experimental work
The temperature dependence of R_0

The resistance of a superconducting-normal interface was first measured by Pippard and co-workers.[50,51] They used SNS structures with copper as the normal metal and lead or tin as the superconductor. Their experimental results were very similar to our measurements of the temperature dependence of R_0.

Pippard et al. were also the first to provide an explanation for the observed data. A brief summary of their theory will be given here.

Andreev[52] first developed the nature of the transport of electrons across an SN interface. He found that if an electron in the normal metal encounters the interface, what happens to it depends on its energy. If the electron has an energy much greater than the gap of the super-conductor, it simply travels across the interface. But if the electron has an energy less than the gap of the superconductor, the electron does not simply cross the interface; instead, the electron from the normal metal combines with a quasiparticle in the superconductor to form a condensed pair, and a hole is ejected back into the normal metal. Thus,

an electron with energy less than the gap is reflected as a hole going in the opposite direction.

Pippard et al. pointed out that if an electron in the normal metal penetrates into the superconductor it will be out of equilibrium; it will scatter inelastically for a while, and eventually combine with another quasiparticle to form a pair. This scattering and subsequent recombination causes energy dissipation in the superconductor, thus giving rise to an extra resistance. In addition, there will now be an electric field in the superconductor due to the non-equilibrium quasiparticle distribution. (Artemenko et al.[55] have calculated that this electric field consists of an initial jump in the electric field at the interface, followed by an exponentially decaying electric field with a decay length $\lambda_b = (4D\tau_e T/\pi\Delta)^{\frac{1}{2}}$ where D is the diffusion constant and τ_e is the inelastic scattering time. Dolan and Jackel[53] directly measured this exponentially decaying electric field and found, for tin, that $\lambda_b(T) \simeq (1.5)(1 - T/T_c)^{0.23}$ microns).

The magnitude of this extra resistance depends on the number of electrons penetrating into the superconductor. At low temperatures, nearly all of the electrons in the normal metal will have energy less than the gap, and there will be very little extra dissipation. As the temperature is raised, the gap decreases and the energy spread of the electrons in the normal metal increases, thus the number of electrons with energy greater than the gap increases. The number of electrons penetrating the superconductor increases, and the extra dissipation increases.

Pippard et al., using a phenomenological model, calculated that the resistance of an SNS junction should be given by

$$R_0/R_{0K} = (1+C)/[1 + C \tanh(p\Delta_\infty/2k_BT)]$$

where p is a constant, R_{0K} is the resistance at T=0, Δ_∞ is the gap in the superconductor far from the interface, and $C = R_0(T_c)/R_{0K} - 1$. Pippard et al. found from their experimental data that p was between 1.4 and 1.7. Figure 4.35 shows a fit of our data to this equation, and the fit is good using p = 1.6.

Since the work of Pippard et al., many authors have attempted to improve on the somewhat phenomenological theory of Pippard et al. by performing rigorous, microscopic calculations. All of these authors have computed the resistance to be $R_0 = R_{0K} + R'$, where R' is the extra resistance. Schmid and Schön[54] found that $R' \sim (1 - T/T_c)^{-0.37}$ (for lead electrodes), Artememko et al.[55] found $R' \sim (1 - T/T_c)^{-0.25}$, and Krähenbühl and Watts-Tobin[56] found $R' \sim (1 - T/T_c)^{-0.63}$. All of these microscopic theories should be applicable for $0.85 < T/T_c < .99$.

We have fit our data to the equation $R_0 = R_{0K} + R_1(1 - T/T_c)^{-\rho}$. We have found that the best fit is for $\rho = 0.11$, as seen in Figure 4.36. The difficulty with this fit is that this gives a value of R_{0K} which is negative, a result which is clearly not physically possible. We thus conclude that our data cannot be fit by this equation. The reason for the inability of the microscopic theories to describe our data is not known. It is possible that the microscopic theories do not apply because they were worked out for a single SN interface; they do not include the effect that one of the superconducting banks has on the other, as a result of the change in the occupied density of states of the normal metal. (The phenomenological model of Pippard et al. did contain a two-interface
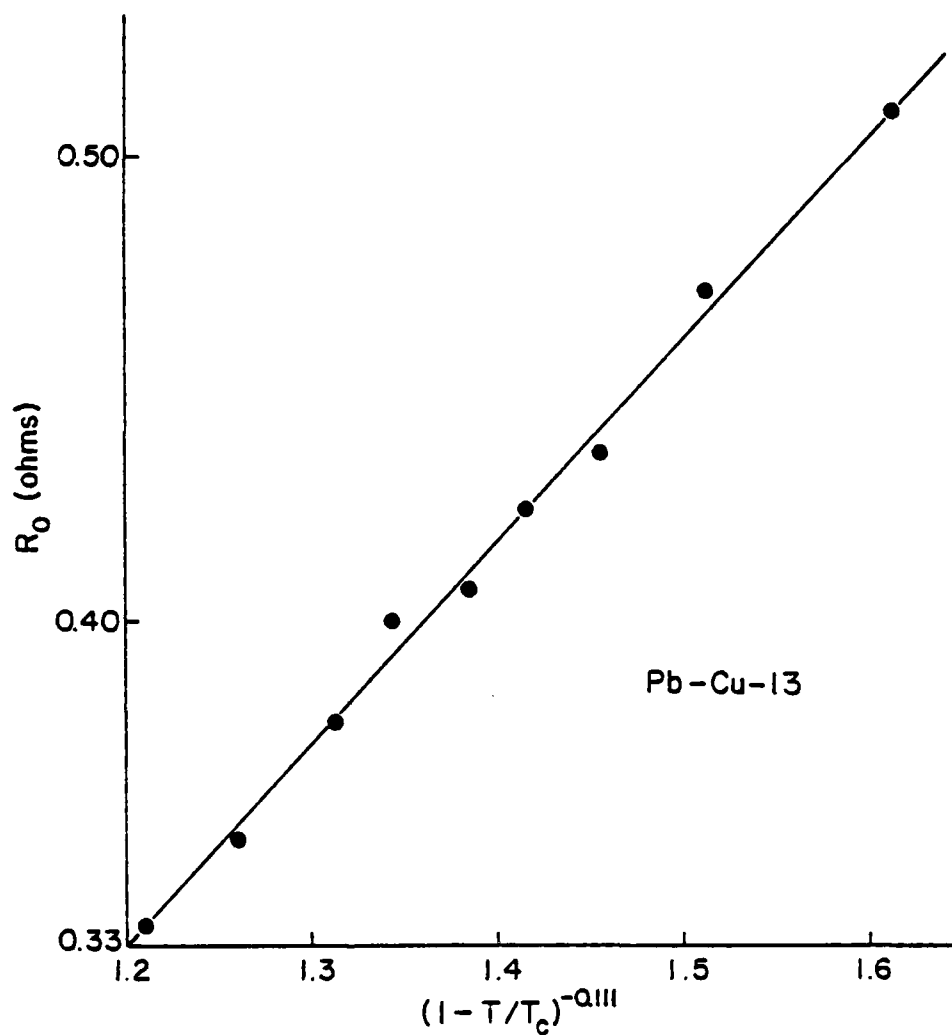
Figure 4.36 R_0 versus $(1-T/T_c)^{-.111}$ for Pb-Cu-13, for $T/T_c > 0.8$. The straight line is the function

$R_0 = -0.19$ ohms $+ .435$ ohms $(1-T/T_c)^{-.111}$.

SNS junction, however.)

High-voltage structure

The peak in the dV/dI curve which occurs at high voltage (V $\sim$ 2 mV) was not observed in any of the previous studies of SNS structures, since these studies did not measure the I-V at such high voltages. However, a similar peak in the dV/dI curve of SN point contacts has been observed by Kaiser-Dieckhoff.[57]

Wang et al.[58] observed peaks in the dV/dI curves of niobium micro-bridges at a voltage corresponding to the gap in the bridge. They attributed this peak to self-coupling to the Josephson oscillation at high temperatures and to the presence of a hot-spot in the bridge at lower temperatures. Gregers-Hansen et al.[59] observed peaks in the dV/dI curves of planar indium microbridges at voltages corresponding to subharmonics of the gap voltage. They attributed this structure to pair-breaking by subharmonics of the Josephson oscillation. The peak in our dV/dI curves cannot be explained by coupling to Josephson radiation since at these high voltages there was no oscillating supercurrent observed in our microwave experiments. The possibility that heating is the cause of our peak will be discussed below.

Since none of the theories of SNS junctions or SN interfaces have considered such high voltages, we cannot look to those theories for an explanation. Instead a somewhat speculative explanation will be given here.

It has been mentioned above that electrons from the normal metal which penetrate into the superconductor cause an extra resistance, and the magnitude of this extra resistance depends on the number of electrons

in the normal metal which have an energy greater than the energy gap in
the superconductor. Now if a voltage V is established across the bridge,
the mean electron energy (with respect to the fermi energy) at the low-
energy end of the bridge will be higher than it would be if V = 0. (This
is due to the fact that for our copper bridges the mean free path was
about 15 nm; since the inelastic collision time for copper at low tempera-
tures is about 10^{-10} seconds[60], this gives a mean diffusion distance between
inelastic collisons of

$$\lambda_e = \left(\frac{v_f \Lambda \tau_e}{3}\right)^{\frac{1}{2}} \approx 0.9 \ \mu m.$$

This distance is longer than the length of our normal metal bridges.)
Thus, as the voltage across the bridge increases, the number of electrons
penetrating into the superconductor increases, as illustrated in Figure
4.38. In Figure 4.38a, most of the electrons in the normal metal bridge
are below the gap, and the extra resistance is low. In Figure 4.38b,
the peak in the electron distribution is nearly at the gap, and the extra
resistance is increased. In Figure 4.38c, the peak in the energy distri-
bution is far above the gap. (In fact, the number of electrons with
energy just above the gap is less in (c) than in (b).) But now, since
most of the electrons are entering the superconductor far above the gap,
the extra resistance is decreased from (b) because high-energy quasi-
particles combine faster than low-energy quasiparticles.[64] (This increase
in the recombination rate is due to the fact that the phase space
available to the emitted phonon varies as Ω^2, where Ω is the phonon
energy. If a quasiparticle of energy Δ combines with another quasi-
particle with energy Δ, the available phase space is proportional to
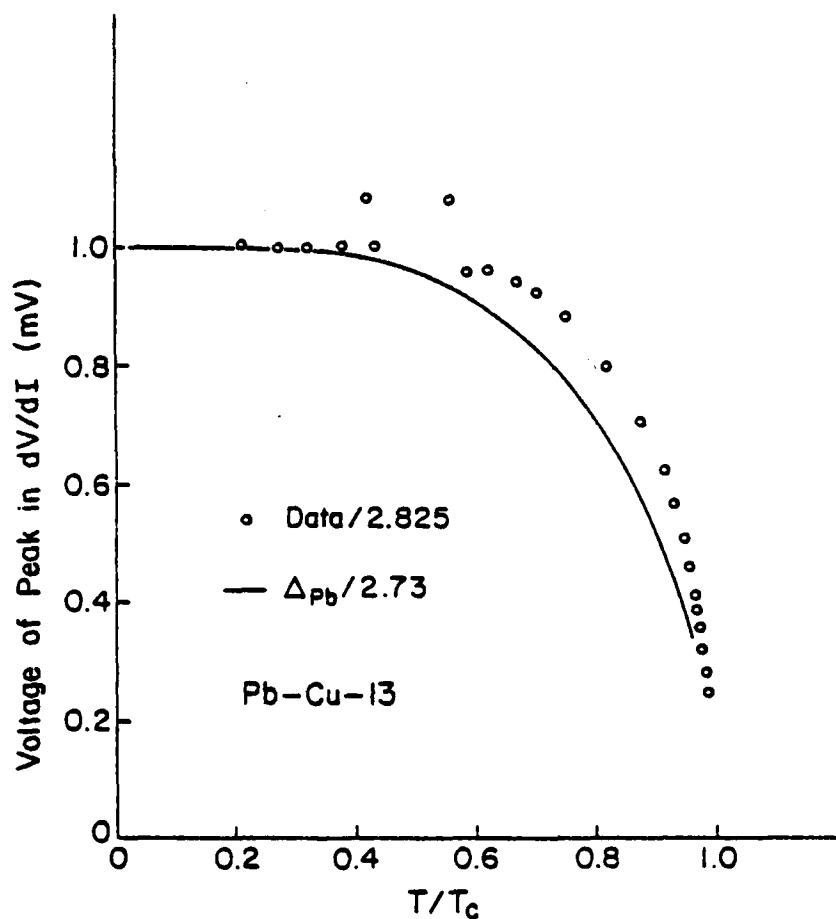
Figure 4.37 Temperature dependence of the voltage at which the peak in dV/dI occurs for Pb-Cu-13. The solid line is the gap voltage for Pb divided by 2.73. The data has been divided by 2.825.
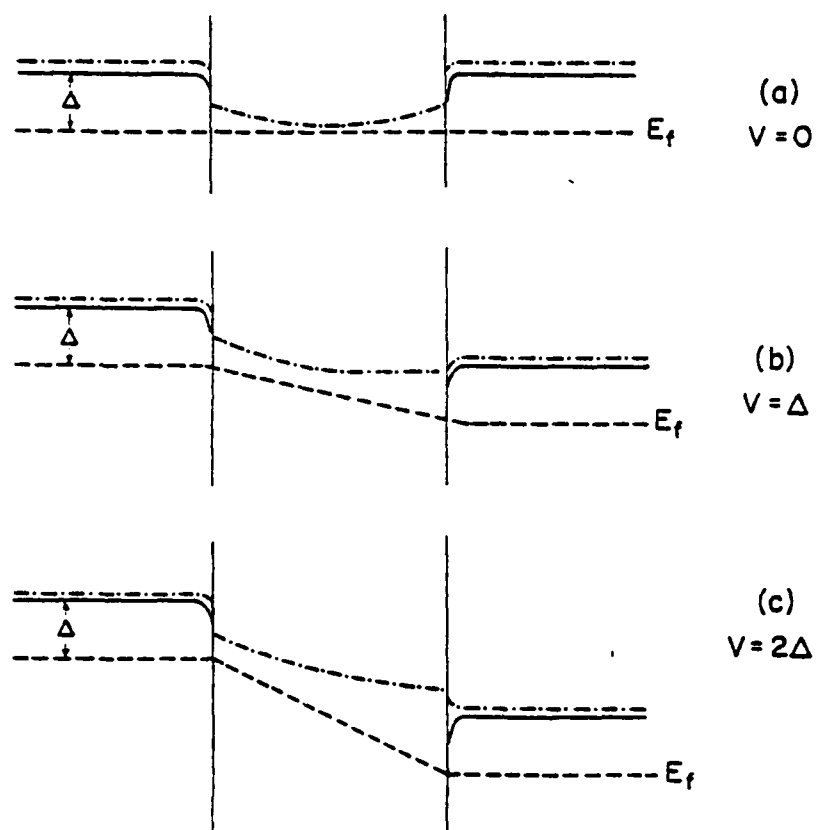
Figure 4.38   Schematic representation of the spatial variation of the
energy of the peak in the electron distribution across a
SNS microbridge. Δ is the gap in the superconductor, E_f
is the fermi energy, and V is the voltage across the micro-
bridge.

$(2\Delta)^2 = 4\Delta^2$. If one of the quasiparticles has energy 2Δ and the other Δ, the available phase space is proportional to $(3\Delta)^2 = 9\Delta^2$. Thus a quasiparticle with energy 2Δ combines more than twice as fast as one with energy Δ.)

Thus, as the voltage increases, the extra resistance increases and then decreases. Figure 4.37 shows the temperature dependence of the voltage of the dV/dI peak along with the temperature dependence of the energy gap. The shape is in fair agreement, but the voltage of the peak is larger than the gap voltage. The reason for this discrepancy is possibly the following: the peak in dV/dI should occur, according to the above model, when the energy of the peak in the electron distribution at the SN interface is equal to the gap in the superconducting banks. For this to happen, the voltage drop across the normal metal bridge must be equal to the energy gap plus the mean energy relaxation of an electron as it travels across the bridge. Now, the measured dc voltage also includes the voltage drops in the electrodes due to the electric field in the superconducting electrodes. Thus the peak in dV/dI should occur when the measured dc voltage is equal to the energy gap of the superconducting electrode plus the voltage drops in the electrodes plus the mean energy relaxation in the bridge.

It should be pointed out that simple Joule heating in the sample would also raise the mean energy, thus increasing the extra resistance. But increased heating would not cause a decrease in the occupation of an energy level, and would therefore not produce a drop in the resistance as the voltage increased. The drop in resistance is a consequence of the

length of the bridge being comparable to the inelastic diffusion length.

The observed peak could not be the result of a hot spot in the bridge, since a hot spot requires that as the temperature is lowered the peak should occur at higher voltages due to the need for increased power dissipation to sustain the hot spot; our peak occurs at a temperature-independent voltage at low temperatures.

The above analysis indicates that the width of the resistance peak is a measure of the width of the electron energy distribution in the normal metal. In addition, the various bumps on the dV/dI curve should also represent structure in the density of states near the interface. Several authors[13-15,61-63] have calculated that the occupied density of states near the fermi level is broadened and, in addition, the density of states actually oscillates with energy. Thus it appears that our experimental observations are somewhat in agreement with theory, but the agreement is at best qualitative. A major difficulty in applying the theories is that all of the theories are done in the clean limit, while our samples are in the dirty limit.

Rowell and McMillan[65] and Rowell[66] used a tunnelling geometry to measure the density of states in clean SN systems, and they found excellent agreement with theory. But since their experiments were tunnelling experiments, they put only a very small voltage across the normal metal. Our result appears to be the first observation of oscillations in the density of states in dirty systems, as well as the first observation of the oscillations by putting a relatively large voltage across the sample.

Chapter 5

OTHER SAMPLES

In addition to the lead-copper SNS microbridges, other samples were produced in the course of this work. Of these other samples, only those with niobium banks were of sufficient quality to justify detailed measurement of their electrical properties. But even these niobium-banked microbridges performed poorly compared to the lead-banked microbridges. (This poor performance was due primarily to the relatively long reduced lengths of these samples. Because of the difficulties in sample preparation, the niobium-banked structures had relatively thin bridges, of the order of 20 nm thickness. Thus, in spite of the shortness of the bridges on a geometrical scale, as short as 200 nm, the bridges were all fairly long in terms of the coherence length.) As a result of this poor performance, it was not possible to quantitatively compare the results of measurements on these niobium-banked structures to the available theories of superconducting weak links. However, it was useful to compare the electrical properties of these niobium-banked microbridges to the results obtained for the lead-banked microbridges. Thus, in order to make this comparison, the results on these other samples will be briefly presented.

5.1 Nb-Cu-Nb Samples

The microbridges consisting of niobium banks and copper bridges, like the lead-copper microbridges, were SNS microbridges. The current-phase relation of these Nb-Cu-Nb samples was found to be nearly sinusoidal at all temperatures for which the CPR could be measured. Furthermore, as
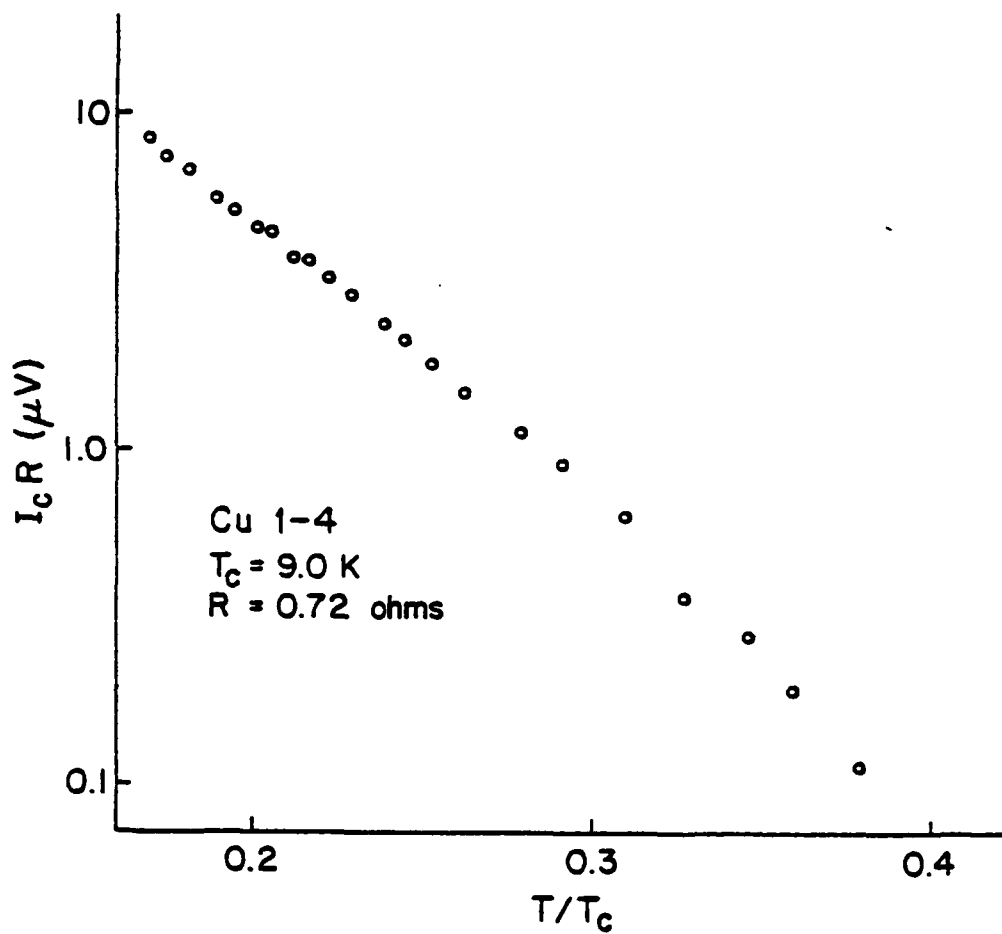
Figure 5.1 Log I_cR versus T/T_c for a Nb-Cu-Nb microbridge (Cu 1-4). This sample had a bridge about 20 nm thick, 200 nm wide and 200 nm long.
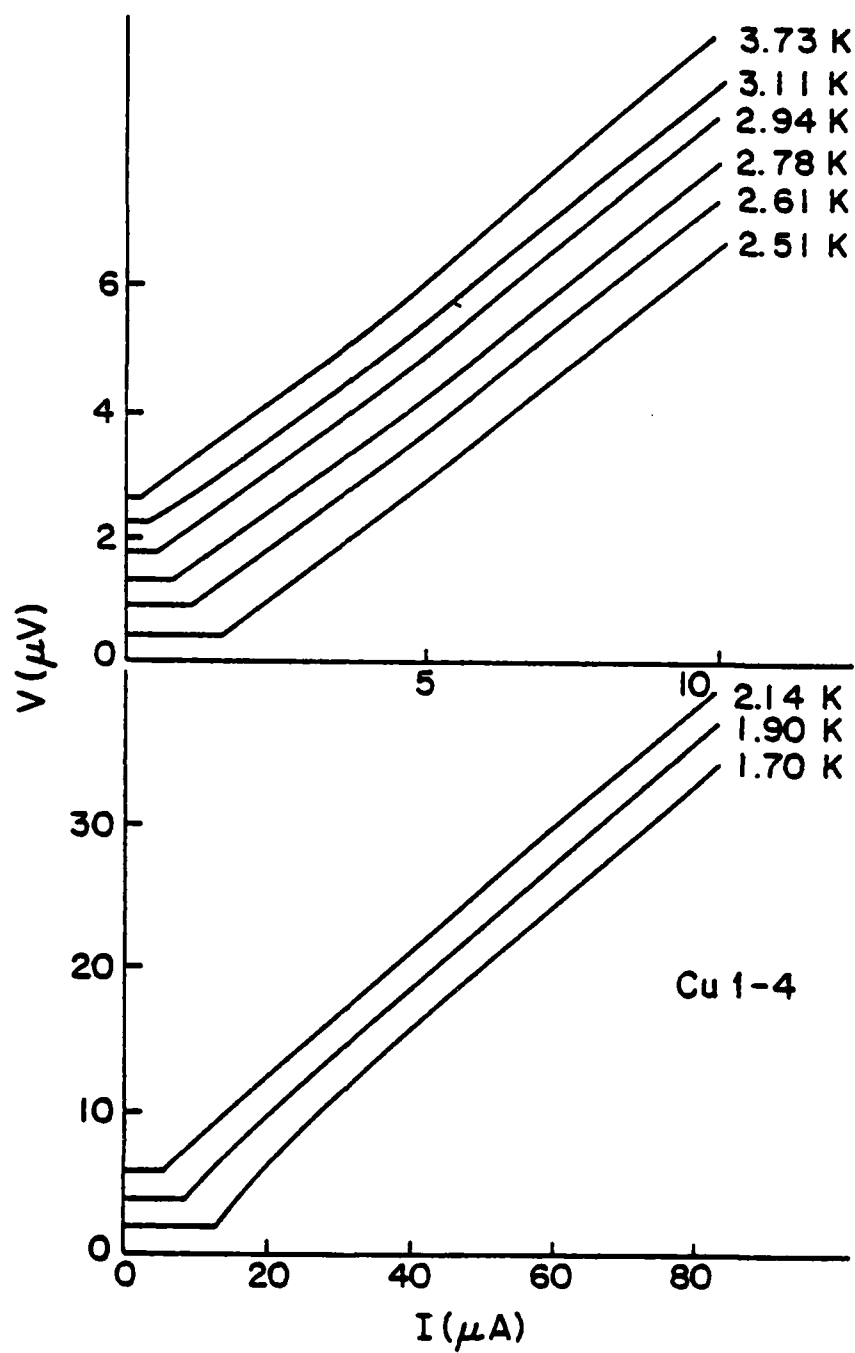
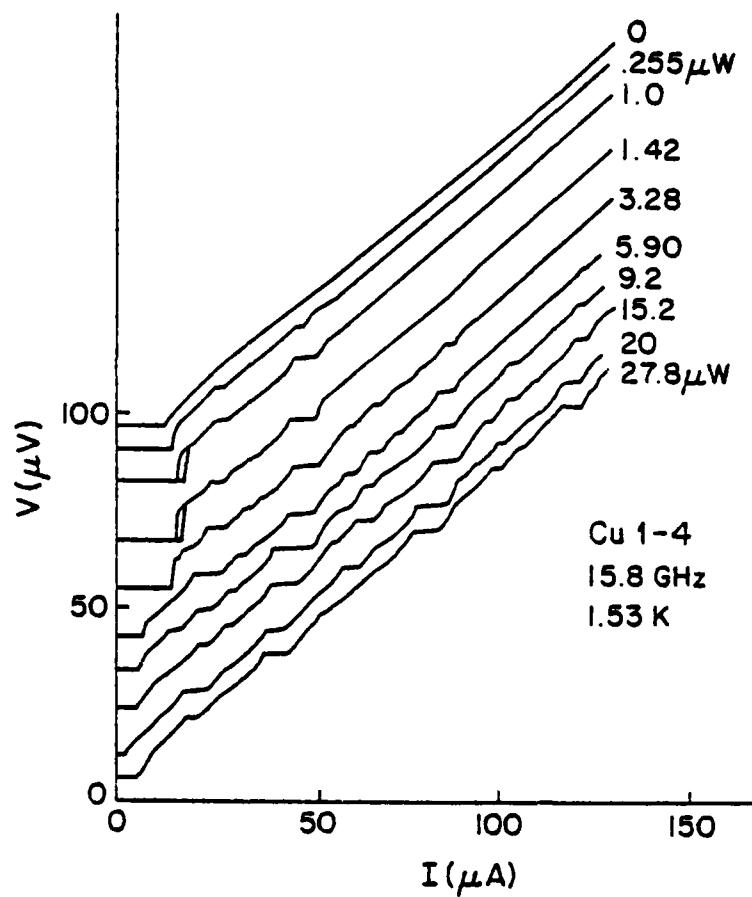Figure 5.2   I-V data for sample Cu 1-4.

Figure 5.3   I-V data for sample Cu 1-4 with 15.8 GHz radiation.

seen in Figure 5.1, the critical current was found to be nearly exponential in temperature. This I_c versus T data could be fit by Usadel's equations, resulting in a reduced length ℓ of 20.5. This reduced length was comparable to that of the longer lead-copper samples.

Figure 5.2 shows a set of I-V curves for the same sample (Cu 1-4) as in Figure 5.1. If these curves are compared to the I-V curves for a lead-copper sample having a similar reduced length, the sets of curves are found to be quite similar. At low voltages there is an inflection point in the I-V curve at about 2 microvolts; this voltage corresponds to a characteristic time of $\hbar/2eV = 1.6 \times 10^{-10}$ seconds. This time is in good agreement with the effective relaxation time of $\tau_{eff} = \ell^2 \pi\hbar/8kT_c = 1.4 \times 10^{-10}$ seconds. Somewhat above this inflection point the I-V curves become straight lines.

A relaxation time this long should cause hysteresis in the I-V at low temperatures; but, as with the longer Pb-Cu-Pb samples, the temperature could not be reduced to a low enough value for the hysteresis to be seen. However, it can be seen in Figure 5.2 that at the lowest temperatures achieved the I-V curve is discontinuous yet single-valued.

Figure 5.3 shows I-V curves for Cu 1-4 with 15.8 GHz applied microwave radiation. There are strong constant-voltage steps and there are significant subharmonic steps. These constant-voltage steps were observed to oscillate for several periods with increasing applied rf power. Data taken at 8.3 GHz showed similar constant-voltage steps with strong subharmonic steps. The presence of these subharmonic steps is in agreement with an effective relaxation time of 1.4×10^{-10} seconds. Data

taken at 2.0 GHz did not show subharmonic steps.

It can be seen in Figure 5.3 that with 15.8 GHz radiation there is
a slight enhancement of the critical current, and there is also a small
induced hysteresis. For 8.3 GHz and 2.0 GHz radiation no enhancement was
observed at these low temperatures. This is in good agreement with the
results obtained for the longer Pb-Cu-Pb samples at low temperatures.

Thus it seems that the results of measurements on the Nb-Cu-Nb SNS
microbridges support the ideas presented in Chapter 4. Unfortunately,
the long reduced lengths of these samples prevent any strong quantitative
comparisons to be made. It was not possible to lower the temperature
enough to observe hysteresis in the I-V curves, and the low values of
I_c made it impossible to measure the effects of applied rf radiation at
any but the lowest temperatures.

The Nb-Cu-Nb samples did have one strong advantage over the
Pb-Cu-Pb samples, however. The high melting temperatures of niobium and
copper meant that prolonged storage of these samples at room temperature
did not alter their electrical characteristics.

5.2 Nb-Al-Nb Samples

Microbridges with niobium banks and aluminum bridges were produced
in which the bridge was about 20 nm thick and one micron long. Figure 5.4
shows a set of I-V curves for one of these samples (A 14-3). These curves
show no hysteresis or other noteworthy features. Figure 5.5 shows the
critical current versus temperature data for this sample; I_c is seen to
be nearly exponential in temperature. This $I_c(T)$ relation is similar
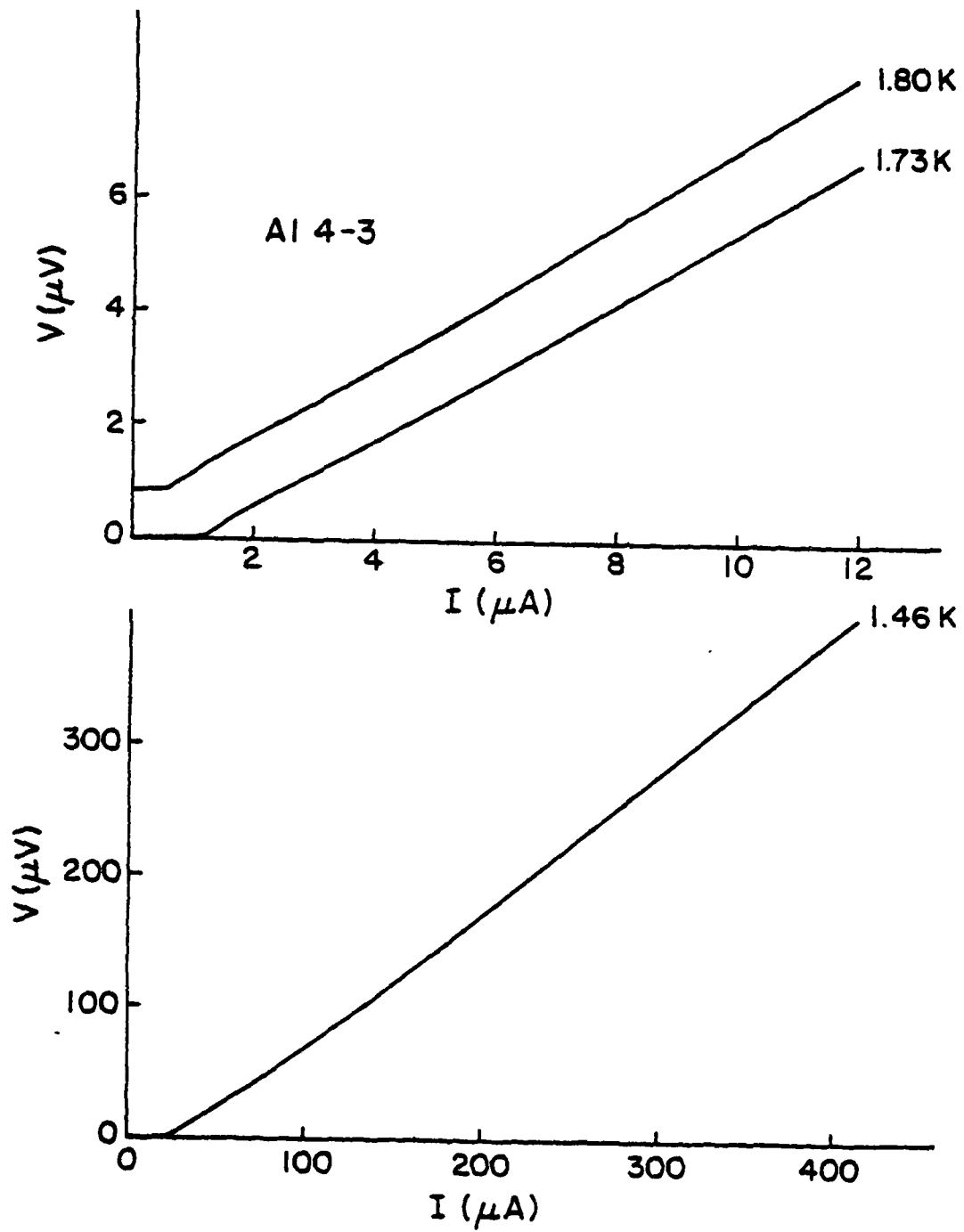to that found for SNS structures. However, the solution to Usadel's

Figure 5.4 I-V data for a Nb-Al-Nb microbridge (Al 4-3). This sample
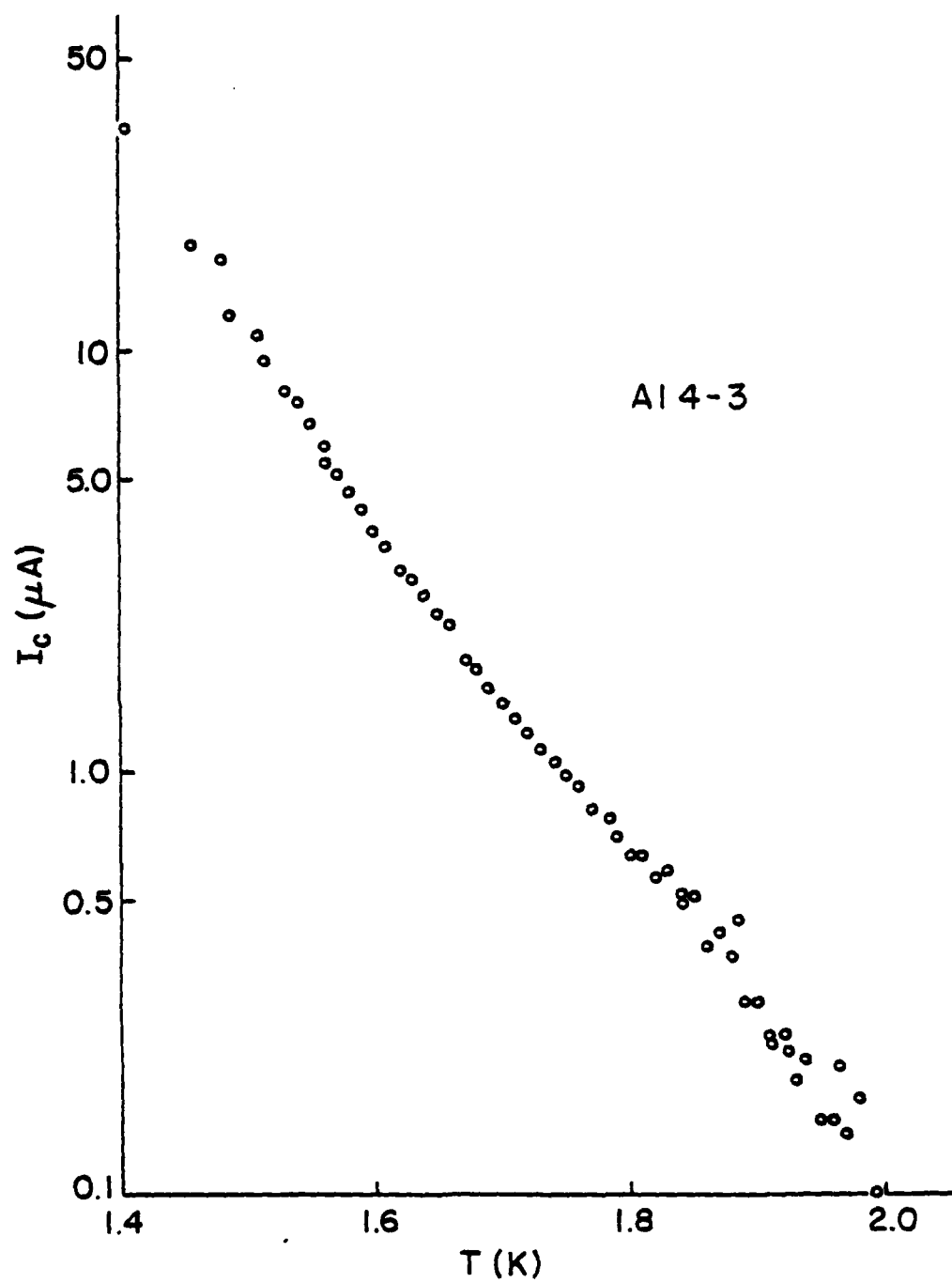had a bridge about 20 nm thick, one micron wide and one
micron long.

Figure 5.5 Log I_c versus T data for sample Al 4-3.

equations found in Chapter 4 is not applicable to these samples, since aluminum is a superconductor with a T_c of about 1 K; there has not been any theory advanced which predicts an I_c versus T relation for micro-bridges with such a large difference between the transition temperatures of the bridge and banks, for data taken near the transition temperature of the bridge.

The current-phase relation for sample A14-3 was found to be nearly sinusoidal at all temperatures of measurement.

Figure 5.6 shows I-V curves with 2.0 GHz applied microwave radiation. There are no subharmonic steps, and there is no enhanced critical current. The constant-voltage steps showed only a single oscillation period with increasing microwave power. Measurements were also performed at 7 GHz, and no enhancement of I_c was observed.

The poor performance of these samples, both with respect to the low values of $I_c R$ and the lack of good constant-voltage steps, was probably due to the thinness of the bridges.

5.3 Nb-Nb-Nb Samples

Variable-thickness microbridges were produced in which both the bridge and the banks were made from niobium; the bridges were about 25 nm thick and the banks were about 60 nm thick.

Figure 5.7 shows critical-current versus temperature data for a sample (Nb 36-1) which had a bridge about 0.5 micron long; Figure 5.8 shows similar data for a sample (Nb 37-2) which had a bridge about 1.5 microns long. For both samples I_c was found to be nearly proportional to $(T_c-T)^{3/2}$, in agreement with the predictions for a two-dimensional
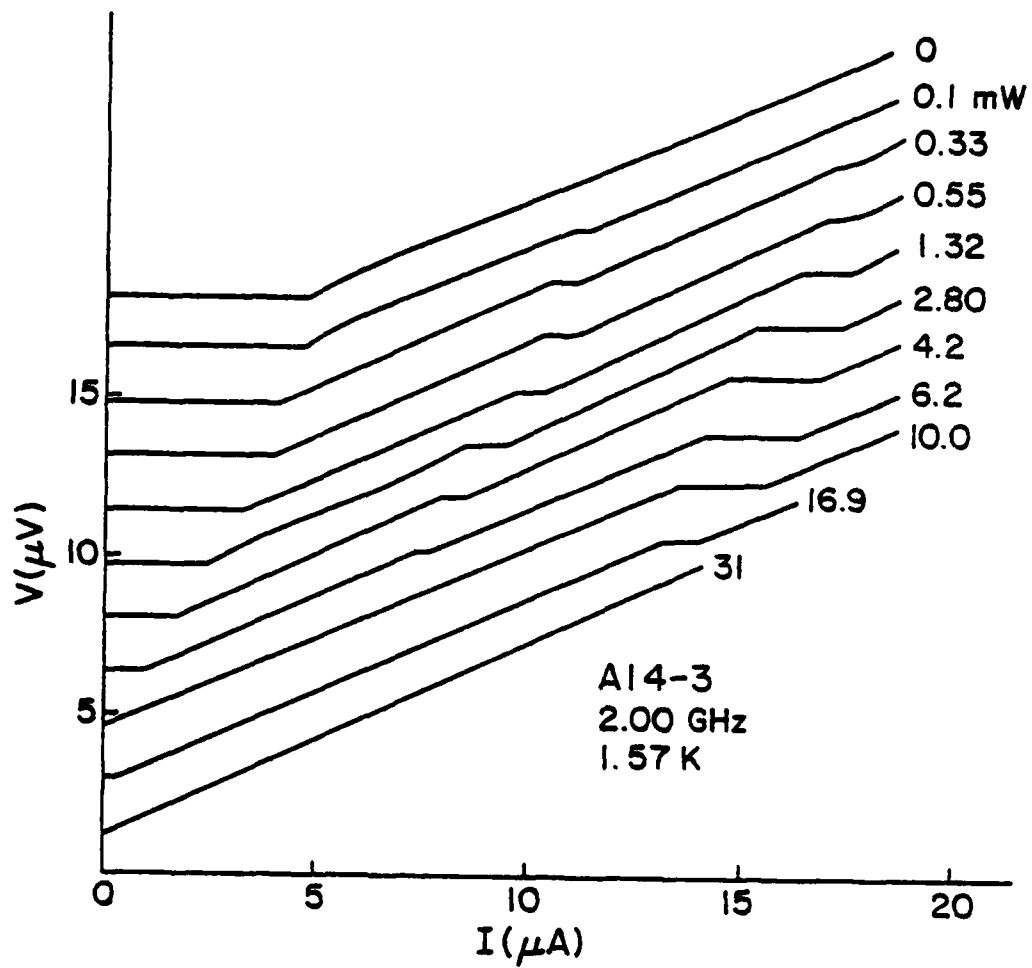
Figure 5.6   I-V data for sample Al 4-3 with 2.0 GHz radiation.
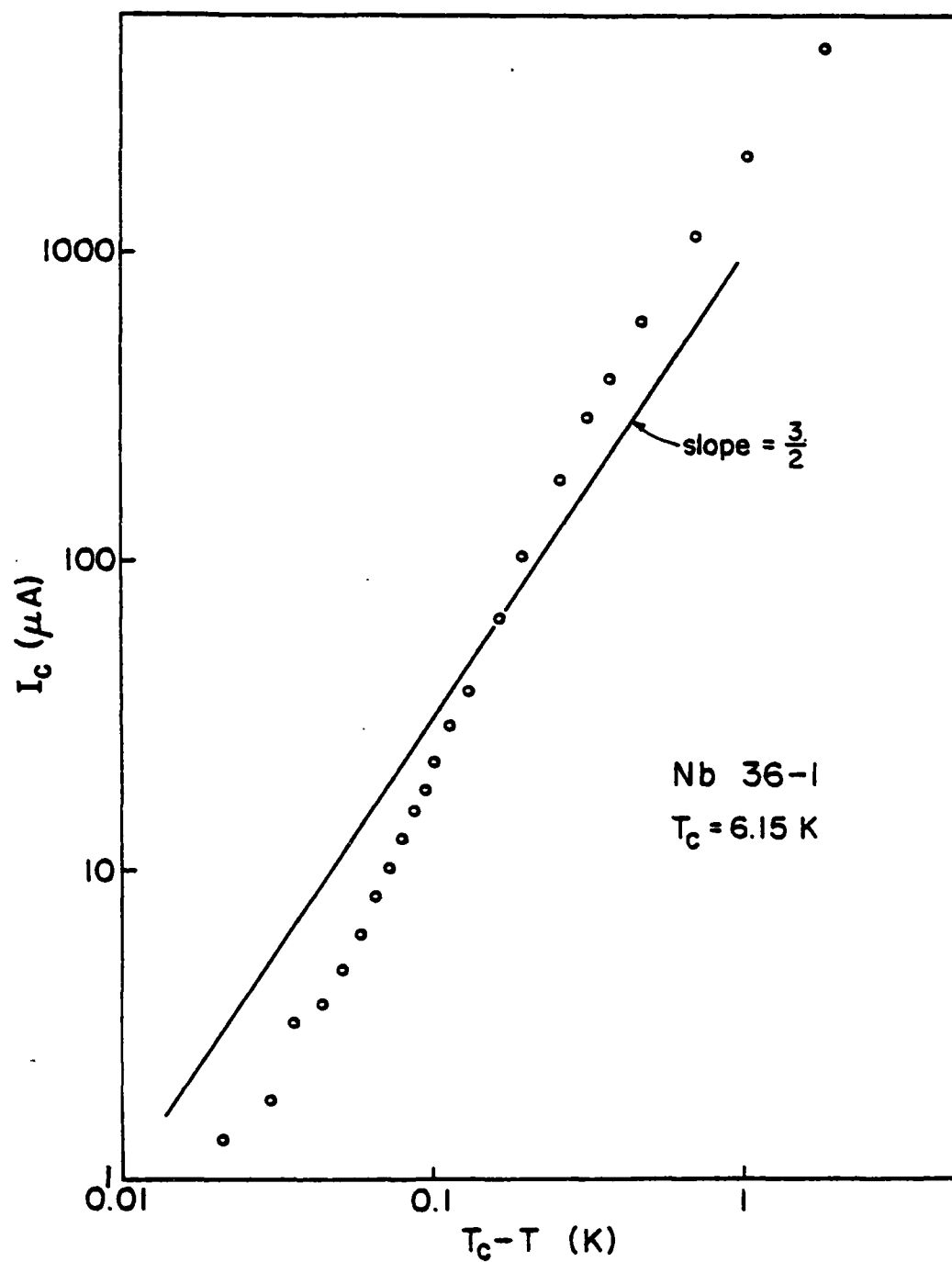
Figure 5.7   Log I_c versus (T_c-T) data for a Nb-Nb-Nb microbridge
(Nb 36-1). This sample had a bridge about 0.5 microns
wide and 0.5 microns long.
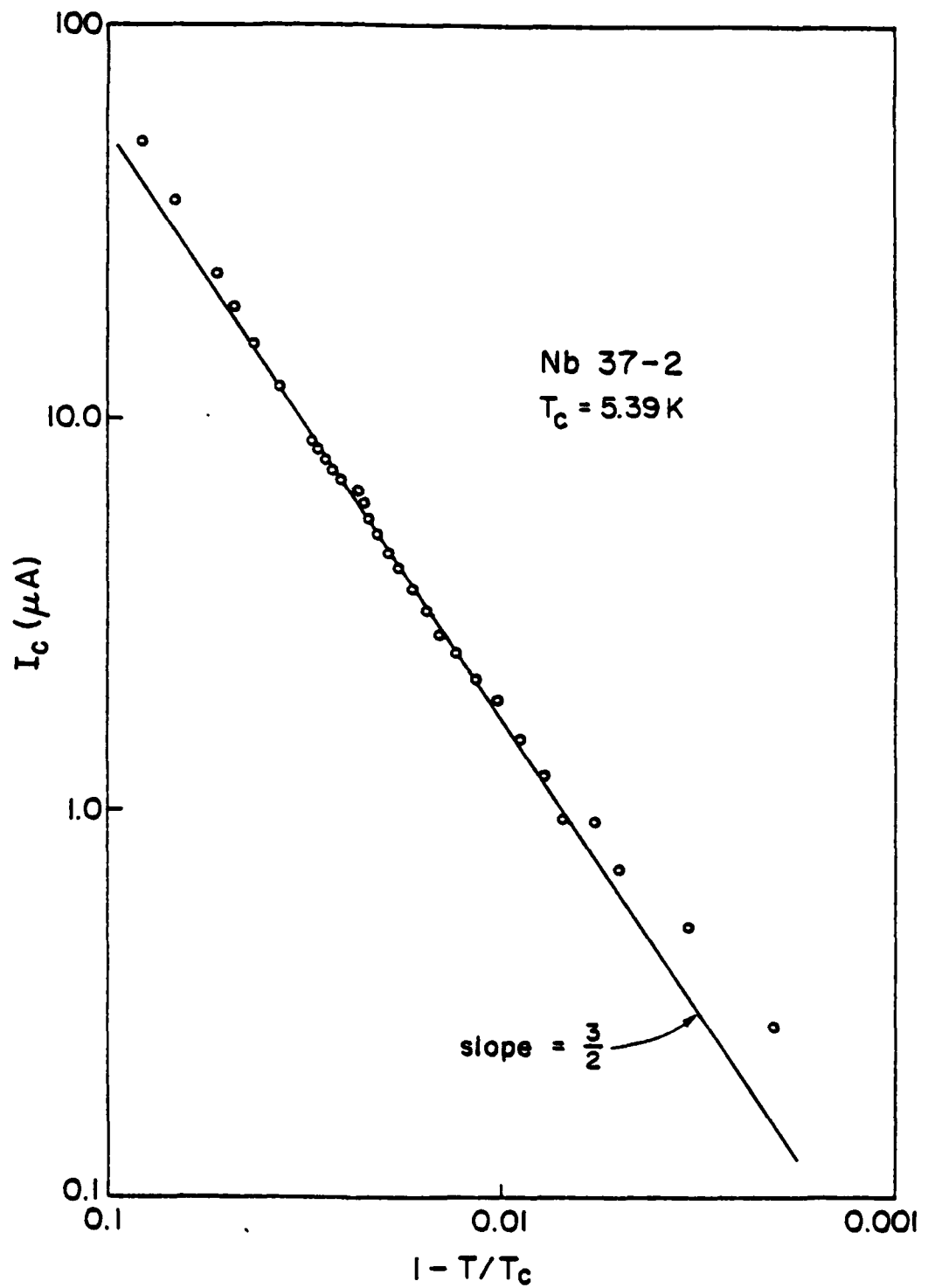
Figure 5.8 Log I_c versus ($1-T/T_c$) data for Nb-Nb-Nb microbridge
(Nb 37-2). This sample had a bridge about 0.5 microns
wide and 1.5 microns long.

superconducting film; this data indicates that these samples were extremely non-ideal. Current-phase measurements on Nb 36-1 found that the CPR was non-sinusoidal, becoming multi-valued slightly below T_c.

Figure 5.9 shows I-V curves for Nb 36-1. There are two interesting features. First, the I-V has an upward curvature almost everywhere; this is probably due to heating. Second, at lower temperatures the I-V curve is hysteretic. Figure 5.10 shows the dependence of the return current I_R on the critical current; it was found that $I_R \propto I_c^{\frac{1}{2}}$. This indicates that the hysteresis was due to heating[27], in contrast to the relaxation-time-induced hysteresis seen in the Pb-Cu-Pb samples.

These samples were studied with applied microwave radiation for frequencies up to 10 GHz, and only extremely weak constant-voltage steps were seen. No enhancement of the critical current was observed.

Figure 5.9 I-V data for sample Nb 36-1.

Figure 5.10   Return current (I_R) versus critical current (I_c) for
sample Nb 36-1.

Chapter 6

SUMMARY AND CONCLUSION

The results reported in this work represent the first measurements
of the electrical properties of short, high resistance (R $\sim$ 1 ohm) SNS
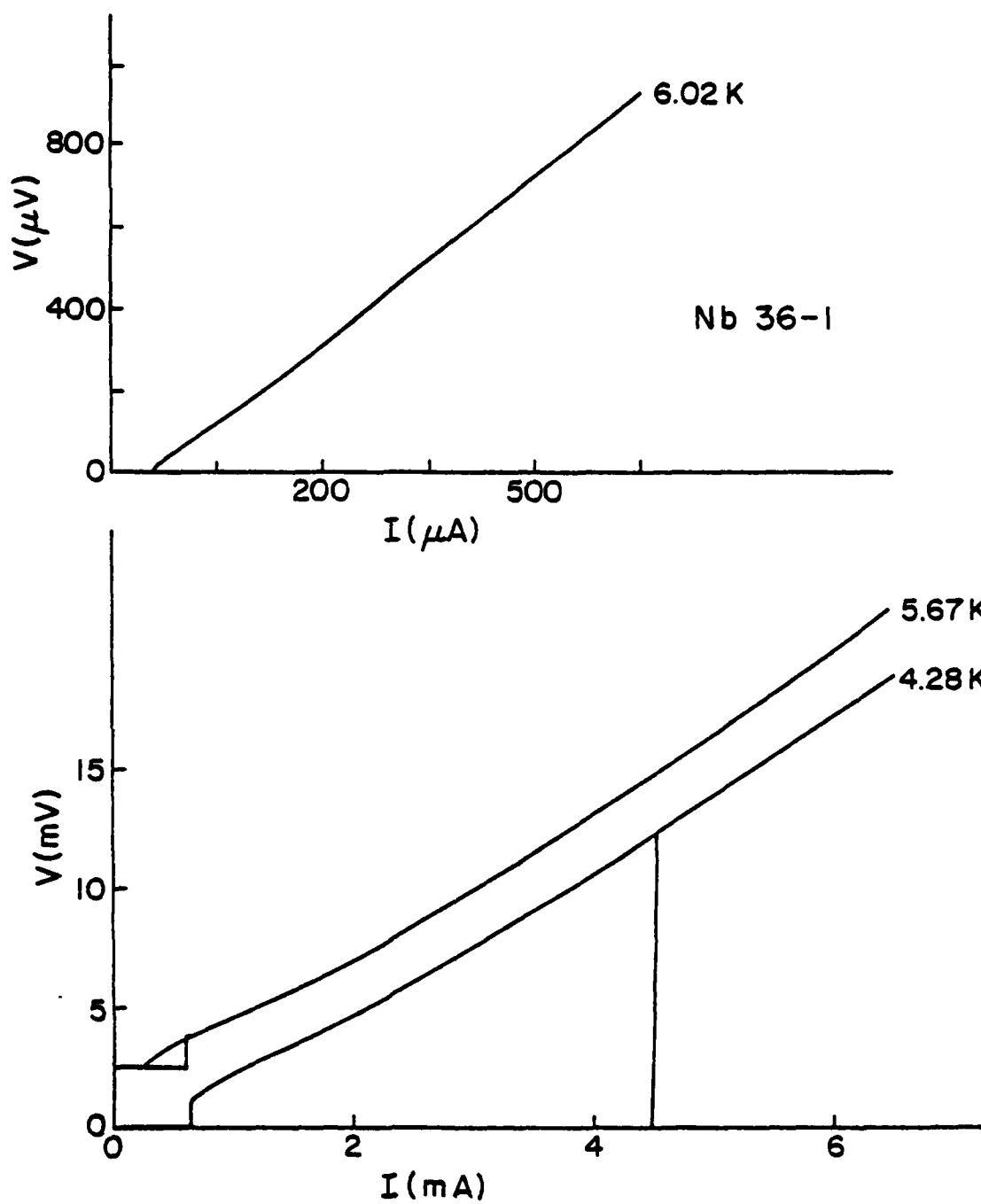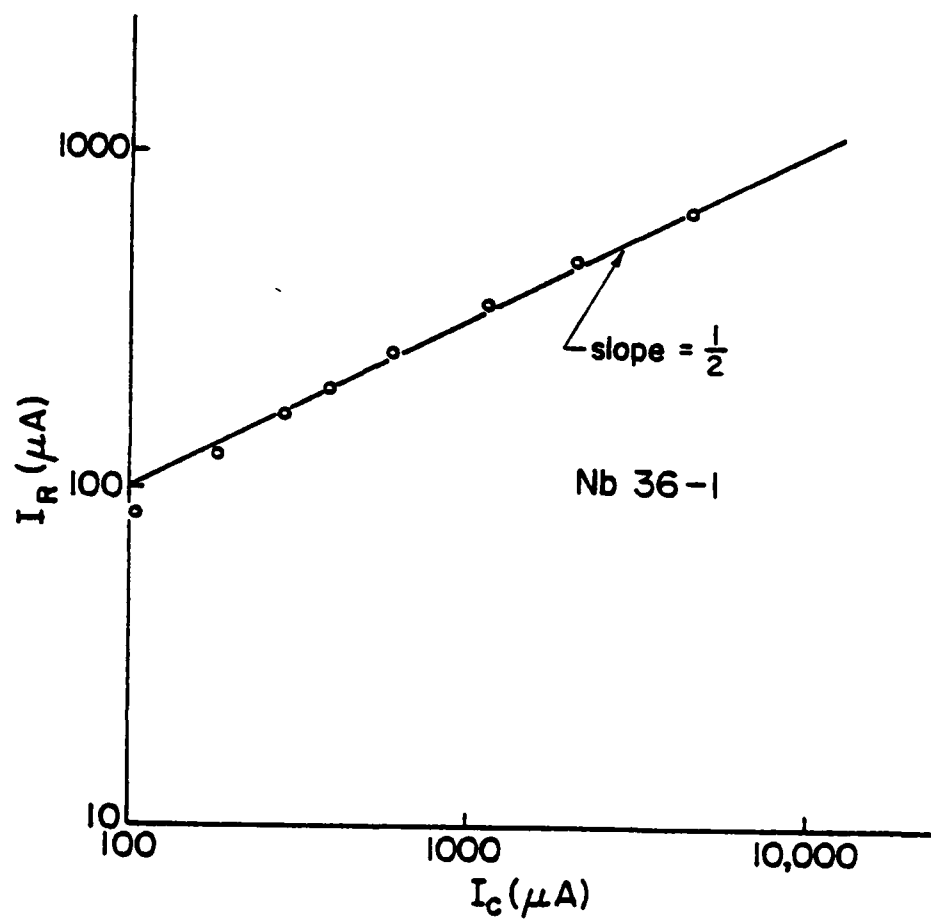microbridges. These small (length and width as small as 200 nm), planar
structures were produced using the advanced microfabrication techniques
of electron-beam lithography and ion-beam etching.

The small cross section of the bridges resulted in a uniform current
distribution in the bridges at all temperatures. This enabled us to make
the first experimental determination of the critical current versus tempera-
ture relation at temperatures far from the critical temperature T_c of the
banks; the I_c versus T relation was measured for all temperatures between
T_c and 0.05 T/T_c. We found that our experimental $I_c(T)$ relation was in
good agreement with theoretical predictions based on Usadel's equations.[22]
(Usadel's equations are a reformulation of Gorkov's formulation of super-
conductivity. They are valid for any superconducting system in the dirty
limit, not just for SNS microbridges. This work has provided the first
experimental verification of these equations.) This successful fit of
theory to experiment produced a reduced length ℓ for each sample, with
$\ell = L/(\hbar v_f \Lambda/6\pi k T_c)^{\frac{1}{2}}$ where L is the physical length of the bridge and Λ
is the electron mean free path in the bridge. Our samples had reduced
lengths ranging from 8.9 to 30.

The low-voltage (V $\stackrel{\scriptstyle <}{\scriptstyle \sim}$ 10 $I_c R$) current-voltage (I-V) characteristics
were studied in detail, and we observed for the first time the effects of
an intrinsic relaxation time on the I-V curves. We found that these I-V

curves could be characterized by an intrinsic temperature-independent relaxation time $\tau_{eff} = \ell^2\pi\hbar/8kT_c$ where ℓ is the reduced length of the bridge determined from the $I_c(T)$ data. We found that at high temperatures there was an inflection point in the I-V curve at a voltage $V \sim \hbar/2e\tau_{eff}$. At low temperatures the I-V curves were hysteretic, with the I-V curve returning to the zero-voltage axis at a return current I_R. At all temperatures the I-V curve became a straight line at a voltage V_{lower}.

We observed that at low temperatures I_RR and V_{lower} were independent of temperature, with both I_RR and V_{lower} having the same low-temperature value of $\hbar\Gamma_R/2e\tau_{eff}$ ($\Gamma_R \sim 5$). We found that Γ_R was nearly independent of the sample length. These observations confirmed both the temperature independence of τ_{eff} and the ℓ^2 dependence of τ_{eff}.

This was the first observation of hysteresis in SNS structures. It was also the first time that the hysteresis in any type of planar microbridge could be definitely attributed to a relaxation time rather than heating or capacitance.

It was found that the nature of the I-V curve with applied microwave radiation was also dependent on the effective relaxation time. These I-V curves showed, for some microwave frequencies, a microwave-enhanced critical current. It was determined that if the microwave period τ_{rf} was shorter than either $\hbar/2eI_cR$ or τ_{eff}, the critical current was enhanced. If τ_{rf} was longer than both of these times, there was no enhancement. This result indicates that the popular gap-enhancement explanation for a microwave-enhanced critical current does not apply to these SNS

microbridges, but that the enhancement is more likely caused by a microwave-induced spatial broadening of the quasiparticle distribution.

Constant-voltage steps were observed in the I-V curves for all frequencies of applied microwave radiation used. Subharmonic steps were observed whenever the criterion for an enhanced critical current was in effect, i.e., for τ_{rf} less than τ_{eff} or $\hbar/2eI_cR$. If τ_{eff} was longer than both of these times, there were no subharmonic steps. The good thermal properties of these microbridges was demonstrated by the observation of constant-voltage steps at dc voltages in excess of 2 mV for the shortest samples.

The high resistance of these samples allowed us to make the first measurements of the I-V curves for voltages much greater than the energy gap of the electrodes. A high-voltage peak in the dV/dI curves was observed, and it was speculated that this peak is due to an extra dissipation in the electrodes. In addition, the low-voltage resistance was found to have an extra, temperature-dependent component. The temperature dependence of this resistance was found to agree with the phenomenological theory of Pippard et al.[50], a theory which attributes the extra resistance to energy dissipation in the superconducting electrodes.

A.1 Numerical Solution of Usadel's Equations for SNS Structures

It was pointed out in Chapter 4 that the correlation functions for an SNS structure obey Usadel's[22] equations:

$$2\omega F_n(x) = D \frac{d}{dx}\left\{(1 - F_n^2)^{1/2} \frac{dF_n}{dx} + \frac{1}{2} \frac{F_n}{(1 - F_n^2)^{1/2}} \frac{dF_n^2}{dx}\right\}$$

where $D = \frac{1}{3} v_f \Lambda$ and $\omega = (2n+1)\pi kT/\hbar$. Note that there are an infinite number of F_n's.

The current through the bridge is given by

$$I_s R = \frac{\pi kT}{e} \sum_{n>0} j_n \ell$$

where

$$\ell = \frac{L}{\xi(T)} = L \left(\frac{\hbar v_f \Lambda}{6\pi kT}\right)^{1/2}$$

and

$$j_n = -\frac{i}{2}\left(F_n^* \frac{dF_n}{dx} - F_n \frac{dF_n^*}{dx}\right)$$

Likharev[21] has demonstrated that these equations can be solved in the following manner. First, use the coherence length as a scale of spatial dimension, i.e., units of $(\hbar v_f \Lambda/6\pi kT)^{1/2}$. Second, write the complex function F as $F = \sin\theta e^{i\gamma}$ where θ and γ are real.

Let θ_0 be the value of θ at the center of the bridge, and θ_B the value of θ at the banks. Then we have the following equations:

$$\frac{d\theta}{dx} = \left|j_n^2\left(\frac{1}{\sin^2\theta_c} - \frac{1}{\sin^2\theta}\right) + 2(2n+1)(\cos\theta_0 - \cos\theta)\right|^{1/2},$$

$$\ell = \frac{L}{\xi(T)} = 2\int_{\theta_0}^{\theta_B} \frac{d\theta}{d\theta/dx},$$

and

$$\phi = \text{phase difference across bridge} = 2j_n \int_{\theta_0}^{\theta_B} \frac{d\theta}{\frac{d\theta}{dx} \sin^2\theta} \quad \text{where}$$

$$\theta_B = \tan^{-1}\left[\frac{\Delta(T)}{(2n+1)\pi kT}\right] \quad \text{with } \Delta(T) \text{ the value of the energy}$$

gap in the superconducting electrodes.

The difficulty with the above equations is that we are interested in knowing j_n as a function of ℓ and ϕ. These integral equations were solved using the following iterative method.

First, by trial and error, values of θ_0 and j_n were found which gave the desired ℓ at $\phi = 0.05$. (With a little experience this was fairly easy. The integrals were evaluated using Simpson's rule with a variable spacing; the spacing between points was varied as $1/\theta^3$, and usually 1000 points were used.)

Once these initial values were determined, the full j_n versus ϕ relation was found by incrementing ϕ by 0.05 and finding the values of j_n and θ_0 which gave the desired ℓ. (This procedure was made automatic by using Newton's method for finding the zeros of a function.)

This procedure gave the current j_n as a function of ϕ. For all the lengths and temperatures applicable to our samples, j_n was found to vary as $\sin\phi$ within 10%.

The above procedure had to be repeated for increasing values of n until increasing n changed Σj_n by less than .01%. (For $T/T_c = 0.6$ only $n = 1$ was needed; for $T/T_c = 0.1$ values of n up to 4 were required.)

A.2 Numerical Simulation of the Shunted Junction Model

The resistively shunted junction model is given by

$$I_{dc} + I_{rf} \sin(\omega_{rf} t) = I_c \sin\phi + V/R$$

and

$$V = (\hbar/2e) \frac{d\phi}{dt} .$$

If currents are measured in units of I_c, voltage in units of $I_c R$, and time in units of $\hbar/2eI_c R$, then these equations become

$$I_{dc} + I_{rf} \sin(\omega_{rf} t) = \sin\phi + V$$

and

$$V = \frac{d\phi}{dt} .$$

These equations were solved numerically by stepwise integration. That is, initially $V = 0$, $\phi = 0$, and $t = 0$. The time was then incremented by Δt, and I_s, V, and ϕ were recalculated by

$$I_s = \sin\phi$$
$$V = I_{dc} + I_{rf} \sin(\omega_{rf} t) - I_s$$
$$\phi = V\Delta t .$$

This process was continued for several periods, with the values of I_s, V, and ϕ recorded at each step. The end result was $I_s(t)$, $V(t)$, and $\phi(t)$ data. Typically, $\Delta t = .01$, and the values of I_s, V, and ϕ were not recorded until several periods had passed (about 1000 steps) to ensure that the iteration had stabilized.

In order to calculate an I-V curve, the above procedure was carried out for several values of I_{dc}. V_{dc} was determined by averaging V over a few hundred periods.

The effects of a characteristic relaxation time τ_{relax} were incorporated by calculating I_s with the equation

$$I_s = \sin\phi \left/ \left(1 + \frac{V^2}{V_{relax}^2}\right) \right.$$

where

$$V_{relax} = \hbar/(2eI_cR\tau_{relax}) \ .$$

References

1. B. D. Josephson, Phys. Lett. 1, 251 (1962); Rev. Mod. Phys. 36, 216 (1964); Adv. Phys. 14, 419 (1965).

2. K. K. Likharev, Rev. Mod. Phys. 51, 101 (1979).

3. L. D. Jackel, Ph.D. thesis, Cornell University, 1976 (unpublished).

4. W. H. Henkels, Ph.D. thesis, Cornell University, 1974 (unpublished).

5. P. E. Gregers-Hansen and M. T. Levinsen, Phys. Rev. Lett. 27, 1847 (1971).

6. P. W. Andersen and A. H. Dayem, Phys. Rev. Lett. 13, 195 (1964).

7. P. G. deGennes, Rev. Mod. Phys. 36, 225 (1964).

8. I. Haller, M. Hatzakis, and R. Srinivisan, IBM J. Res. Dev. 12, 251 (1968).

9. E. D. Wolf, F. S. Ozdemir, W. E. Parkins and P. J. Coane, "Rec. IEEE 11th Symp. on Electron, Ion, and Laser Beam Tech.", ed. by R. F. M. Thornley (San Francisco Press, 1971).

10. Mihir Parikh and David F. Kyser, J. App. Phys. 50, 1104 (1979).

11. C. M. Melliar-Smith, J. Vac. Sci. Tech. 13, 1008 (1976).

12. M. Gaerttner (private communication).

13. R. O. Zaitsev, Sov. Phys. JETP 21, 426 (1965).

14. P. G. deGennes and D. Saint-James, Phys. Lett. 4, 151 (1963).

15. I. O. Kulik, Sov. Phys. JETP 30, 944 (1970).

16. Chikara Ishii, Prog. Theor. Phys. 44, 1525 (1970).

17. John Bardeen and Jared L. Johnson, Phys. Rev. B5, 72 (1972).

18. A. I. Bezuglyi, I. O. Kulik, and Yu N. Mitsai, Sov. J. Low Temp. Phys. 1, 27 (1975).

19. I. O. Kulik and Yu N. Mitsai, Sov. J. Low Temp. Phys. 1, 434 (1975).

20. H. J. Fink, Phys. Rev. B14, 1028 (1976).

21. K. K. Likharev, Sov. Tech. Phys. Lett. 2, 12 (1976).

22. Klaus D. Usadel, Phys. Rev. Lett. 25, 507 (1970).

23. J. Clarke, Proc. Roy. Soc. London 308A, 447 (1969).

24. J. G. Shepherd, Proc. Roy. Soc. London 326A, 421 (1972).

25. W. C. Stewart, App. Phys. Lett. 12, 277 (1968).

26. D. E. McCumber, J. App. Phys. 39, 3113 (1968).

27. W. J. Skocpol, M. R. Beasley, and M. Tinkham, J. App. Phys. 45, 4054 (1974).

28. Y. Song, J. App. Phys. 47, 2651 (1976).

29. A. Baratoff and L. Kramer, "Superconducting Quantum Interference Devices and Their Applications", edited by H. D. Hahlbohm and H. Lübbig (Walter de Gruyter, New York, 1977), p. 51.

30. B. R. Fjorbøge and P. E. Lindelof, J. Low Temp. Phys. 31, 83 (1978).

31. M. Tinkham, "Introduction to Superconductivity" (McGraw-Hill, New York, 1975), p. 275.

32. K. K. Likharev and L. A. Yakobsen, Sov. Phys. JETP 41, 570 (1975).

33. L. G. Aslamazov and A. I. Larkin, Sov. Phys. JETP 43, 698 (1976).

34. A. A. Golub, Sov. Phys. JETP 44, 178 (1976).

35. John Clarke, Phys. Rev. B4, 2963 (1971).

36. N. I. Komarovskikh, G. M. Lapir, A. N. Samus', and V. K. Semenov, Sov. Tech. Phys. Lett. 1, 432 (1975).

37. A. F. G. Wyatt, V. M. Dmitriev, W. S. Moore, and F. W. Sheard, Phys. Rev. Lett. 16, 1166 (1966).

38. A. H. Dayem and J. J. Wiegand, Phys. Rev. 155, 419 (1967).

39. P. E. Gregers-Hansen, M. T. Levinsen, L. Pedersen and C. J. Sjøstrøm, Solid State Comm. 9, 661 (1971).

40. B. R. Fjordbøge, T. D. Clark, and P. E. Lindelof, Phys. Rev. Lett. 37, 1302 (1976).

41. H. A. Notarys, M. L. Yu, and J. E. Mercereau, Phys. Rev. Lett. 30, 743 (1973).

42. H. A. Notarys and J. E. Mercereau, Physica 55, 424 (1971).

43. J. E. Mercereau, "Superconducting Quantum Interference Devices and Their Applications", edited by H. D. Hahlbohm and H. Lübbig (Walter de Gruyter, New York, 1977), p. 101.

44. Yu. I. Latyshev and F. Ya. Nad', JETP Lett. 19, 380 (1974).

45. G. M. Eliashberg, JETP Lett. 11, 114 (1970).

46. Jhy-Jiun Chang and D. J. Scalapino, J. Low Temp. Phys. 29, 477 (1977).

47. P. E. Lindelof, Solid State Comm. 18, 283 (1976).

48. L. G. Aslamazov and A. I. Larkin, Phys. Lett. 67A, 226 (1978).

49. P. Russer, J. App. Phys. 43, 2008 (1972).

50. A. B. Pippard, J. G. Shepherd, and D. A. Tindall, Proc. Roy. Soc. London A324, 17 (1971).

51. G. L. Harding, A. B. Pippard, and J. R. Tomlinson, Proc. Roy. Soc. London A340, 1 (1974).

52. A. F. Andreev, Sov. Phys. JETP 19, 1228 (1964).

53. G. J. Dolan and L. D. Jackel, Phys. Rev. Lett. 39, 1628 (1977).

54. Albert Schmid and Gerd Schön, J. Low Temp. Phys. 20, 207 (1975).

55. S. N. Artemenko, A. F. Volkov, and A. V. Zaitsev, J. Low Temp. Phys. 30, 487 (1978).

56. Y. Krähenbühl and R. J. Watts-Tobin, J. Low Temp. Phys. 35, 569 (1979).

57. U. Kaiser-Dieckhoff, "Superconducting Quantum Interference Devices and Their Applications", edited by H. D. Hahlbohm and H. Lübbig (Walter de Gruyter, New York, 1977), p. 165.

58. Li-Kong Wang, Dae-Jin Hyun, and Bascom S. Deaver, Jr., J. App. Phys. 49, 5602 (1978).

59. P. E. Gregers-Hansen, E. Hendricks, M. T. Levinsen, and G. R. Pickett, Phys. Rev. Lett. 31, 524 (1973).

60. J.-J. Chang and D. J. Scalapino, "Superconductor Applications: SQUIDs and Machines", ed. by Brian B. Schwartz and Simon Foner (Plenum, New York, 1977), p. 455.

61. R. O. Zaitsev, Sov. Phys. JETP 23, 702 (1966).

62. W. L. McMillan, Phys. Rev. 175, 537 (1968); Phys. Rev. 175, 559 (1968).

63. Reiner Kümmel, Phys. Rev. B3, 784 (1971).

64. S. B. Kaplan, C. C. Chi, C. N. Langenberg, J. J. Chang, S. Jafarey, and D. J. Scalapino, Phys. Rev. B14, 4854 (1976).

65. J. M. Rowell and W. L. McMillan, Phys. Rev. Lett. 16, 453 (1966).

66. J. M. Rowell, Phys. Rev. Lett. 30, 167 (1973).